SUPER STAR CLUSTER CANDIDATES IN THE STAR-FORMING REGIONS OF LUMINOUS INFRARED GALAXIES

By

Rojovola Zara-Nomena Randriamanakoto

A dissertation submitted in partial fulfillment of the requirements for the degree M.Sc. in the Department of Astronomy, as part of the National Astrophysics and Space Science Programme

UNIVERSITY OF CAPE TOWN

DECEMBER 2010

Supervisors:

Dr. Petri Väisänen[1]

Dr. Sarah Blyth[2]

[1]South African Astronomical Observatory

[2]Astronomy Department, University of Cape Town

Abstract

We report on a study of super star cluster (SSC) candidates in the star-forming regions of a representative sample of local luminous infrared galaxies (LIRGs) using K_S-band near-infrared (NIR) adaptive optics imaging with GEMINI/ALTAIR and VLT/NACO instruments. The evolution of the cosmic star formation rate (CSFR) indicates its rapid decline in the local Universe. LIRGs ($L_{ir} = 10^{11} - 10^{12}\mathrm{L}_{\odot}$) are shown to contribute a large amount to the CSFR in the early Universe, whereas they are very few at lower redshifts. This work is based on the study of local LIRGs with the ultimate goal of understanding high redshift galaxies. *Specifically, it aims to derive the first-ever K_S-band SSC luminosity functions (LFs) and to establish an empirical relation of the brightest SSC candidate with the global star formation rate (SFR) of the galaxy.* LIRGs have been found to host a large number of SSCs. After the data reduction and photometric calibration, we select the potential SSC candidates in each target galaxy and construct the LFs using two different binning methods. We then correct the data for observational incompleteness. We find a slope index of the order of $\alpha \sim 1.5 \pm 0.2$ of the power-law form $N(L)dL \sim L^{-\alpha}$. This value is shallower compared to the typical slope ~ 2 from optical observations. One of our targets exhibit a turnover in the faint end of their LFs. We suggest that the small values of our slope are an imprint of a mass-dependent disruption model, unless the data is significantly affected by blending. We propose that a truncated cluster initial mass function is the reason for the bend in the LF at the faint end, since it is still 2 magnitudes above our completeness limit. We interpret the brightest star cluster-SFR relation as a reflection of a size-of-sample effect or an indication that the most massive star cluster (SC) is the brightest one or/and the youngest SC is simultaneously the most luminous. These results help to understand the SC formation and evolution.

Declaration

I declare that "*Super star cluster candidates in the star-forming regions of luminous infrared galaxies*" is my own work, that it has not been submitted before for any degree or examination in any other University, and that all the sources I have used or quoted have been indicated and acknowledged as complete references.

Rojovola Zara-Nomena Randriamanakoto

December 2010

Signed : .....

Acknowledgements

My foremost thanks go to God almighty for providing me the knowledge and courage to overcome the challenges since I started my study in South Africa.

I am really grateful to my supervisor Dr Petri Väisänen, for his valuable assistance and encouragement over the past two years. Thanks for suggesting me this interesting project and for being patient in guiding me throughout its accomplishment.

Thanks to my co-supervisor Dr Sarah Blyth for her support and to all the SAAO staff members as well as my office mates. I have thoroughly enjoyed my stay at the Observatory and I will never forget the good time that I have spent with the SAAO Outreach team.

I wish to extend my gratitude to the National Astrophysics and Space Science Programme for providing me very useful lectures and practical works. Thanks to the fellow students for your help and support, in particular Oyi, Tom, Okoh, Abiy, Mongwane, Zolile and Courage.

Thanks to the Malagasy community here in Cape Town, especially Ando, Andry, Ianja and Solohery. With you guys, I really feel at home.

I acknowledge the funding from the South African Square Kilometre Array. With the scholarship my dream came to reality: "becoming among the active Women in Science".

Finally, I would like to dedicate this thesis to Mom, Dad, Tojo and Onja. I am so proud for having you as my family. No matter the distance that separates us, you are always there for me.

Contents

List of Figures

List of Tables

Chapter 1

Introduction

1.1 Overview

This thesis reports the study of super star cluster candidates in interacting luminous infrared galaxies (LIRGs[1]) using observations in near-infrared (NIR) K_S-band[2] using adaptive optics (AO) imaging. Through the observations of super star cluster (SSC[3]) populations within the galaxies, the project aims to understand galaxy formation and evolution at higher redshifts by directly studying early star formation (SF) and its triggering in extreme environments in a representative sample of nearby interacting LIRGs. The SF environments in these galaxies are similar to what is expected more generally at higher redshifts. This work contributes towards answering the following fundamental questions: do the most massive SCs only form in starburst environments, or are massive SCs seen in those locations just because of larger number statistics? How do their lifetimes depend on the cluster initial mass function (CIMF) and local environment as well as on the global properties of the host galaxies? What fraction of the initial SC population end up in stable long-term bound structures such as globular clusters?

The main specific objectives of the thesis are *to derive the first-ever K-band luminosity function (LF)* [4] *of the massive star clusters and to establish a relation between the brightest star cluster and the galaxy star formation rate (SFR) in the NIR wavelengths.* These are crucial in order to understand the early SC formation, which is still under debate, and to answer the above mentioned questions. K-band AO imaging is unique in

[1] A LIRG is a galaxy with an infrared luminosity $L_{ir} = L(8 - 1000\mu m)$ range of 10^{11} - $10^{12} L_{\odot}$.
[2] Hereafter, we will be using K-band instead of K_S-band.
[3] In this thesis, the term star cluster (SC) refers to a super star cluster (SSC).
[4] A LF is the number of astronomical objects per magnitude or flux interval.

opening a new angle into the SC populations since studies thus far have been dominated by optical observations. K-band observations suffer significantly less from extinction effects allowing detection of the more obscured regions of the starbursts.

The results from a representative sample of ten local LIRGs are presented and discussed in this thesis. The data are from the first set of observations of an on-going multi-epoch local LIRG survey using NIR AO observations. The fields of view typically cover the central 8 - 12 kpc of galaxies, and the spatial resolution corresponds to 20 - 50 pc, depending on the target distance.

This thesis is divided into five major chapters and three appendices. The rest of this chapter provides an introduction to the field of study. Chapter 2 describes the data reduction and the methods that have been used to get the data for analysis. We give the details in deriving the K-band LF and the related photometric analysis in Chapter 3. In Chapter 4, we discuss the significance of our results. Finally, we summarize and conclude the main results from the thesis in Chapter 5 and we briefly describe our future work related to the topic. The appendices are intended to provide further information of the data analysis in Chapter 4.

1.2 Cosmic star formation history and galaxy evolution

Understanding the formation and the evolution of the Universe is a major outstanding challenge in astronomical and cosmological science. Scientists are devoted to solving the puzzle using theoretical simulations and multi-wavelength observations. The reconstruction of the cosmic star formation (CSF) history is a key ingredient in unveiling such a very complex laboratory. This is crucial as it will help to reveal when exactly the very first sources of light occured and to locate accurately the epoch of reonization in the cosmic timeline. This epoch is suggested to mark the beginning of any star formation in the Universe (Barkana & Loeb 2001).

Juneau et al. (2005) suggested that there is a strong dependence between cosmic star formation rate (CSFR) and the galaxy stellar mass. They stated that at higher redshifts the very massive galaxies contribute most to the comoving SFR density of the Universe. Results from cosmological N-body simulations showed that such behaviour is the effect

of "downsizing"[5] in time of galaxy formation: the most massive galaxies are most likely to host very active SF at an early epoch whereas, lower mass galaxies are the ones to form later and to exhibit high SFR at lower redshifts (Cowie et al. 1996). Following these ideas, one should first understand the formation and evolution of galaxies since they are the major building-blocks of the Universe and major components of the large scale structures (Gott et al. 2005).

One of the most important processes related to galaxy formation and evolution is merging. In a Λ cold dark matter (CDM) cosmological model (*i.e.* the Universe forms from a bottom-up scenario of its components), this phenomenon plays a major role by driving the formation of the most massive galaxies. The first observations from the *GOODS NICMOS*[6] survey reported that today's massive galaxies had previously undergone major and minor merger events at the early stages of the cosmic evolution (e.g. Bluck et al. 2009). This is in agreement with the results from a Monte Carlo merger-tree simulation which revealed that small dark matter (DM) haloes are gradually merging with time to form very massive ones (e.g. Okamoto & Habe 2000, Okamoto & Nagashima 2001). On the other hand, a well-known hypothesis is that an elliptical galaxy may be the result of a disk-disk collision of two isolated gas rich spirals (Toomre 1977). This was strongly supported by Wright et al. (1990) and Stanford & Bushouse (1991) who found reasonable de Vaucouleurs profiles $r^{-\frac{1}{4}}$ from the infrared radial brightness profiles of merger remnants in their observations.

Finally, mergers are believed to trigger a significant star formation rate due to tidal interactions. A study of the nuclear Hα emission of interacting spiral galaxies proved that this tracer of SFR is estimated to be 3 - 4 times stronger than that emitted in isolated systems (e.g. Keel et al. 1985, Bushouse 1986). At the same time, other studies found that the CSFR at high-z was much higher than locally, leading to speculation that it could be related to interactions (e.g. Madau et al. 1996, Smail et al. 1998).

Intriguing interacting systems that we should pay attention to are those of the luminous and ultraluminous infrared galaxies (U)LIRGs, believed to be amongst the extremes of

[5] Downsizing generally refers to the anticorrelation between the mass and the formation epoch of the stars in a galaxy.

[6] GOODS or Great Observatories Origins Deep Survey is a multi-wavelength campaign aiming to study the very distant Universe. HST/NICMOS is the instrument used for the NIR regime.

interaction induced SF (Lonsdale et al. 2006). In the local Universe, only a small fraction of the global SF density is contributed by these interacting galaxies. However, at higher redshift, $z > 1$, the fraction becomes dominant as they become much more frequent (Iono et al. 2009). In the following section, we will briefly review the (U)LIRG characteristics as well as their cosmic distribution from the literature.

1.3 Interacting LIRGs: our laboratory to probe SFR

In the early 1970's, the first mid-infrared observations reported that more energy is emitted in the infrared ($\sim$ 5 - 500 μm) than in the optical for some extragalactic sources (Low & Kleinmann 1968, Rieke & Low 1972). Later on, the launch of the *Infrared Astronomical Satellite (IRAS)* in 1983, a first all sky survey in mid and far- infrared wavelengths, enabled the discovery of many of these sources for the first time in the local Universe (Neugebauer et al. 1984). They had been missed during previous optical surveys because they only emit a small fraction of their energy in those wavelengths (Sanders & Mirabel 1996).

While Soifer et al. (1984) generally identified the new types of galaxies as "infrared galaxies"[7], Sanders & Mirabel (1996) sub-classified them according to their infrared luminosities L_{ir}. They estimated this parameter by considering the total IR flux F_{ir} emitted by the galaxy in all IRAS bands (12, 25, 60 and 100 μm) as expressed in Eq. 1.1:

$$F_{ir} \; = \; 1.8 \times 10^{-14} \; (13.48 f_{12} \; + \; 5.16 f_{25} \; + \; 2.58 f_{60} \; + \; f_{100}) \;\; [W m^{-2}] \qquad (1.1)$$

Combining the fluxes from the mid- and far-infrared wavelengths would lead to a more accurate estimate of the IR luminosity. Knowing the luminosity distance D and the total flux F_{ir} emitted by the galaxy, Sanders & Mirabel (1996) established a relation as defined in Eq. 1.2 to estimate its IR luminosity:

$$L_{ir} \; = \; L(8 - 1000 \; \mu m) \; = \; 4\pi \; D^2 \; F_{ir} \; L_{\odot} \qquad (1.2)$$

In their nomenclature, Sanders & Mirabel (1996) classify a galaxy to be a luminous infrared galaxy (LIRG) if $L_{ir} = 10^{11}$ - $10^{12}\, L_{\odot}$ and it will be an ultra-luminous IR galaxy (ULIRG) for $L_{ir} > 10^{12}\, L_{\odot}$. One of the most important works in showing evidence for a population of (U)LIRGs in the local Universe was done by Soifer et al. (1987) by analysing

[7] An object with $L(1 - 1000 \; \mu m)/L(0.1 - 1 \; \mu m) > 1$ is an infrared galaxy.

a sample of IR selected galaxies retrieved from the *IRAS Bright Galaxy Sample (BGS)*[8]. They compared the far-infrared luminosity function of the brightest IR galaxies with those of normal galaxies, starburst galaxies and Seyfert galaxies taken from literature. The results indicated that the emission from (U)LIRGs contribute significantly towards the cosmic IR background in the local Universe, hence they are a legitimate population in that cosmic volume. Since then, (U)LIRGs have been studied intensively in order to better understand their evolution and specific characteristics and their contribution to the CSF history.

1.3.1 IR luminosity, gas and morphology of LIRGs

While the re-radiation of the light in infrared wavelengths after dust absorption is the mechanism for the IR emission in these galaxies, the triggering of such a strong emission is still under debate (Elbaz et al. 2002). It is suggested that the presence of a high concentration of molecular gas in these systems plays an important role as it will induce active star formation such as nuclear starbursts. The latter will in turn dominate the luminosity of the whole galaxy (Sanders & Mirabel 1996). On the other hand, the presence of an active galactic nucleus (AGN) in the core of the galaxy may also contribute to the intense IR luminosity (Genzel et al. 1998).

Assuming that both SF and AGN phenomena are the source of LIRG energy, many different studies such as Soifer et al. (1987) and Genzel et al. (1998) proposed that in the local Universe, the ongoing star formation in the LIRGs generally dominate the luminosity over the AGN activity. A simple way to get an indication of whether an IR galaxy is AGN or SF-dominated is to use the IRAS flux ratio f_{25}/f_{60}: a higher fraction of such a ratio would result from warm dust within the galaxy which is consequently hosting, most probably, AGN activity (Soifer et al. 1987). Observations of galaxies from the *IRAS BGS* added with ULIRGs from Kim & Sanders (1998) revealed that the fraction of the luminosity from AGNs increases with an increasing infrared luminosity of the galaxy, whereas the main source of energy is powered by starburst activity at lower L_{ir}. Sanders & Mirabel (1996) explained this correlation with the variation of the galaxy morphology: the more a galaxy is disturbed, the higher will be the concentration of molecular gas fueling its central AGN activity. Subsequent studies such as the recent works by Imanishi (2008) and Goto et al. (2010) using the AKARI IR space-based telescope found the same

[8] *IRAS BGS* is a subsample of the *IRAS* all-sky survey. It is composed of the brightest galaxies at 60μm (Soifer et al. 1987).

correlation between the fractional AGN-SF energy contribution and the total infrared luminosity and they suggested that such a trend may be responsible of the "downsizing" in galaxy formation.

Various studies found thatt he infrared luminosity varies with the (U)LIRG morphologies. A review in Sanders & Mirabel (1996) showed that as the value of L_{ir} increases, the predominant morphology in the sample tends to vary from a normal and isolated galaxy with no major interaction to a merger galaxy with a molecular gas-rich content. While 32 % of LIRGs with log $L_{ir}/L_{\odot} \sim 11$ - 11.5 are classified to be normal galaxies, more than 66 % are already interacting systems for log $L_{ir}/L_{\odot} > 11.7$. It is believed that the further a galaxy is in its merger stage, the higher will be its star-formation efficiency due to the abundant gas accumulated during the tidal interactions and gas heating mechanism (e.g. Sanders & Mirabel 1996).

When merger or/and tidal interactions occur between two galaxies, their gas is expected to flow toward the galaxy nucleus. This would result to a higher gas surface density, Σ_{gas}. According to the well-known Kennicutt-Schmidt (KS) law, the SFR surface densities, Σ_{SFR}, gradually increases with Σ_{gas} as a power-law function (Schmidt 1959, Kennicutt 1998b):

$$\Sigma_{SFR} \propto \Sigma_{gas}^{N} \tag{1.3}$$

where $N \sim 1.4$ is the Schimdt power-law. Note that the value of N may change with respect to its molecular gas content: the more abundant the molecular gas within the galaxy is, the steeper will be its KS power-law index (Graciá-Carpio et al. 2008).

In this thesis, a common empirical relation by Kennicutt (1998a) which was derived under some assumptions (e.g. the AGN contribution is insignificant, L_{ir} of is the best SFR indicator of the galaxy) will be used. As can be seen in Eq. 1.4, the relation is used to convert the galaxy's L_{ir} into its SFR.

$$\frac{SFR}{M_{\odot}\ yr^{-1}} = 1.7 \times 10^{-10}\ L_{ir}\ [L_{\odot}] \tag{1.4}$$

1.3.2 LIRGs at higher redshift

Studies of the cosmic distribution of (U)LIRGs revealed that they are rare in the local Universe, whereas as we go further back in time they become more numerous (Hacking

et al. 1987). This ubiquity at high-z is thought to produce a large comoving IR luminosity density, about 70 times larger than today, hence leading to a significant contribution toward the CFR (e.g. Elbaz et al. 2002, Le Floc'h et al. 2005). Taken from Le Floc'h et al. (2005), Figure 1.1 shows the (U)LIRG IR luminosity distribution as a function of redshift. By converting L_{ir} into SFR using Eq. 1.4, it shows as well how the SFR varies as a function of z. These results are in correlation with the fact that the observed CSFR is very much higher in the early Universe than today (see Section 1.2), and it could be because merging is occuring everywhere in the early Universe.

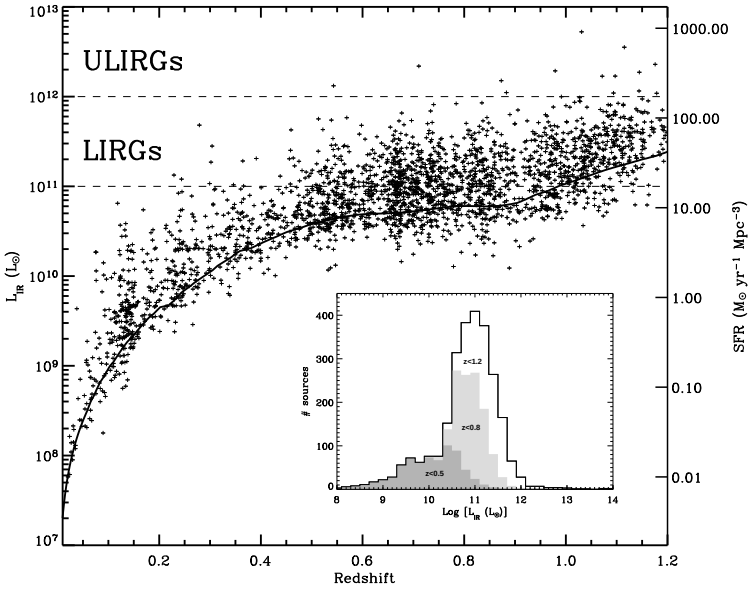

Figure 1.1: The (U)LIRG IR luminosity distribution observed with MIPS 24 μm as a function of redshift z. Using the relation in Eq. 1.4, the right vertical axis gives the SFR converted from the given L_{ir}. The inset corresponds to the IR luminosity of the same sources with the sample split in three sub-classes: $z < 0.5$, $z < 0.8$ and $z < 1.2$. Taken from Le Floc'h et al. (2005), the figure shows that (U)LIRGs are rare in the local Universe, whereas they become more numerous at high-z.

In contrast, however, Bell et al. (2005) and Elbaz et al. (2007) recently argued that only 30 % of the strongly star-forming galaxies at high-z are merging systems. More than half of the population of (U)LIRGs are rather normal spirals. These results suggest that the morphology of a galaxy, whether it is an interacting system or not, does not play an important role in the variation of the CSFR over the cosmic time. The decline of the CSFR could merely result from the amount of gas being exhausted (Noeske et al. 2007). The

reasons for the rapid decline of the number of (U)LIRGs over the cosmic space density as well as the sudden drop of the CSFR in the present Universe are currently under debate.

Local interacting LIRGs are specifically chosen to be the targets of this study because of their internal SF environment, which is often associated with violent and extreme star-formation activity such as the formation of super star clusters (Larsen 2002). This will be outlined in the next section. Furthermore, the external environments of local LIRGs could also be similar to what is happening at higher-z. Studies of the *GOODS* galaxies by Elbaz et al. (2007) revealed a reversal of the SF-density relation at $z \sim 1$: while the SFR of galaxies generally decreases with the environment richness in the local Universe, the opposite case occurs at higher redshift due to the process of large scale structure formation. However, it is suggested that this relation would be the same at both redshifts for LIRGs specifically (Tekola, PhD, private communication). Therefore, they are believed to be good analogs of higher-z galaxies such as $z \sim 1$ blue cloud galaxies (e.g. Elbaz et al. 2007). To better understand the galaxy evolution in the earlier Universe and the large scale structure formation, it is thus useful to start the observations and analysis with the closest luminous and star-forming sources.

1.4 Super star clusters in interacting LIRGs

It is believed that most stars in galaxies are born in clusters, but much remains unclear on the early star cluster evolution, and hence galaxy evolution (Lada & Lada 2003). More observations are required to better understand the mechanism behind it. The discovery of unfamiliar star clusters in a peculiar galaxy in the 1980's motivated even more researchers to solve the puzzle.

When pointing the Hale 5-m reflector at Palomar on a peculiar galaxy, NGC 1569, Arp & Sandage (1985) identified a new variety of very luminous star clusters which appeared to be both massive and young (see Table 1.1). The same objects were amongst the very first new discoveries from the *Hubble Space Telescope*, imaging NGC 1275 in the central galaxy of the Perseus cluster (Holtzman et al. 1992). Thereafter, subsequent works started to focus more on the features and dynamics of these newly found star clusters. Arp & Sandage (1985) adopted the term "super star clusters" (SSCs) for these objects. But other names such as "young massive clusters" or "blue populous clusters" also refer to the same star clusters (Larsen & Richtler 1999). In this thesis, we will be using the name

given by Arp & Sandage and we note that the term SC and SSC refer to the same objects.

SSCs are often constrained to interacting systems. However, they can also be found in other environments as long as there is a high level of star formation, which is a major ingredient for these star clusters to be born (Iono et al. 2009). In fact, apart from mergers and interacting systems, previous studies revealed that circumnuclear star-forming rings (e.g. Benedict et al. 1993) and nearby dwarf galaxies (e.g. O'Connell et al. 1994) also host these star clusters. The difference is just that the population of SSCs is much larger in galaxies exhibiting an extreme starburst environment with a violent SF such as interacting LIRGs (Larsen 2002).

SSCs have been probed intensively in the Magellanic clouds and in the very nearby galaxies (Elson & Fall 1985). Amongst the well-known systems are M51 (8.2 Mpc) by Bik et al. (2003) and M83 (4.5 Mpc) by Chandar et al. (2010). Most of the observations were done in the optical wavelengths using the *Hubble Space Telescope*. Multi-wavelength observations have been carried out to study SSCs in the Antennae galaxy (NGC 4038/4039): including the radio, infrared, optical, ultraviolet and X-ray wavelengths. This system has been the most active extragalactic scale laboratory to study SSCs, as it provides a large statistical sample of these star clusters (at least thousands were detected) (Whitmore et al. 1993). With an infrared luminosity log $L_{ir} = 10.84$, if at a distance of 21.5 Mpc, this interacting system is almost classified as LIRG (Sanders et al. 2003). So far, researchers focussed more on SSCs within the nearby non-LIRG extragalactic systems ($D < 25$ Mpc), simply because it is much easier, and there are only few studies probing SSCs in the more distant local LIRGs. Arp 299 (IC 694/NGC 3690) with log $L_{ir} = 11.88$ at 47.7 Mpc, Haro 11 with log $L_{ir} = 11.22$ at 81.2 Mpc and the Bird galaxy (IRAS 19115-2124) with log $L_{ir} = 11.87$ at 206 Mpc have been targets to study young massive clusters by Lai et al. (1999), Adamo et al. (2010) and Väisänen et al. (2008), respectively. These works started to combine optical observations with the NIR adaptive optics imaging for a better analysis of SSCs.

Despite the significant work already done over the past decades, the early stages of evolution of SSCs still remain unclear. However, it is crucial to carry on active research of these SCs in order to improve our current knowledge of the evolution and dynamics of the SSCs and their host galaxy, as well as a good explanation of star formation in general. The aim of this work is to contribute to understanding the above matters.

1.4.1 Characteristics

SSCs are believed to be the progenitors of the present day globular clusters (GCs). Previous studies revealed that with their extreme characteristics, they are potential proto-GC candidates (e.g. Johnson 2005). Moreover, these star clusters are a good starting point to investigate the formation of massive stars and SF in general since they are classified to be amongst the most extreme types of star clusters and that each one of them may be composed of up to thousands of massive stars (Johnson 2005). Over the past decades, results from multiple observations have agreed that the very luminous star clusters are massive ($M \sim 10^5 M_\odot$) and very young as well: from 10 or less to 100 Myr old (e.g. Ho 1997, Whitmore 2000). Their natal environments, which are violent and actively star-forming regions, offer a high probability for the star clusters to acquire these extreme properties. Taken from Johnson et al. (2009), Table 1.1 compares some physical SSC properties with those of GCs and embedded clusters[9]: SSC characteristics differ from those of embedded clusters, but are similar to those of GCs. It is suggested that some of the most massive and dense ones will end up being the progenitors of young globular clusters (de Grijs 2005).

Type	N_* [a]	Mass ($M_\odot$)	d_h [b] (pc)	ρ_h [c] ($M_\odot\ pc^{-3}$)	Age (years)
Globular cluster	$> 10^5$	$10^{3.5}$ - 10^6	0.6 - 8	10^{-1} - $10^{4.5}$	$> 10^9$
Embedded cluster	35 - 2000	350 - 1100	0.6 - 2	1 - 5	$10^6 - 10^7$
SSC	$> 10^5$	10^5 - 10^6	6 - 10	$\sim 10^4$	10^6 - 10^7

[a] The number of cluster members
[b] The half-light diameter of the cluster
[c] The mean density inside the region containing half of the cluster mass

Table 1.1: This table taken from Johnson et al. (2009) shows that SSC characteristics differ from those of embedded clusters, but are similar to those of GCs.

Compared to the visual absolute magnitude of a young star cluster, e.g. R136 in the Large Magellanic Cloud (M_V = -11.3 mag), SSCs are much brighter in M_V ranging up to -15 mag (O'Connell et al. 1994). An SSC at the age of $\sim$ 10 Myr old would have

[9] Embedded cluster is an open cluster that is still partially or fully enclosed in a interstellar gas or dust cloud.

-13 mag visual absolute magnitude depending on its mass. However, after 10 to 15 Gyr, the same star cluster will be much fainter, by 6 to 7 visual magnitudes, due to stellar evolution (Bruzual A. & Charlot 1993). While their ages are generally ranging from a few Myr to several hundred Myr (Ho 1997), most SSCs only survive until the age of $\sim$ 10 Myr. Older clusters are those which were lucky enough to survive infant mortality and other effects of cluster disruption (Goodwin & Bastian 2006, de Grijs & Parmentier 2007). These phenomena responsible for short term survival of SSCs will be further discussed in Section 1.4.3.

Using a length scale such as the effective radius, r_h, a typical SSC size is approximately 3 - 5 pc, which is slightly larger than a GC, as can be seen in Table 1.1. Based on that compact size, Ho (1997) suggested that SSCs are most likely to be gravitationally bound. Their photometric properties revealed that the cluster mass is between 10^5 to 10^6 $M_\odot$ with a density $\sim 10^4$ $M_\odot$ pc^{-3} (Ho 1997).

Finally, SSCs are commonly used to trace the current star formation history of their host galaxy. This is because they are mostly located wherever there is very active SF going on, and they are very young and bright star clusters (Bastian 2008). Moreover, Weidner et al. (2004) derived a relation which tightly correlates the luminosity of the brightest star cluster with the global galaxy SFR. One goal of this thesis is to test whether a similar relation exists in the near-infrared wavelengths, where dust extinction uncertainties are smaller.

1.4.2 Formation

As mentioned earlier, many observations and an exciting debate are still on-going, aiming to provide the best explanation of the early stages of evolution of massive star clusters. The fact that this phase is often enshrouded in the very dusty regions of the galaxy makes them difficult to be probed, especially if the observation is done in the optical wavelengths or the instrumentation used is not very sensitive (Johnson 2005). We will attempt to highlight SSC formation in this section, based on recent studies of the subject.

It is believed that SSCs follow the same process of star formation as massive stars. Taken from Johnson (2005), Figure 1.2 compares the evolutionary stages of an individual massive star and a super star cluster. Due to the lack of observations, the layout

illustrates a very simplified scenario of the SSC formation. In fact, the preliminary stages within the dashed box have not yet been confirmed observationally. Nevertheless, the figure indicates that there are several analogs between the two types of objects.

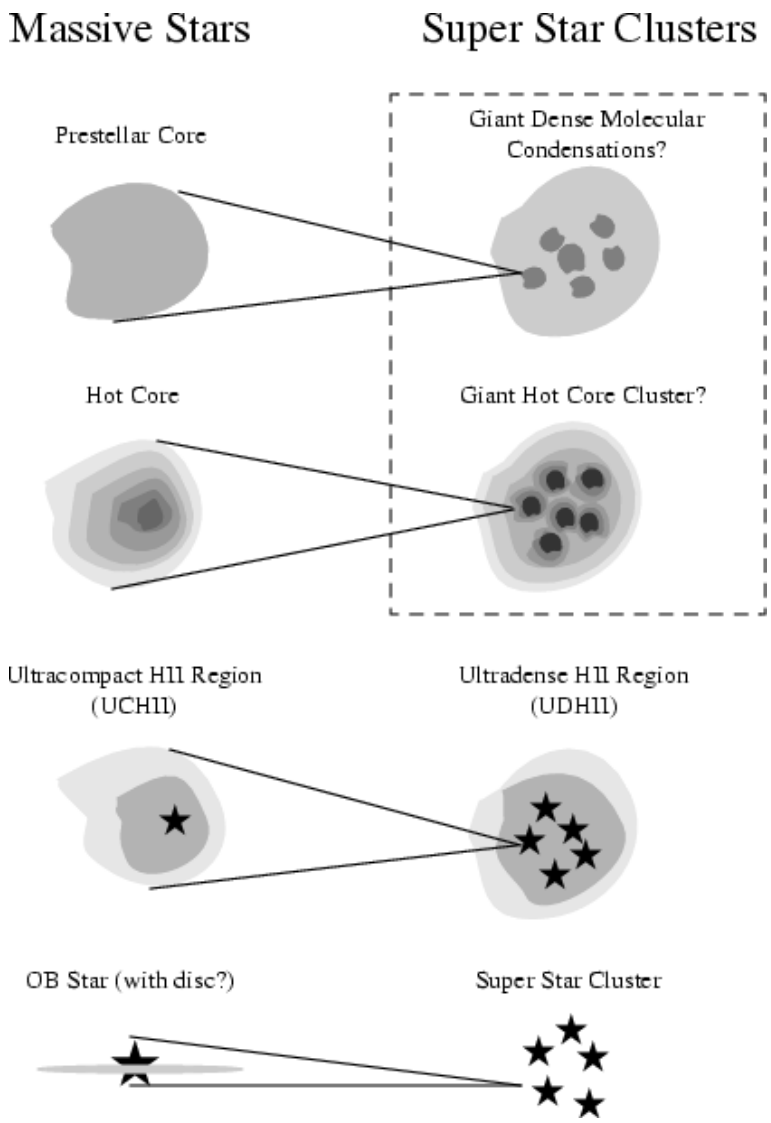

Figure 1.2: Comparison of the evolutionary stages of an individual massive star and a super star cluster. The preliminary stages of an SSC within the dashed box have not yet been confirmed observationally. This layout is from Johnson (2005).

A pre-stellar core is required for a massive star to form, whereas the condensation of a dense giant molecular cloud (GMC) with a high global pressure ranging up to

$P/k_B \sim 10^{8-9}\ Kcm^{-3}$ is necessary to give birth to an SSC[10]. This high pressure, arising from the large-scale shocks which are the results of the direct collisions or strong gravitational interactions occuring in the host galaxy, would be the major ingredient to cause the massive core GMC to be tightly bound (van den Bergh 2004). In his review, Larson (2003) pinpointed that this star-forming cloud core presents an excess in its angular momentum which would be too large to be observed in a single star. Therefore, when gravity and turbulence dominate against the thermal pressure, the massive molecular cloud would split up into a clump of massive stars. Later, the ionization of these newly born massive stars will in turn create a very dense HII region surrounding the natal SSC. As illustrated in Figure 1.2, this extreme HII region is simply a scaled-up version in mass and luminosity of a galactic ulracompact HII region. We should note that these analogies only hold if the time-scale of the cluster formation is $\sim$ 0.1 - 1 Myr (Johnson 2005).

1.4.3 Evolution

Once a star cluster is formed, its chance of survival will still depend on various mechanisms. Many studies suggest that they endure cluster disruption in their first few Myr of lifetime, such as gas expulsion and stellar evolution (e.g. Lada & Lada 2003, Goodwin & Bastian 2006). The first form of disruption happens during the supernovae explosion phase of the most massive stars leading to a significant mass-loss of the SC. Consequently, it will undergo a violent relaxation and will become gravitationally unbound. If the SC is unlikely to reach a new equilibrium within a short time scale, it will not survive the mass-loss due to stellar evolution and the tidal effects (Bastian & Goodwin 2006). This phenomenon called *infant mortality* would be the cause of a significant number of SSCs being destroyed at $\sim$ 10 Myr of age in the widely studied Antennae system (Whitmore 2004). On the other hand, if the subsequent cluster disruption (e.g. stellar evolution) is not so significant and if the gas expulsion only occurs within a few crossing-times, the SC will endure an *infant weight loss* since it will be mass-segregated while searching for a new equilibrium: the revirialized SC will acquire a new escape velocity V_e^{new}. Therefore, low mass stars with higher velocity dispersion than V_e^{new} will escape from the SC to form an infrared light excess at larger radii, whereas those having lower velocity dispersions, which are mainly the massive stars, will tend to expand looking for a new virial equilibrium increasing the SC core radius (Goodwin & Bastian 2006).

[10] P is the pressure of the natal cluster and k_B is the Boltzmann constant.

In the case that SSCs would have reached a new virial equilibrium at the age of $\sim$ 40 - 50 Myr (Bastian & Goodwin 2006), they are likely to become the potential progenitors of the present day GCs (de Grijs 2009). This idea arises from the fact that they tend to have the same properties as that of proto-GCs; with a similar size ($\sim$ 5 pc) and a mass somewhat higher than that of a GC. These extreme star clusters are suggested to evolve with time to form the old building blocks of the Universe. However, a long term survival of an SSC over a Hubble time will still depend on the stellar initial mass function (IMF) as well as the intensity of the cluster disruption (de Grijs 2009). The shallower the IMF slope is, the smaller the chance for the star cluster to survive for a Hubble time to become a globular cluster. A steep slope is required for a long-time survival of the star cluster because gas expulsion as well as stellar evolution would favor the acceleration of its expansion. If the latter happens, low-mass stars will therefore disperse to form field stars, since they are the most vulnerable to the cluster disruption. Moreover, this deficit in low-mass stars will make the cluster mass function shallower. All these factors will lower the chance for the star cluster to become the precursor of a globular cluster because it would rather likely be dissolved (de Grijs & Parmentier 2007).

1.5 What can we learn from the SSC luminosity function?

In this thesis, a luminosity function (LF) is the number of super star cluster candidates per magnitude or flux interval. It is a very common tool used to study the properties of stars, star clusters or galaxies. Over the past decades, various studies have shown that the LF of open and globular clusters are quite different. While the former is still under debate whether it follows a power-law or a gaussian function, the latter is strongly shown to be well-fitted with a log-normal shape (e.g. Elmegreen & Efremov 1997, Fritze-v. Alvensleben 1999, Anders et al. 2007).

Fitting a function to the LF shape is crucial as it helps to determine the mode of formation and disruption of the star cluster. It is also used to constrain the cluster initial mass function CIMF [11] and may even provide some clues of the proto-globular cloud mass-spectrum (e.g. Gieles 2010, Parmentier & Gilmore 2007). Early theoretical and observational studies agreed that the LF of a population of star clusters is well-approximated to first order by a universal single power-law (e.g. Elmegreen & Efremov

[11] CIMF is the mass distribution of a population of clusters in terms of their theoretical initial mass.

1997, Lada & Lada 2003, Gieles et al. 2006a) of the form:

$$N(L)dL \sim L^{-2}dL \tag{1.5}$$

It is suggested that the above function is simply the reflection of the cluster mass function following the same distribution with the same value of the power-law index:

$$N(m)dm \sim m^{-2}dm \tag{1.6}$$

Moreover, the GMC mass-spectrum will likely obey the same function but with an index varying between 1.5 to 2.5 for a GMC located in the Local Group of galaxies (e.g. Rosolowsky 2005). This is because of the tight correlation that was established by Parmentier & Gilmore (2007) between the initial mass, m_{init}, of a gas-free bound cluster and the mass, m_{cloud}, of the gas cloud progenitor.

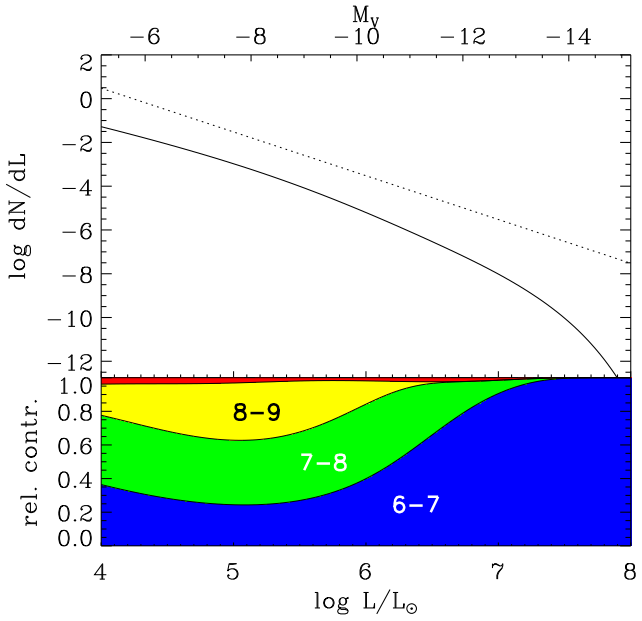

Figure 1.3: The upper panel of this figure taken from Gieles (2010) represents a star cluster LF based on a theoretical simulation (solid line). It shows that the model does not follow a universal single power-law with $\alpha = 2$ (dotted line) at higher magnitude range. The lower panel gives the relative distribution of star clusters with respect to their age groups as a function of the magnitude bin. The inset numbers represent the different age groups expressed in Myr.

However, some recent observational analysis and theoretical models cast some doubt on

these conclusions. As an example, Figure 1.3 taken from Gieles (2010), clearly indicates that the inde x of the LF model deviates from 2, though it follows quite well the universal power-law LF (dotted line) at the faint end. Gieles (2010) rather suggests a double power-law to better fit the star cluster LF. Moreover, results from recent studies reveal that a power-law LF will not always correspond to a MF following the same distribution. And in the case they both do follow a power law, it would not necessarily mean that they will have an identical power law index. Because a magnitude bin may include star clusters with a wide range of ages, the mass-to-light ratio will be age dependent. This is illustrated in the lower panel of Figure 1.3: star clusters with different age groups may be present all over the magnitude bins.

A recent review by Portegies Zwart et al. (2010) emphasized that the power-law index α is greater than 2 at the bright end of the LF. This simply arises from a relation determined by Whitmore (2003), between the luminosity L_{max} of the most luminous object with the total number N of the clusters as given by:

$$L_{max} \sim N^{\eta} \tag{1.7}$$

Assuming a pure power-law with $\alpha \sim 2$, η would be equal to 0.75. And using the relation by Hunter et al. (2003), which is $\eta = \frac{1}{\alpha - 1}$, such a value would correspond to $\alpha \sim 2.4$ mapping only the brightest cluster of the sample. Portegies Zwart et al. (2010) interpreted Eq. 1.7 to be the result from a size-of-sample effect: the formation of the very bright cluster of the sample is not constrained by any physical conditions. However, a similar relation established by Weidner et al. (2004) and Bastian (2008) and which is associated with the L_{max} - SFR relation would lead to a mass-to-light ratio dependance on L_{max}.

Another important result that we should take note of from various observations of different galaxy environments, is that the power-law index α is generally varying from 1.8 to 2.8. It could depend, for instance, on the galactic environment, the filter used, as well as the techniques which have been used to derive the LF (e.g. Gieles 2010). In contrast, a recent study of SSCs in M83 by Chandar et al. (2010) argued that α is mostly insensitive to these different factors.

It is obvious from these various results that more work is required to provide reliable information from the luminosity function with regard to the star cluster properties.

Chapter 2

Observations and data reduction

2.1 Observations

2.1.1 The sample

In this work, we analyse a representative sample of ten LIRGs from an ongoing NIR AO survey (Väisänen et al. 2009). With redshifts of $0.01 < z < 0.05$, they are situated in the local Universe ($45 <$ D (Mpc) < 207). Equatorial and galactic coordinates as well as the luminosity distance of the targets are retrieved from the NASA/IPAC Extragalactic Database (NED)[1] as listed in Table 2.1. The logarithmic values of their IR luminosities $L(8 - 1000\ \mu\mathrm{m})$, as defined by Eq. 1.2, are originally retrieved from the *IRAS Revised Bright Galaxy Sample* which is published by Sanders et al. (2003) and they range from 11.24 to 11.88 solar luminosities on a logarithmic scale. Strong LIRGs are often interacting systems although they might exhibit different merging stages, and that is the case here too. As already mentioned in Section 1.4, interacting LIRGs provide a good site for the formation of massive star clusters because they are often associated with violent star formation (Larsen 2002). Focussing our study in local LIRGs will help us to better understand the ULIRGs which contribute strongly to the SF of the Universe at high-z. SF environments in local LIRGS are suggested to be similar to what is expected more generally at higher redshifts (e.g. Le Floc'h et al. 2005).

2.1.2 Data acquisition

The data were captured in a K-band filter using two different NIR ground-based telescopes located in Chile and Hawaii. Adaptive optics imaging using both natural and laser guide stars of these telescopes were used: the NAOS-CONICA on the ESO Very

[1] See http://nedwww.ipac.caltech.edu/

Large Telescope (VLT/NACO) and the ALTAIR NIRI on the Gemini-North telescope (GEMINI/ALTAIR). With such instruments, the dusty regions and the inner parts of the galaxy can be well resolved, allowing a better estimate of the amount of SF from these regions. So far, there are very few NIR studies of SSCs compared with the optical ones (e.g. Alonso-Herrero et al. 2006, Väisänen et al. 2008, Adamo et al. 2010). Väisänen et al. 2009 revealed that NIR data are ideal for probing the most massive star clusters since there is less extinction at these wavelengths. However, very young SSCs may be missed because a K-band filter is more sensitive to red sources (though any significant "red excess" could counteract this, Adamo et al. 2010).

Name [a]	RA [b] ($J2000$)	DEC [c] ($J2000$)	l [d] ($degrees$)	b [e] ($degrees$)	D [f] (Mpc)	$\log L_{ir}$ [g] ($L_\odot$)
MGC +08-11-002	05 40 43.7	+49 41 41	161.668	9.958	79.9	11.41
IC 694	11 28 27.3	+58 34 43	141.903	55.387	57	11.88
NGC 3690	11 28 32.2	+58 33 44	141.903	55.406	45.3	11.88
UGC 8387	13 20 35.3	+34 08 22	82.928	80.599	101	11.67
CGCG 049-057	15 13 13.1	+07 13 32	8.890	50.954	56.4	11.27
IRAS F16516-0948	16 54 24.0	-09 53 21	9.504	20.501	94.8	11.24
IRAS F17138-1017	17 16 35.8	-10 20 39	12.241	15.675	72.2	11.42
IRAS F17578-0400	18 00 31.9	-04 00 53	23.449	9.419	57.3	11.35
IRAS 18293-3413	18 32 41.1	-34 11 27	0.148	-11.307	74.6	11.81
IRAS 19115-2124	19 14 30.9	-21 19 07	16.074	-14.425	206	11.87

[a] Common name of the galaxy
[b] Equinox J2000 right ascenscion
[c] Equinox J2000 declination
[d] Galactic longitude
[e] Galactic latitude
[f] Luminosity distance
[g] 8 - 1000 μm IR luminosity

Table 2.1: Equatorial and galactic coordinates of the observed sample are shown in this table. The luminosity distance is retrieved from NED under the following cosmological assumptions: $H_o = 73 \mathrm{kms}^{-1}\mathrm{Mpc}^{-1}$, $W_{matter} = 0.27$ and $W_{vacuum} = 0.73$. The IR luminosity is as estimated by Sanders et al. (2003) by setting a slightly different cosmological parameters.

The number of individual frames used to get the final combined image and the total integration time in *sec* are given in Table 2.2 for each target. For AO correction, natural guide stars were used for the VLT/NACO data, whereas laser guide stars for the GEMINI/ALTAIR ones.

VLT/NACO data

IRAS 18293-3143 and IRAS 19115-1114 were our first SSC pilot study (Väisänen et al. 2008). Observed with the K-band NACO AO system on the VLT UT4 (with a plate scale of $0.027''\text{pix}^{-1}$ from the S27 camera), their final images have a field of view of $27''$ with a full-width-half-maximum FWHM $\sim 0.1''$ for the point sources. Each individual frame was taken with an exposure time of 90 *sec*. More details of the observations are given in the papers Mattila et al. (2007) and Väisänen et al. (2008).

GEMINI/ALTAIR data

The other targets are from an on-going multi-epoch survey from GEMINI/ALTAIR using a K-band filter. The survey is mainly intended to search for dusty core-collapse supernovae in local (U)LIRGs. The pixel scale of a frame is $0.022''\text{pix}^{-1}$, yielding a field of $22'' \times 22''$. The data which are already available have a resolution of $\sim 0.1''$ (Kankare et al. 2008). Each individual frame has an exposure time of ~ 30 *sec*.

Instrument	Name	Nb frames	Exp.time (*sec*)
GEMINI/ALTAIR	MCG +08-11-002	38	1140
	IC 694	40	1260
	NGC 3690	73	2192
	UGC 8387	48	1440
	CGCG 049-057	56	1680
	IRAS F16516-0948	40	900
	IRAS F17138-1017	33	990
	IRAS F17578-0400	49	1470
VLT/NACO	IRAS 18293-3413	41	1230
	IRAS 19115-2124	47	1410

Table 2.2: Log of the observations of the sample. GEMINI/ALTAIR and VLT/NACO instruments were used for a high resolution NIR AO imaging of the targets. This leads to a resolution of $\sim 0.1''$ for point sources in both cases.

2.2 Data reduction and photometry

For this thesis, data from VLT/NACO were ready to be analysed. However, GEMINI/ALTAIR data reduction was required, starting from the derivation of the final co-added image of each target. Preliminary steps such as flat-fielding and exposure-time calibration were already performed by Erkki Kankare using tasks of IRAF/NIRI package (Kankare et al. 2008).

The IRAF/NIRI[2] package is specifically built to reduce the raw frames from the ALTAIR/NIRI observations. The first crucial process for any further reduction is to run the raw data using NPREPARE. The other tasks will not run if this preliminary step has been skipped. In running this task, variance and the data quality planes will be also created. Non-linear or saturated pixels in the image are corrected with NRESIDUAL. While normalized flat fields and a bad pixel mask are created via NIFLAT, the sky images are instead constructed with NISKY. The task NIREDUCE is used for flat-fielding, dark frame and sky subtraction. After going through these processes, each individual frame with a scaled exposure time is ready to be combined to form the final NIRI co-added image.

2.2.1 GEMINI/ALTAIR final co-added images

Excluding the bad frames

For good photometry and to improve the signal-to-noise ratio of the final combined image, not all the frames taken during the observations were included. A more accurate co-added image having a good quality can be derived by imposing some criteria which will determine whether a frame will be included or not to form that final image.

An individual frame will be qualified as being a *bad frame* if it fits in the following situtations simultaneously:
(1) The standard deviation σ of an isolated region of the frame is too high compared to the other ones. Electronic noise or a strong turbulence of the atmosphere may lead to such a value. Therefore, the corresponding frame will be composed mainly of noise. The size of the region was chosen to be large enough to avoid any biased value of σ.
(2) The FWHM of point sources which can be identified all over the frames is very large

[2]More information are available at http://www.gemini.edu/sciops/data/IRAFdoc/niriinfo.html

compared to the other ones. This large value means that the frame was taken during a night with bad seeing or that the AO correction was not fully successful.

Once the bad frames are excluded, a method is adopted to perform the de-striping process in order to minimize the horizontal noise.

Minimizing the horizontal noise

If the dark frame subtraction did not work very well during the preliminary steps of the data-reduction, the frames will probably include horizontal noise patterns, *i.e.* stripes. To minimize the noise, we built a python script which required the individual frames as input, and returned as output the same frames but with the noise attenuated. The counts of the output frame were derived using the following formula:

$$New\_count \; = \; Original\_count \; - \; MEDIAN \tag{2.1}$$

For each row of the original frame, its median, *MEDIAN*, is estimated in order to derive the New_count by subtracting the $Original\_count$ from that estimated value. However, to get a smooth background, we have to be careful because a high value of *MEDIAN* will be estimated for some rows, due to the counts corresponding to the nucleus of the galaxy. Therefore, we introduced a certain cutoff limit: for a given row, only the counts which are less than that cutoff limit will be considered to estimate the median of that row. The cutoff is given by:

$$cutoff \; = \; MODE \; + \; \sigma \tag{2.2}$$

where $MODE$ is the mode of the whole frame and σ is the standard deviation of the same region which was previously used to check if the frame is noisy or not.

Interpreting Eq. 2.1, one can deduce that a constant "sky" level per row will be subtracted as well for the output frames. Although the effect of the de-striping can be observed at each individual frame, it will be much more evident after combining them into a single frame as shown in Figure 2.1.

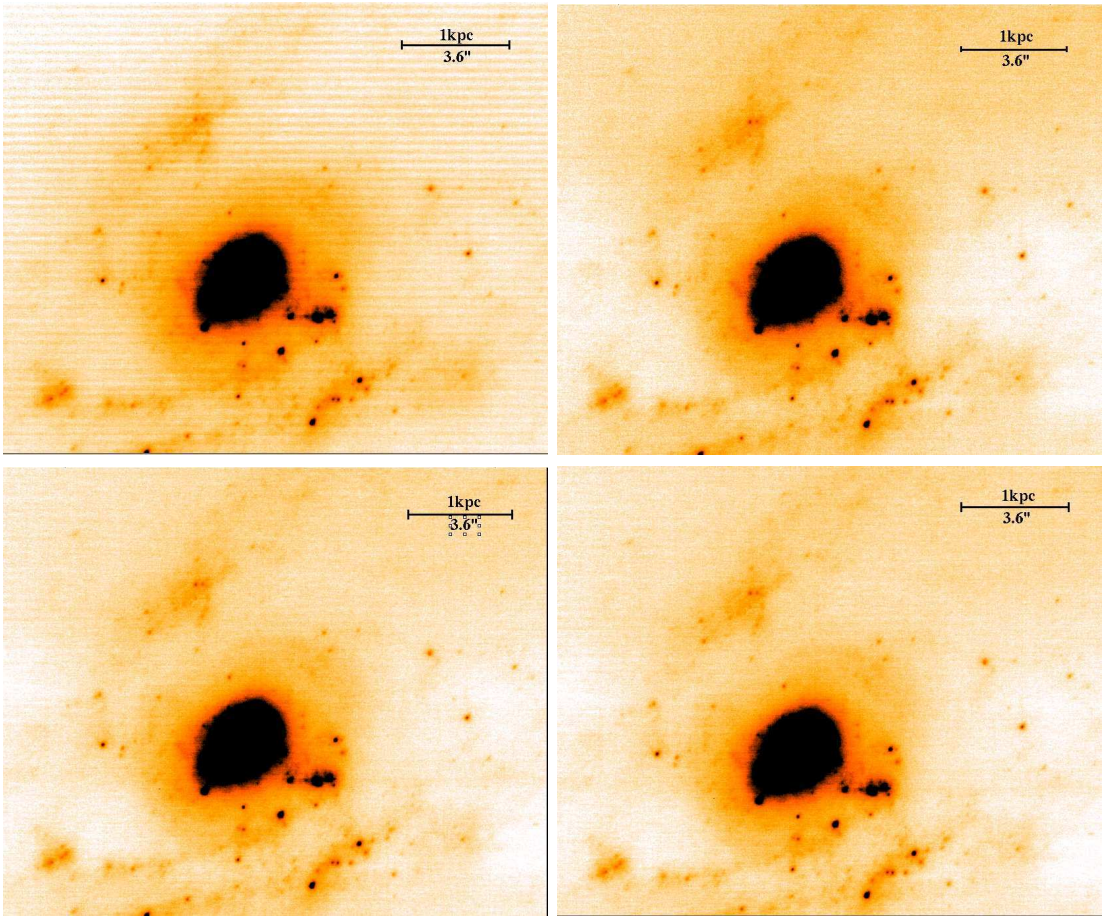

Figure 2.1: Different final co-added images of IC 694. If we did not minimize the horizontal noise before combining the individual frames, we get a co-added image as seen in the upper left of the figure. However, we get the other images shown in the same figure after de-striping. The only difference between these images is that they do not have the same value for the cutoff limit. With $cutoff = MODE + 5\sigma$, we get the image in the upper right, for $cutoff = MODE + 3\sigma$, the one in the lower left and for $cutoff = MODE + \sigma$, the co-added image looks like the one in the lower right.

From the final co-added images illustrated in Figure 2.1, one can clearly see that the lower the cutoff limit is, the higher is the attenuation of the black band which appears as a white band for a negative scaling, in the middle of the frame which comes from the large pixel values corresponding to the galaxy nucleus. Therefore, we decided to use the image in the lower right, where $cutoff = MODE + \sigma$, for further analysis since that image has the more attenuated black band compared to the others.

Combining the individual frames

Once the horizontal noise is minimized and the bad frames excluded, the IRAF task IMCOMBINE was used to align and to combine the individual frames. After using various algorithms to output different types of combined images, we estimated and compared the new value of σ in these images. As a result, we decided to keep the one which was "average-combined" with the parameter *reject* set to be "avsigclip" because it corresponds to the lowest value of σ, which means that the background is the least noisy with this method. In addition, "avsigclip" is efficient in rejecting cosmic rays and it is usually recommended for combining a small number of individual frames. We note that we used the task XDSHIFTS to estimate the offsets between the individual frames. This task requires an input file which will store the coordinates of a common bright source in the field from each individual frame.

2.2.2 Astrometry calibration

Because of its small field, and very small number, if any, of bright stars, it is difficult to make a direct astrometry calibration of the GEMINI/ALTAIR final co-added images via the *Guide Star Catalog II (GSC II)*, or other star catalogs. Therefore, using the IRAF task CCMAP, we first calibrated the corresponding HST/ACS data, which have a larger field of view, of the same target fields and then using the same task they will be the ones to be used as a reference while adding the World Coordinate System (WCS) in the FITS header of the NIR imaging.

Astrometry calibration of an input image with CCMAP is basically done by matching pixel and celestial coordinates of the same point sources. Pixel coordinates are from the input image itself, whereas the celestial ones are taken either from an archival catalog such as *GSC II* in our case or from the FITS header of another image mapping the same target. The calibration works in the same way as a fitting process where the smaller is the number of point sources to compose the coordinate list, the higher will be the uncertainty of the results. Running CCMAP updates the image coordinate system. Therefore, the WCS will be added in the FITS header of the input image.

For the following targets: IRAS F17578-0400, IRAS F16516-0948, CGCG 049-057 and MCG +08-11-002, either the HST/ACS data could not be retrieved or they do not have any obvious common point sources. Therefore, we used the software GAIA as it provides

an option which is able to add the WCS coordinates of the image. One of the calibrated images using the CCMAP task was used to copy the WCS in the remaining uncalibrated images. The RA and DEC as well as the X and Y positions in pixel values of the center of the target were required to get the real WCS info of these images. The RA and DEC were retrieved from the 2-MASS K-band survey, and the corresponding X and Y coordinates were determined by gaussian smoothing the NIR image and finding the K-band peak flux.

2.2.3 Object detection

SExtractor is an astronomical software package well-suited for object detection (Bertin & Arnouts 1996). Through a set of parameters in the configuration file, it has an ability to deblend overlapping objects and to detect a large number of sources in the field. We used this software since our aim is to detect as many SSC candidates as possible. The critical input parameters in the configuration file had to be set carefully. They were chosen based on the following criteria:
(1) All the point-sources located in the star-forming regions of the galaxy should be detected. They are most likely to be SSC candidates which are the targets of this study.
(2) Two distinct sources which are close enough but can still be identified individually by visual inspection should be detected separately when running the software.
(3) Spurious sources are only expected to be overabundant in the outskirts of the frame because of noise. They will mostly be excluded since the edges of the frame will be omitted for further analysis.

Therefore, in order to get the appropriate configuration file which would fulfill the above criteria, we ran SExtractor many times on the input image using different sets of parameters for further comparison. After each compilation, we recorded the number of the extracted objects and we checked whether the suspected SSC candidates were mostly detected by the software. In addition, we adopted a method which enabled to separate spurious and real sources. This was done by running SExtractor on the inverted version of the image (*i.e.* multiplying all the pixels values in the frame by -1). In that case, the parameters are set to be the same as those used to run the real input image. This method allowed us to estimate the percentage of spurious objects with respect to the total number of detected objects and it identified these junk sources amongst the overall extracted objects from the real image. After repeating many times the same procedure,

we finally derived the appropriate configuration file in comparing the results given from the multiple compilation. The chosen set of parameters was the one corresponding to the output catalog which mostly extracted real objects and simultaneously had a minimum number of junk sources. Because the noise and background characteristics are somewhat different in each final frame, we do not expect exactly the same parameter for each galaxy. As shown in Table 2.3, we chose a small value for the parameter DETECT_THRESH for

Name	DETECT_THRESH	BACK_SIZE
MCG +08-11-002	2	14
IC 694	2	10
NGC 3690	1.3	12
UGC 8387	1.5	12
CGCG 049-057	1.1	8
IRAS F16516-0948	1.0	10
IRAS F17138-1017	1.5	10
IRAS F17578-0400	1.3	11
IRAS 18293-3413	2	11
IRAS 19115-2124	2	10

Table 2.3: The values of some critical parameters used to run SExtractor for each target. We note that the parameters for each galaxy are not the same since noise and background characteristics in each frame differ from one another.

each target, to optimize detection of faint SSC candidates. In addition, we found that the data extraction is quite good for a lower value of DETECT_THRESH combined with an upper value of DETECT_MINAREA. We have set the latter parameter to be equal to 10 while running SExtractor on the GEMINI/ALTAIR images and to be 5 for the VLT/NACO ones. BACK_SIZE is also another critical parameter for the data extraction since it performs the background estimation of the image. In our case, an ideal value for that parameter spanned between 8 to 14 (see Table 2.3). A higher value will only lead to the detection of the very bright objects. The de-blending process is perfomed via DEBLEND_MINCONT and DEBLEND_THRESH parameters. They were respectively set to be 10^{-7} and 64 for a better isolation of blended sources. Extended objects and faint sources will stand a higher chance of being extracted once the parameter FILTER is activated since its role is to smooth the image before any detection. Instead of using the default file for the FILTER_NAME, we refered to the FWHM of the point sources in the field. Therefore, depending on the average of the FWHM, we either used the file *gauss_3.0_5×5.conv* or *gauss_5.0_9×9.conv*.

2.2.4 Photometry: SExtractor vs IRAF/DAOPHOT

Photometry can be performed at the same time with the object detection using SExtractor. However, we decided to use the task PHOT inside the IRAF/DAOPHOT package instead. We realised that the output photometry from SExtractor strongly depends on some critical parameters in our large galaxy dominated frame. The way its algorithm works is as follows: a new background image is built according to the value of the BACK_SIZE prompted by the user which will be used to estimate the sky when performing photometry. Regardless of a large number of detected objects associated with a small value of that parameter, cosmic rays and noise will however affect the output photometry. Therefore, we only used SExtractor for object detection and we used the IRAF/DAOPHOT package for photometry. The latter has the tasks DATAPARS and FITSKYPARS to get rid of cosmic rays and noise and the task PHOT to perform aperture photometry.

Before running the task PHOT, we first need to choose properly the size of the aperture radius and the sky annulus. They will respectively be used to estimate the amount of the flux from the source and to get a background estimation. In our case, the size of the aperture radius was set to be approximately 2 times the value of the FWHM of the point sources. If there are very close together detected sources, this will avoid the flux contamination from each other. With such a small aperture size, an aperture correction is very necessary. For a good sky sampling, because of the strongly varying background in between features of the galaxy, it is better to set the value of the inner radius just 2 or 3 pixels larger than the aperture radius. Therefore, we used 10 pixels ($\sim 0.2''$) aperture radius and a sky annulus from 12 to 15 pixels.

2.2.5 Photometry calibration

After performing the aperture photometry, we need to apply an aperture correction to the instrumental magnitude and adjust the magnitude with respect to the real magnitude zero-point.

Aperture correction

Due to the small aperture size used, not all the flux from the sources is measured. The smaller the aperture is, the higher will be the amount of flux lost. Applying an aperture correction to the instrumental magnitude will recover that loss. In this thesis, we used

the curve of growth method to estimate the aperture correction, a_c. This method is based on generating a set of instrumental magnitudes of a source while increasing the aperture radius but keeping the same value for the sky annulus. As we go far away from the centroid of the object, the curve is expected to become flat. This shape indicates that almost 100 % of the flux is considered. A bright and isolated point-like object in the field shall be chosen to draw the curve.

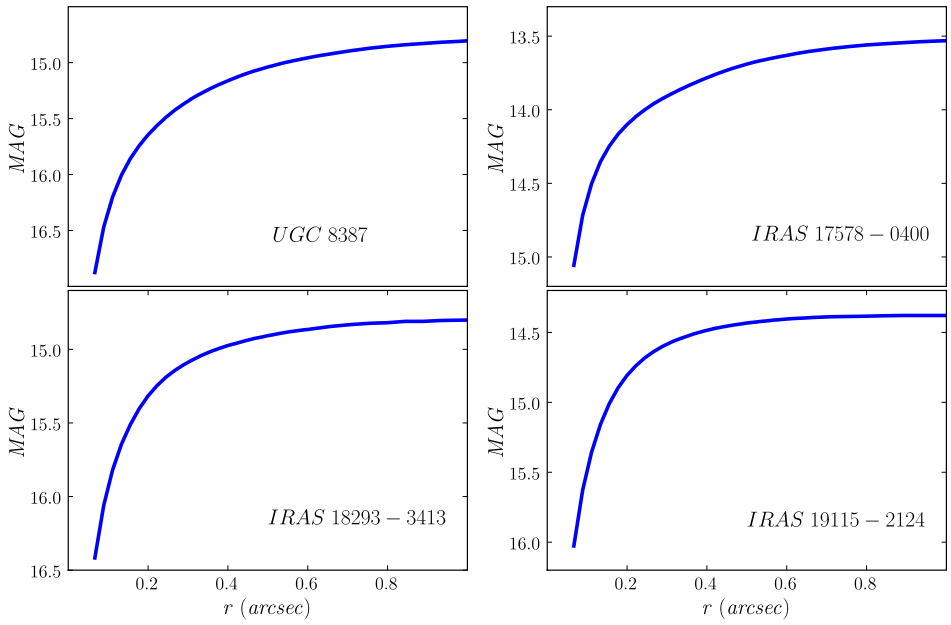

Figure 2.2: The upper panel shows the growth curves used for aperture correction for UGC 8387 and IRAS F17578-0400; the ones in the lower panel are for the VLT data. For each target, a very bright and isolated source was chosen to draw the curve.

If we look at the growth curves in Figure 2.2, with an aperture radius of r = 45 pixels ($\sim 1''$) one can get already a reasonable estimate of the apparent magnitude. In our case, we had set an aperture radius of 10 pixels ($\sim 0.2''$) for photometry. Therefore, using the curve of growth method, a_c will be the difference between the two magnitudes $MAG^{real}_{r=1}$ and $MAG^{instr}_{r=0.2}$, estimated respectively from r = $1''$ and r = $0.2''$ as shown in Eq. 2.3:

$$a_c = MAG^{real}_{r=1} - MAG^{instr}_{r=0.2} \tag{2.3}$$

For a more realistic aperture correction, we used the same sky annulus as in Section 2.2.4 while estimating the value of $MAG^{instr}_{r=0.2}$.

Since MCG +08-11-002 and CGCG 049-057 do not have any isolated sources in their field, we used the average of the derived aperture correction of the GEMINI/ALTAIR data which is 0.77 ± 0.06. The same value was also used for NGC 3690, where the few potential sources for drawing a growth curve were all located in uneven background leading to very complex curves. The value of a_c for each target are in the second column of Table 2.4.

Name	a_c	m_0
MCG +08-11-002	0.77 ± 0.06	26.66 ± 0.14
IC 694	0.83 ± 0.05	26.81 ± 0.23
NGC 3690	0.77 ± 0.06	27.23 ± 0.16
UGC 8387	1.02 ± 0.02	26.80 ± 0.22
CGCG 049-057	0.77 ± 0.06	26.46 ± 0.22
IRAS F16516-0948	0.80 ± 0.01	26.61 ± 0.20
IRAS F17138-1017	0.58 ± 0.03	26.53 ± 0.09
IRAS F17578-0400	0.64 ± 0.01	26.54 ± 0.12
IRAS 18293-3413	0.60 ± 0.02	26.95 ± 0.08
IRAS 19115-2124	0.50 ± 0.01	26.30 ± 0.13

Table 2.4: Values of the magnitude zero-point m_0 and the aperture correction a_c applied to the data for photometry calibration. The errors were estimated using the propagation of errors.

Estimating the magnitude zero-point

The magnitude zero-point, m_0, with a default value of 25, is defined as the zero-point of the photometric measurements. It is related to the magnitude system, m, of a source by the following expression:

$$m = m_0 - 2.5\ log_{10}F \tag{2.4}$$

where F is the measured flux from the source.

For this work, we only derived the zero-point for the GEMINI/ALTAIR data; those for VLT/NACO data were already available (Väisänen, private communication). Figure 2.3 summarizes the method we used for the derivation. It was based on the comparison of the magnitudes of the same source from the 2MASS catalog and the IRAF task

PHOT which was run on the input image that we want to estimate its zero-point. We needed an intermediate image since we failed to make a direct comparison between the two magnitude values.

Because the data have a small field of view (only 22″ × 22″), we first matched the magnitudes from the 2MASS K-band point-sources catalog with those measured from the NOTCAM image of the same sample. For Arp299 (IC 694/NGC 3690), no NOTCAM images were available and WHT data were used instead.

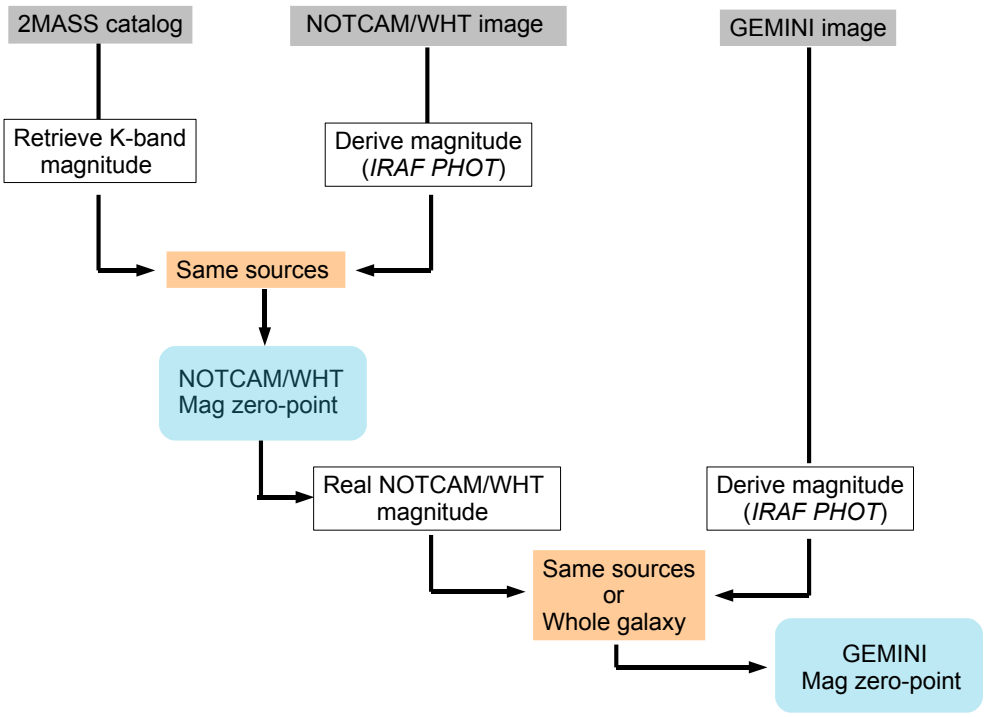

Figure 2.3: The flowchart briefly describes how the magnitude zero-point was derived in this work.

Only point-sources having a K-band magnitude uncertainties of less than 0.15 mag were used, and those sources from the intermediate data that were unsaturated and more or less isolated. A default value of m_0 was used to measure the magnitudes of these selected sources. A better estimate will arise from a higher number of the common sources. Once the zero-point of the intermediate image is evaluated, one can proceed to estimate that of the GEMINI/ALTAIR image.

The above method did not work due to the lack of common point sources for the following targets: MCG +08-11-002, CGCG 049-057, IRAS F16516-0948 and IRAS F17138-1017. In these cases, we considered the whole galaxy to estimate m_0 but just needed to make sure that the sizes for the aperture radius and the sky annulus were the same in both images. The zero-point of the GEMINI/ALTAIR data as listed in the third column of Table 2.4 were deduced from the comparison between the magnitudes from the intermediate image (either NOTCAM or WHT) using the value of m_0 which was just derived earlier with those ones from our data using the default value $m_0 = 25$.

Since all photometry was then eventually referenced to 2MASS magnitudes, our magnitude system will be the same as the 2MASS Vega-band K_S filter.

Chapter 3

Data analysis

3.1 SSC candidates selection

Deciding whether a detected source is a SSC candidate or not is quite challenging in our case because we are only working with a single filter. Firstly, we excluded the abundant detected objects seen in the edges of our images. Because the noise level is very high and there are no potential candidates in these regions, this was a better way to get rid of most of the spurious sources. After that process, we assumed that the catalog is mainly composed of real sources since we have already tuned the parameters for detection to minimize the junk sources by running the inverted version of the image (this method is described in Section 2.2.3). We then make use of a FWHM (in pixels) versus apparent magnitude (MAG) plot for the selection. This plot, shown in the upper panel of Figure 3.1, helps us to distinguish between a fuzzy object, a very bright one and a potential SSC candidate. In addition, for a robust data analysis one should take into account photometric uncertainties. Therefore, we excluded data points having errors $\sigma_{mag} > 0.25$ in their magnitudes. Finally, it is useful to make a visual inspection of the astronomical image in order to locate the selected candidates in the field and to verify whether the selected source is really a potential candidate or not. We expect that they are mainly located in the star-forming regions of the galaxy as argued by Larsen (2002).

Figure 3.1 shows plots of the FWHM *vs* MAG, σ_{mag} *vs* MAG as well as the position of the detected objects from SExtractor for IRAS 18293-3413. For that target, SSC candidates are chosen to be those having $2.5 <$ FWHM (in pixels) < 15. We are aware that the upper cutoff value $\mathrm{FWHM_{max}}$ is too far from the FWHM ~ 4.5 of a real point source, and we would potentially be including many non-point-like or blended sources.

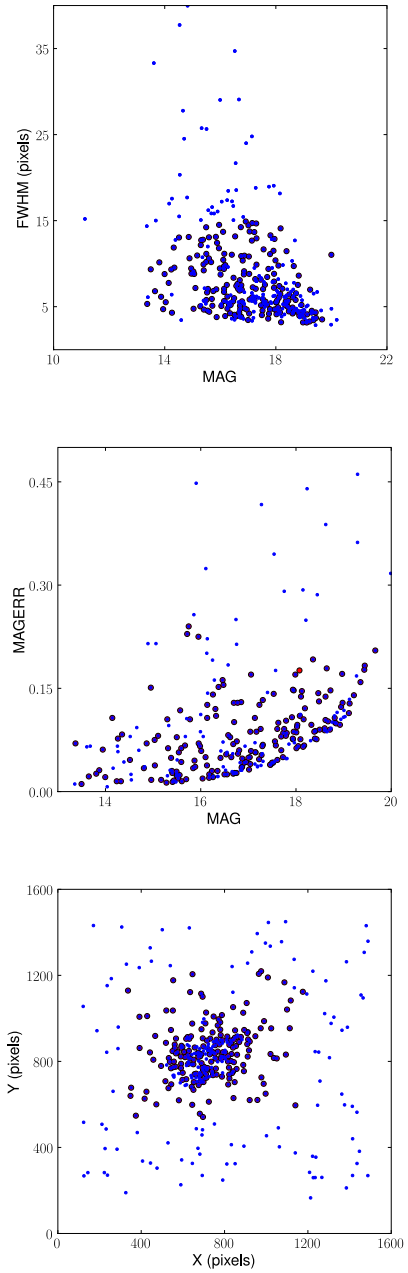

Figure 3.1: *Upper panel*: A FHWM vs MAG plot of the detected objects from SExtractor, omitting the edges of the field in IRAS 18293-3413. *Middle panel*: The uncertainty in the intrinsic magnitude plotted against the magnitude from the IRAF PHOT task. *Lower panel*: The spatial distribution of the objects in the field. The red solid points represent the SSC candidates, whereas all detected objects are the blue solid ones.

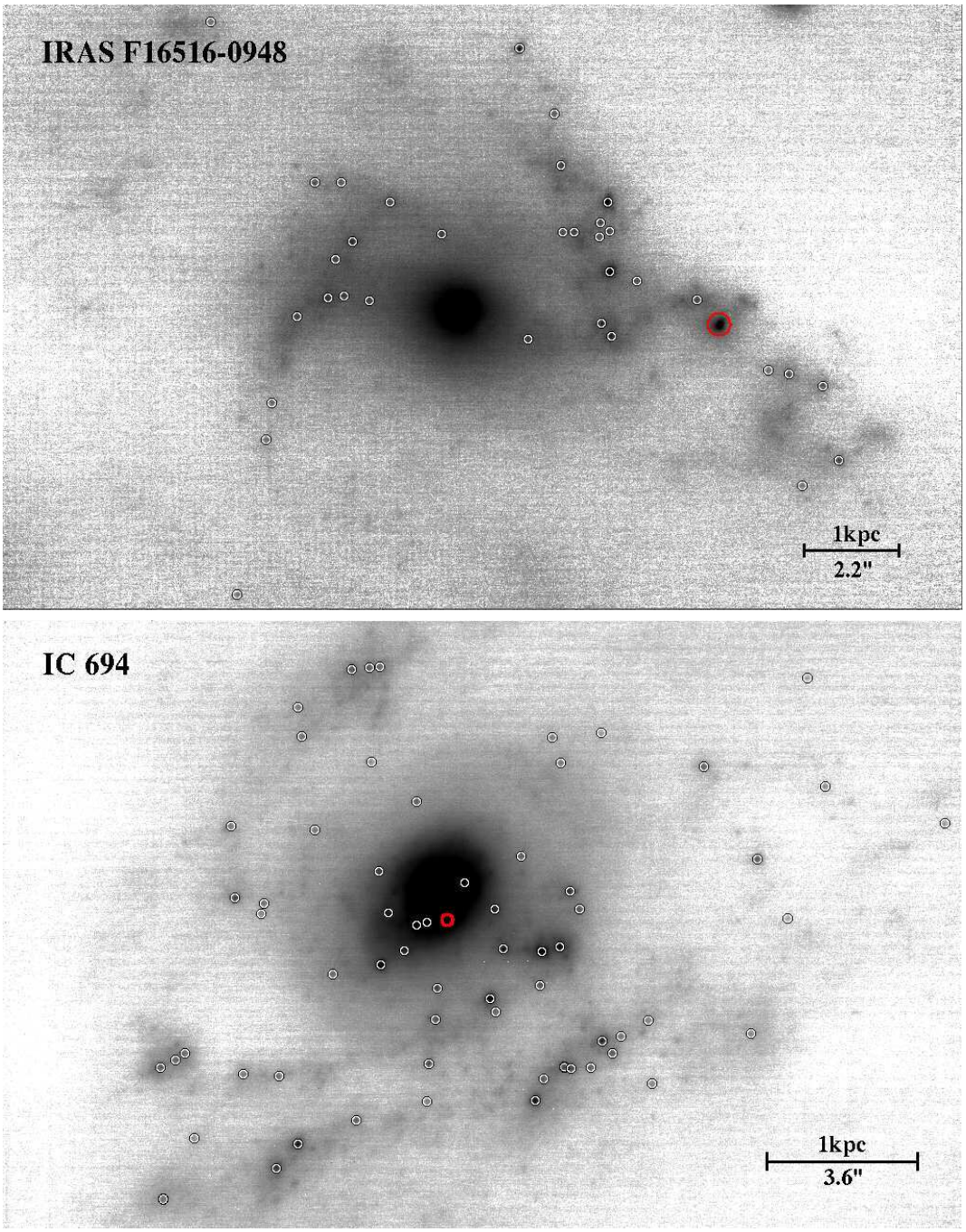
IRAS F16516-0948
1kpc
2.2"
IC 694
1kpc
3.6"

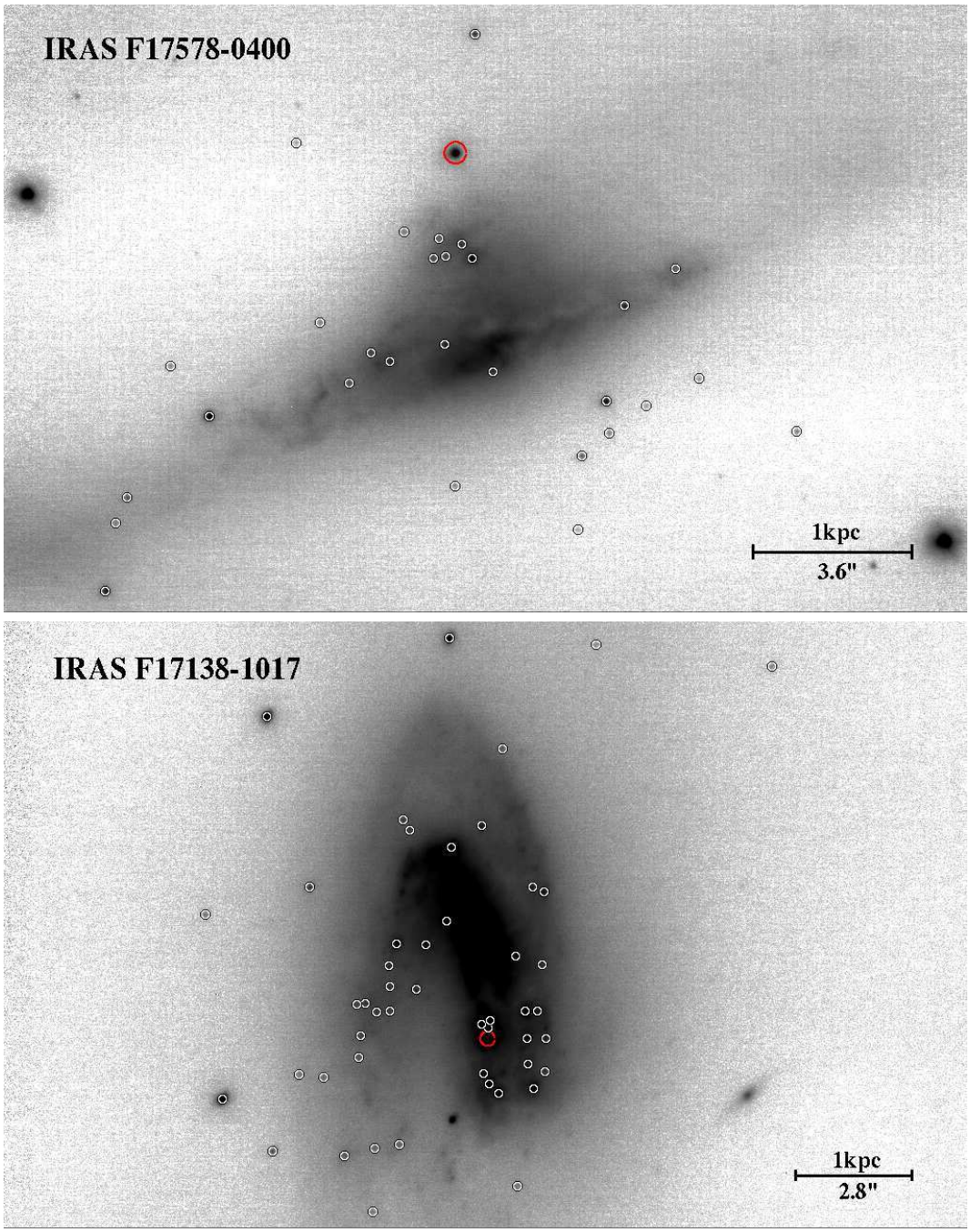
IRAS F17578-0400
1kpc
3.6"
IRAS F17138-1017
1kpc
2.8"

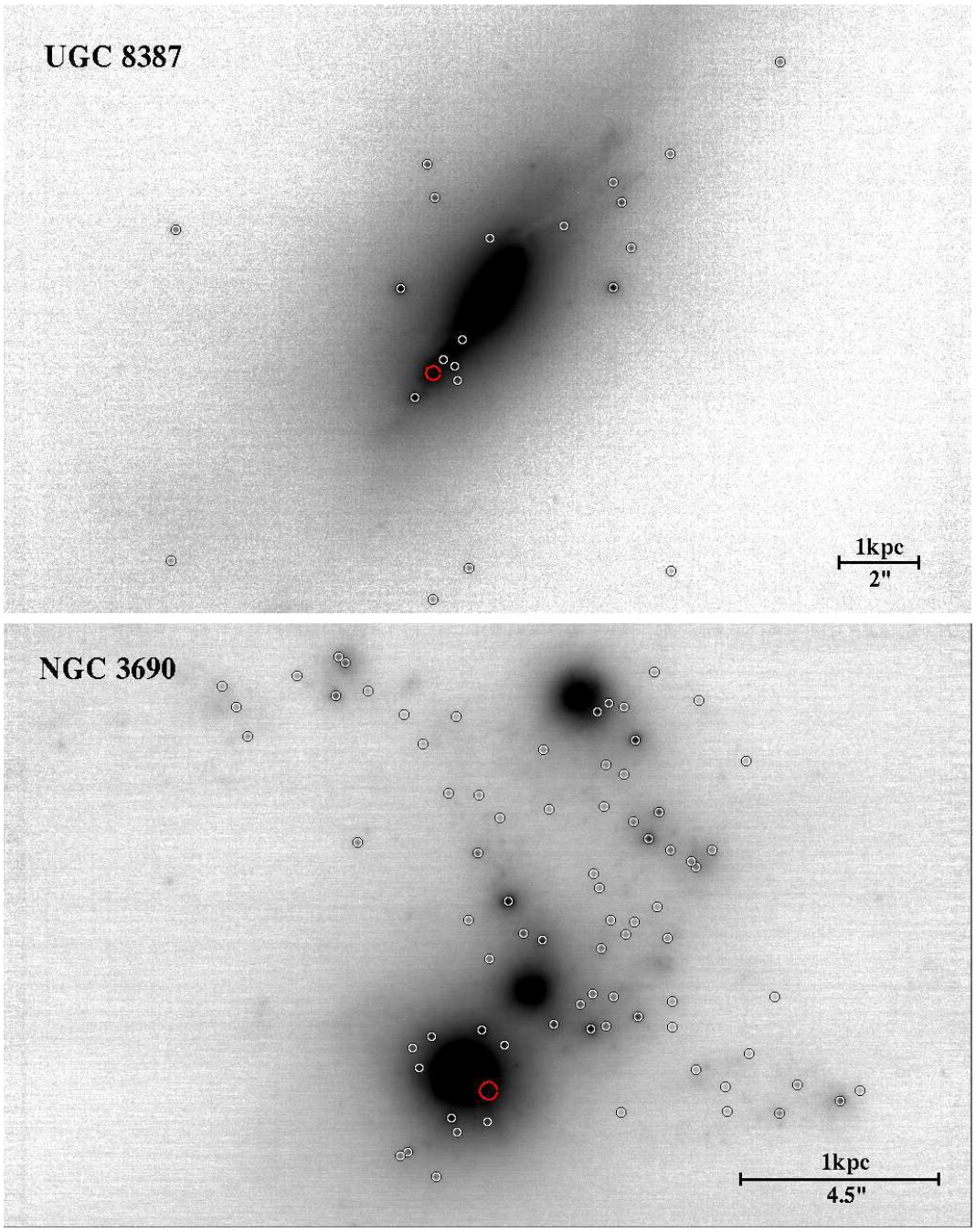
UGC 8387
1kpc
2"
NGC 3690
1kpc
4.5"

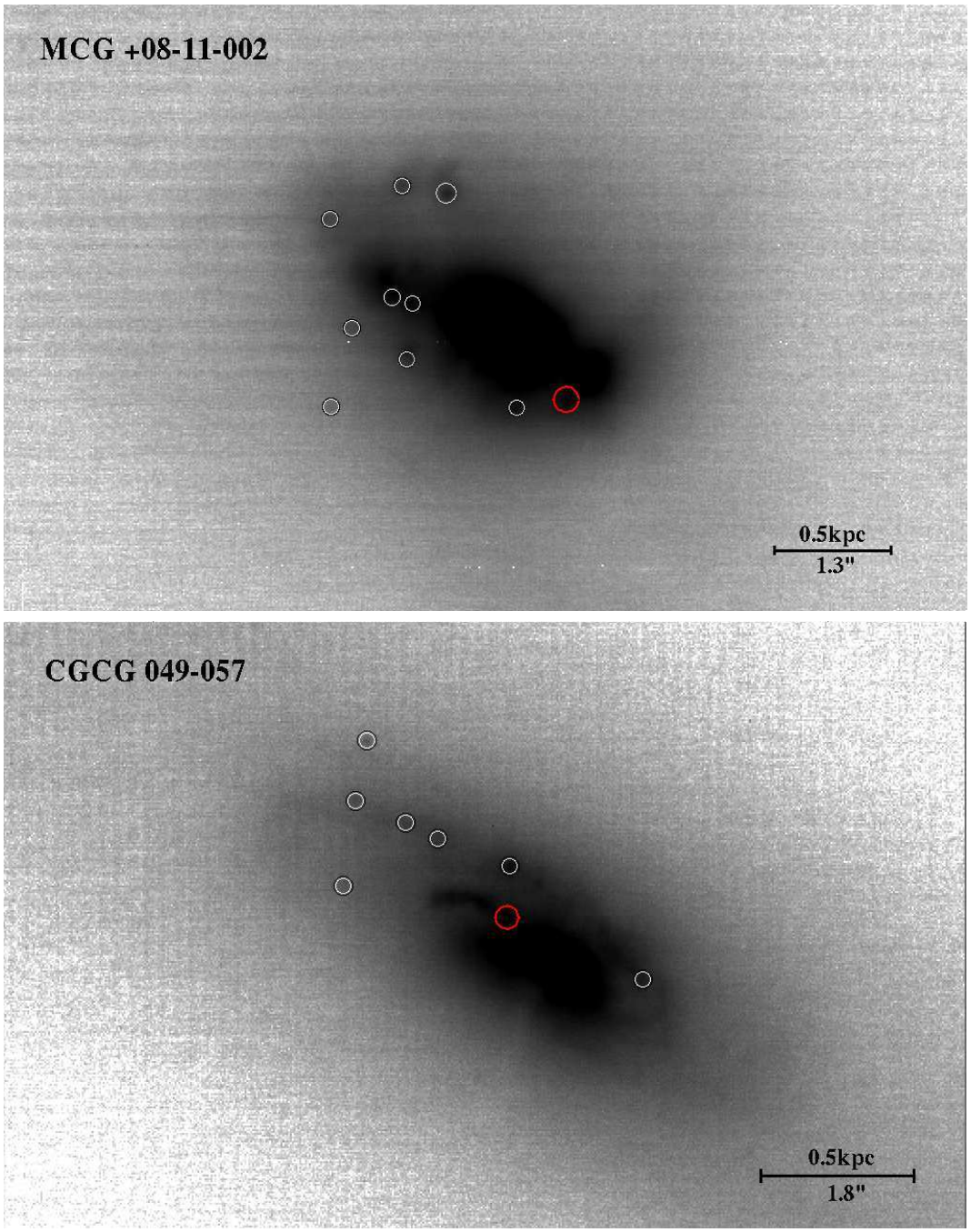
MCG +08-11-002
0.5kpc
1.3"
CGCG 049-057
0.5kpc
1.8"

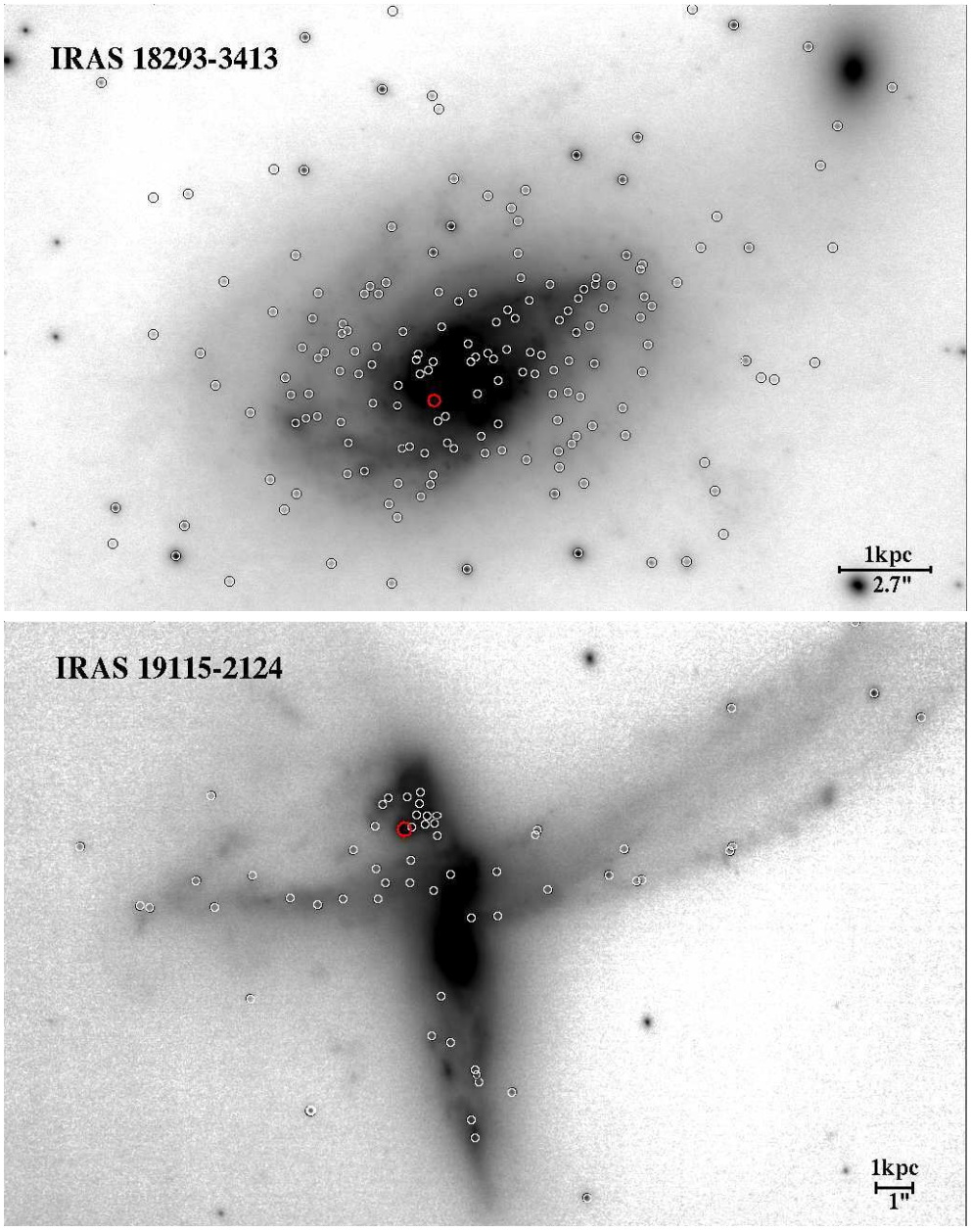

Figure 3.2: Astronomical images of our LIRGs representative sample in the K_S-band filter. The selected super star cluster candidates are marked with open circles. They are few in MCG +08-11-002 and CGCG 049-057 but are abundant in IRAS 18293-3413. Mostly located in the inner regions of the galaxy, the brightest cluster candidate is marked with a red circle.

However, in this thesis, the high cutoff value is necessary, essentially because of the uncertainty of the FWHM determination, otherwise we would lose almost half of the potential candidates as verified from visual inspection by lowering it. We realized that the FWHM output by SExtractor strongly depends on the setting of the BACK_SIZE, especially with the relatively small values of the parameter as required in our fields (see Table 2.3). Estimating the FWHM is quite difficult since most of the sources are on top of diffuse emission and the background level is strongly varying all over the frame. Finally, we checked the final results of the derived LF in the case of using a more stringent FWHM cutoff and we found that there is no significant change in the values of α, which is the LF power-law index, in spite of a lower cutoff.

The open circles in Figure 3.2 illustrate the spatial distribution of the SSC candidates in each target. Appendix A show a zoomed in rescaled version of each target frame. We noticed that detected objects are generally elongated for IRAS F16516-0948, possibly because of an unsucessful AO-correction or a misalignment of its individual frames. Under the chosen selection criteria, their numbers are listed in the first column of Table 3.1.

3.2 The SSC K-band LF

3.2.1 Completeness test

During object detection, faint objects are likely to be missed leading to an incomplete sample. For a more accurate data analysis, we first need to determine the photometric completeness limit of each sample then correct the data for that bias. This step is useful in order to get a more realistic result, otherwise one may derive a LF with a spurious bend in the faint end or with a shallower slope (Anders et al. 2007). For this thesis, we therefore ran our own Monte Carlo (MC) completeness simulations through the science images. In what follows, we will first highlight the creation of an artificial star which is necessary for the simulation and later explain how it works based on the algorithm of the script. We should note that we assumed that the completeness fractions output by the simulation would be similar to the ones which will be derived from the simulation of an artificial star cluster.

Creating the artificial star

Using IRAF/DAOPHOT package, we created a point-spread function (PSF) model for each target field. For the task PSTSELECT, bright and non-saturated isolated objects

were selected, as many as possible. While creating the model with the task PSF, we used the same FWHM as that of a potential SSC candidate and a total PSF radius of 45 pixels ($\sim 1''$) which we hope will recover almost all the energy from the source as shown in the curve of growth method for aperture correction (see Section 2.2.5). Figure 3.3 shows the frames of some created PSF stars. We considered the best PSF model among the others for MCG + 08-11-002 and CGCG 049-057 due to the non-existence of isolated stars in the field. Once the artificial star is created, it will be scaled and then used to run the MC completeness simulation.

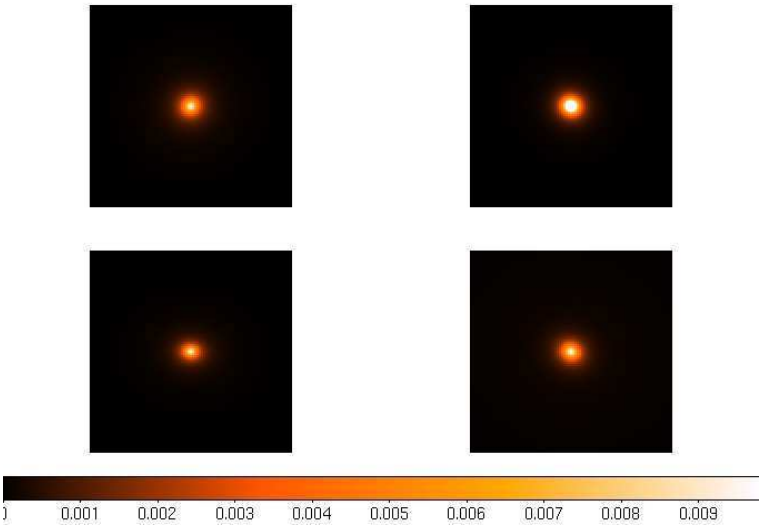

Figure 3.3: Some PSF models output from IRAF/DAOPHOT package. With a field of of $\sim 1'' \times 1''$, they will be randomly implemented in their respective science images for a completeness test.

Scaling the star

Because we will be running the simulation over a range of magnitudes, it is useful to first scale the PSF model. This means that we divide each count of the frame by the total number of pixels forming the model so that the total flux F of the scaled PSF will be equal to 1. For any given magnitude, m, we can use the formula:

$$F = 10^{-0.4(m-m_0)} \tag{3.1}$$

to derive the corresponding flux since we have already determined the value of the magnitude zero-point, m_0, in Section 2.2.5.

Building the MC completeness simulation

The main idea of the simulation is to record how many of the input objects, added randomly in the science images, are detected by SExtractor at a given magnitude range. A simple algorithm of the script is illustrated in Appendix B and the details are given below:

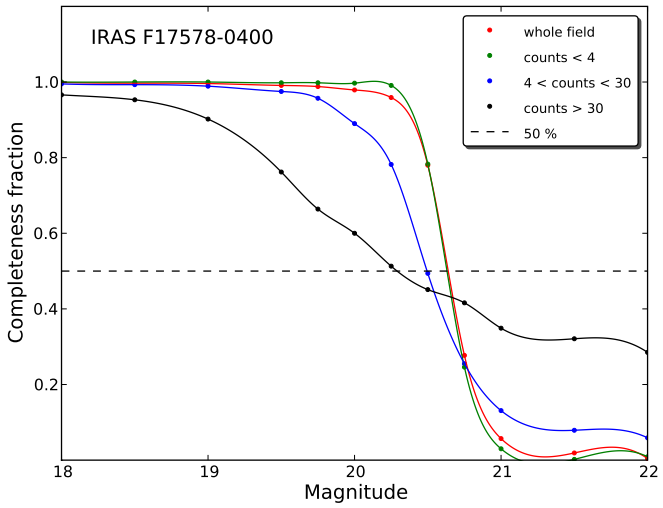

Figure 3.4: The results of Monte Carlo completeness simulation within different regions of IRAS 17578-0400. Each curve corresponds to the interpolation of data points output by the simulation for a given background level. The horizontal dashed line represents the 50 % completeness limit. From the figure, we can see that a superposition of many background levels would lead to a shallower completeness curve which is the case for the blue and the black curves. They respectively correspond to the middle and the inner regions of the frame.

(1) We first derived the corresponding flux of the chosen magnitude using Eq. 3.1. We then get the frame of the artificial star associated to that flux using the scaled PSF model. In our case, the simulation ran from 18 to 22 magnitudes in steps of 0.5 mag.
(2) For better statistics, we generated 1,000 random positions of the centroids of the stars. To avoid systematic errors, we used a new subset of random positions for each magnitude.
(3) Once the artificial star has the desired magnitude value and its centroid has specific coordinates, we implemented the star in the science image by adding the counts from the scaled PSF frame with those of the field within the specified location.

(4) Each time we added the star one by one, not to change the characteristics of the source density in the frames, we ran SExtractor on the science image using the same input parameters when doing object detection (See Section 2.2.3). We read through the output catalog, to check whether the star was detected or not.

After looping the same process over the chosen magnitude range, one can get a plot of the completeness fraction of the detected objects with respect to their magnitudes. In Figure 3.4, it is represented by the red line and the horizontal dashed line shows the 50 % completeness level. However, for a robust completeness test, we ran the simulation in different regions of the field. To determine whether a random position corresponds to a specific region in the field, we estimated the average background level from its surrounding 5 by 5 pixel area and then checked if that value falls in the condition imposed regarding the counts of that region. As an example, a random position having an average background less than 4 counts is amongst the "outer regions" of the field for IRAS F17578-0400 (the green line in Figure 3.4). Between 4 and 30 counts, it is located in the "extended regions" of the galaxy (the blue line) and finally, for a value greater than 30, it will correspond to the "inner regions" (the black line). These conditions vary from one target to another since they do not have the same background level.

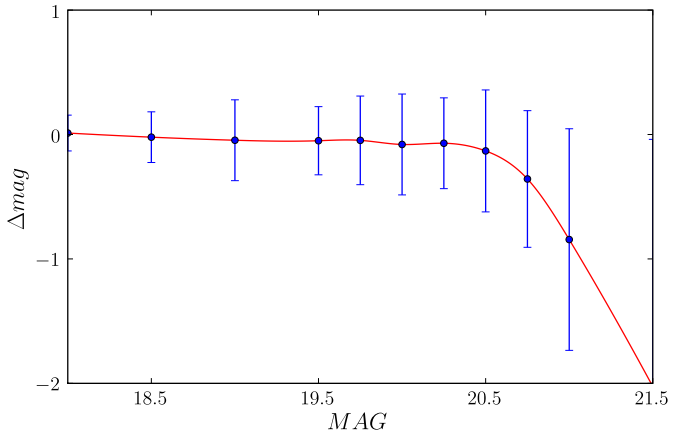

Figure 3.5: This plot indicates the accuracy of our photometry compared to the magnitude MAG of the artificial star for IRAS F17578-0400. Δmag is the difference between MAG and the photometry output by the task PHOT if the star was detected. The figure shows that our output photometry is reliable until $\sim$ 20.5 mag.

As can be seen in Figure 3.2, the SSC candidates are generally located in the starburst regions of the galaxy. Moreover, using a short python script, we found that approximately 70 % of the SSC candidates are actually located in the "extended regions" of the galaxy. Therefore, we decided to use the output simulation of the middle regions, corresponding to the blue line in Figure 3.4, for the incompleteness correction. The results of the simulation of each target are shown in Appendix C and Table 3.1 lists the magnitude values of the 50 % completeness limit in each target.

In addition, if the star was detected, we performed photometry using exactly the same parameters as in Section 2.2.4. This is aimed to verify the consistency of our photometry compared to the known magnitude of the artificial star. One can see from Figure 3.5 that our output photometry is reliable until $\sim$ 20.5 mag for IRAS F17578-0400 since $|\Delta\text{mag}| < 0.15$ where the completeness level is approximately 50 %.

Name	Nb SSC	Completeness limit	
	($\sigma \leqslant 0.25$)	Apparent mag	Absolute mag
MCG +08-11-002	10	19.5	-14.9
IC 694	66	19.5	-14.3
NGC 3690	80	19.4	-13.9
UGC 8387	23	20.1	-14.9
CGCG 049-057	8	19.9	-13.9
IRAS F16516-0948	35	20.2	-14.6
IRAS F17138-1017	55	20.7	-13.6
IRAS F17578-0400	34	20.5	-13.3
IRAS 18293-3413	176	20.1	-14.2
IRAS 19115-2124	63	20.5	-16.1

Table 3.1: After imposing our selection criteria, we got the number of SSC candidates for each target. The distribution of these candidates are shown in Figure 3.2 and Appendix A. The 50 % completeness level is given in both apparent and absolute magnitudes. The lower value of the absolute magnitude for IRAS 19115-2124 is because of its distance $D = 206$ Mpc which is very far away compared with the other targets.

3.2.2 Constructing the luminosity function

Once the SSC candidates have been selected for each target, one can construct a binned LF and then later fit a function to its shape. In order to convert the photometry in terms of absolute magnitude M_K, we used the luminosity distance D of the sample retrieved from the NASA/IPAC Extragalactic Database (NED) as listed in Table 2.1 and the

following expression:

$$m_K \; - \; M_K = \; 5 \; log_{10} D \; - \; 5 \tag{3.2}$$

Binning

Maíz Apellániz & Úbeda (2005) indicated that the shape of the true LF may be affected by sample binning. To check for consistency, we decided to construct two LFs from the data points of each target using two different methods. A large discrepancy between the two fitting parameters of the derived LFs would probably indicate the effect of the sample binning.

The first method was to choose a constant bin size and then count the number of the objects falling in each magnitude bin. The second way to derive the LF was to use a variable bin size by assigning the same number of objects to each bin, then estimate Δmag to get the number per magnitude bin. The more the target had SSC candidates, the smaller was the value of the bin size that was used in the first method. While dealing with the second method, it would be convenient to choose a reasonable amount of objects placed in each bin for a more accurate result, approximately of the order of 8 SSC candidates per bin.

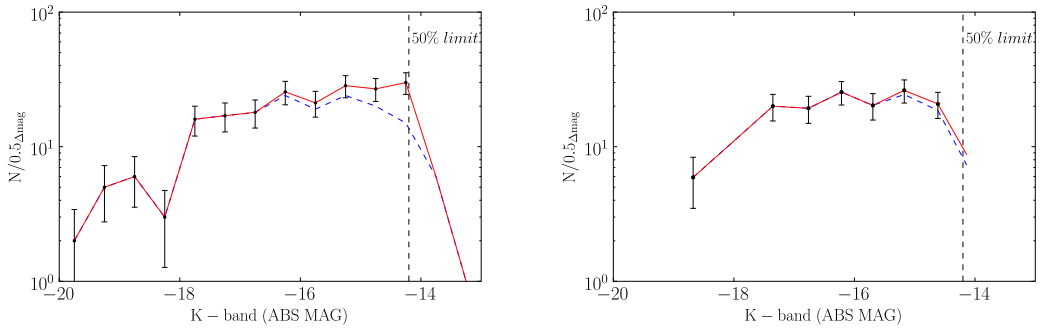

Figure 3.6: The two SSC LFs of IRAS 18293-3413 derived with two different methods. The solid line is the incompleteness corrected LF while the dashed line is the original one. The vertical line indicates the 50% completeness limit. The left panel is the binned LF when the data were distributed into the same bin size of 0.5 mag and the right panel is the one when the magnitude bin size was variable but had the same number of objects, which is 23 in this case.

Fitting a function to the LFs

From visual inspection, the number of the clusters generally rises as we move towards fainter magnitudes. Doing a linear least-squares fit to the data in log-log space will probably be the most appropriate approximation of the shape of the LF. For a better precision of the fit, we should weigh the data points using their respective poisson-noise uncertainties $\sqrt[2]{N}$.

When overplotting the weighted linear fitting with the LFs, as shown in Figure 3.7, 3.8 and 3.9, one can really see that the shape of the LF follows a power-law function of the form:

$$N(L)dL \sim L^{-\alpha}dL \tag{3.3}$$

In a log-log plot, the linear fitting is expressed as follows:

$$\log N(M_K) \; = \; AM_K \; + \; B \tag{3.4}$$

According to Elmegreen & Efremov (1997), the relation between α and the linear slope A can be derived as follows:

Since M_K is related to L by:

$$M_K \sim -2.5 \log L \tag{3.5}$$

Therefore,

$$N(L)dL \; = \; n(L)L \; d\log L \sim -n(L)L \; dM_K/2.5 \tag{3.6}$$

Converting the luminosity into magnitude in the left hand side of Eq. 3.6:

$$N(L)dL \; = \; n(M_K)dM_K \tag{3.7}$$

Equating Eq. (3.6) and (3.7), one can write:

$$n(M_K) = \; n(L)L/2.5 \tag{3.8}$$

Using Eq. (3.3) and by taking the logarithms:

$$\log \, n(M_K) \; = \; (1 \; - \; \alpha) \log \, L \; + C^{te} \tag{3.9}$$

Using Eq. (3.5), one can finally write:

$$\log \, n(M_K) \; = \; 0.4(\alpha \; - \; 1)M_K \; + C^{te} \tag{3.10}$$

where C^{te} corresponds to the intercept of the linear fit in Eq. 3.4 and

$$A = 0.4(\alpha - 1) \tag{3.11}$$

corresponds to the slope.

Therefore, the power-law index of the distribution is expressed as

$$\alpha = 2.5A + 1 \tag{3.12}$$

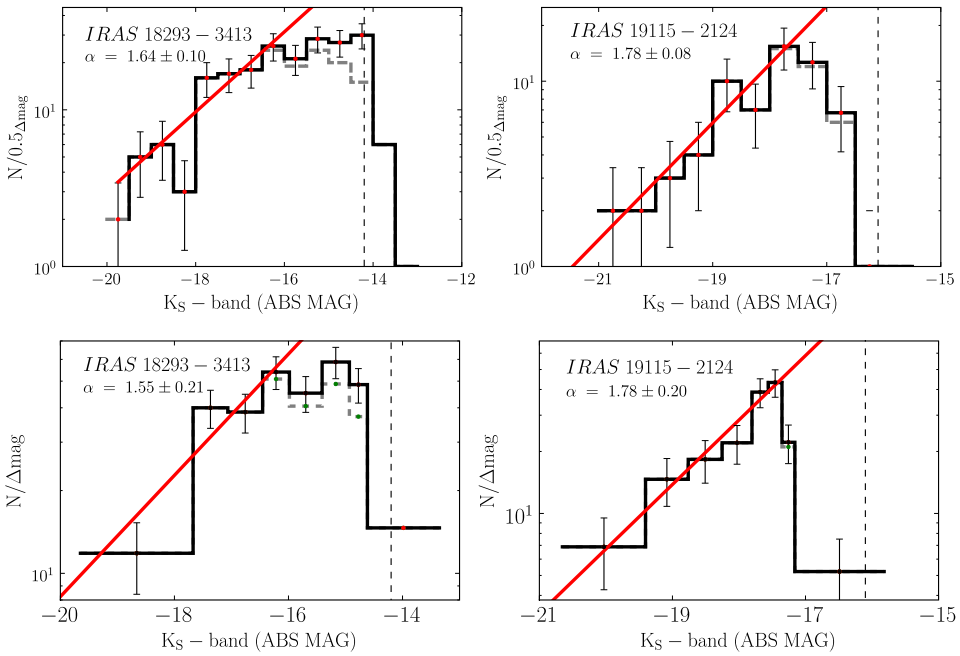

Figure 3.7: *Upper panel:* VLT/NACO SSC candidate K_S-band LFs using a constant bin size. *Lower panel:* VLT/NACO SSC candidate K_S-band LFs using a variable bin size with equal number. The black solid line is the incompleteness corrected LF while the dashed line is the original one. The red solid line is the weighted linear fit of the data points and the vertical line marks the 50 % completeness limit. While we were able to reach up to $\sim$ -14 mag in IRAS 18293-3413, the distance of IRAS 19115-2124 only allowed us to construct a LF until $\sim$ -16 mag. LF in the left panels probably show evidence for a turnover at fainter magnitudes since the bend starts at about two magnitudes above the completeness limit.

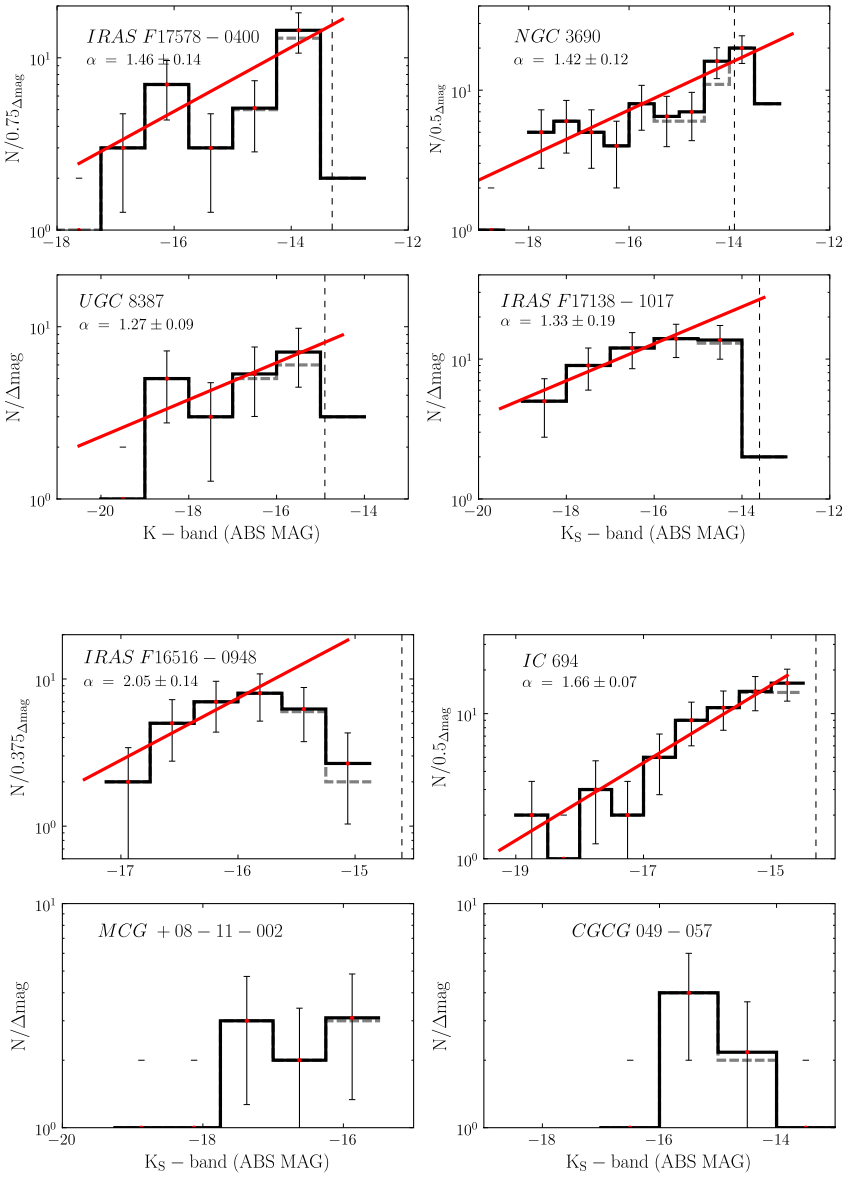

Figure 3.8: GEMINI/ALTAIR SSC candidates K_S-band LFs using a constant bin size. The black solid line is the incompleteness corrected LF while the dashed line is the original one. The red solid line is the weighted linear fit of the data points and the vertical line marks the 50 % completeness level. Due to the very small number of super star cluster candidates in MCG +08-11-002 and CGCG 049-057, we preferred to not apply a fitting to the LF. Since the targets forming the sample do not have the same number of SSC candidates, their bin sizes are not the same, hence the y-axis label varies from one target to another one.

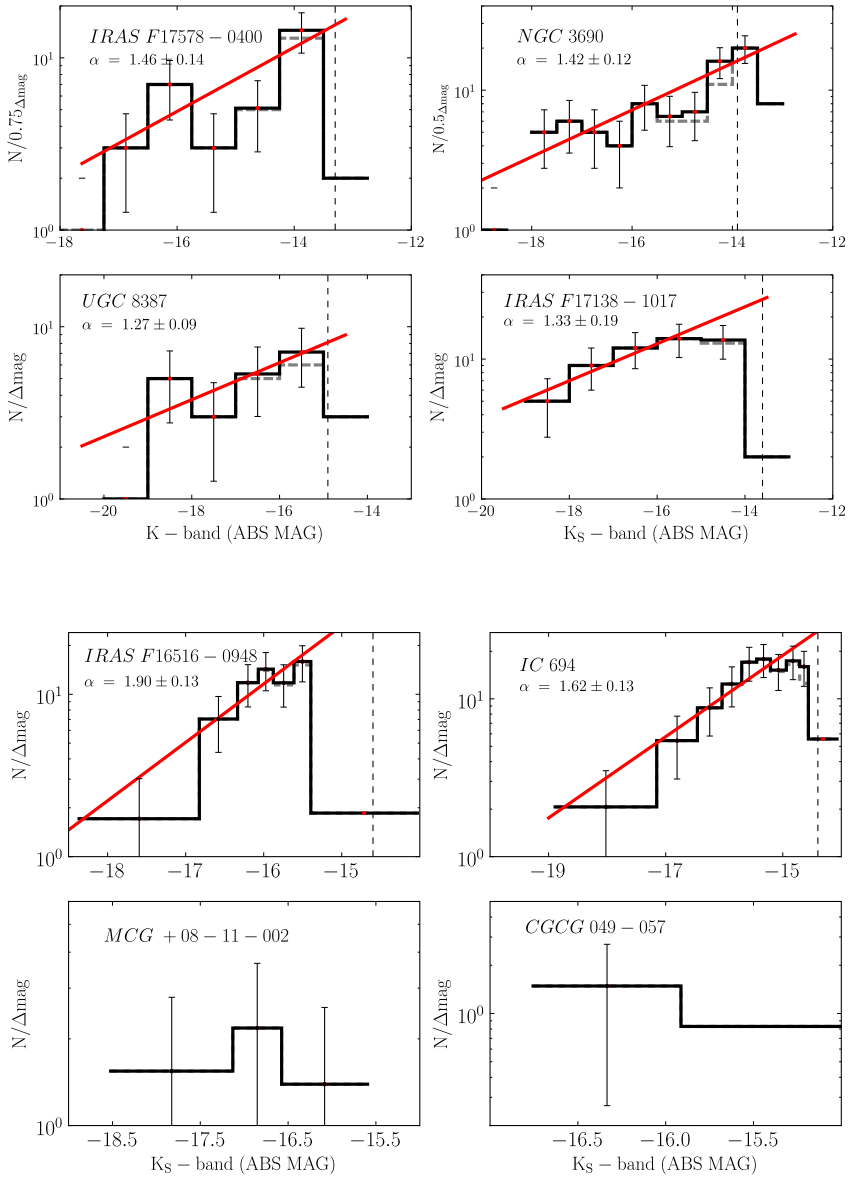

Figure 3.9: GEMINI/ALTAIR SSC candidates K_S-band LFs using a variable bin size with equal number. The black solid line is the incompleteness corrected LF while the dashed line is the original one. The red solid line is the weighted linear fit of the data points and the vertical line marks the 50 % completeness level.

Considering Eq. 3.12, we find the values of α as listed in Table 3.2 for each LF using the two different methods. α_1 is the slope of the LF for a constant bin size with an average of $\bar{\alpha_1} \sim 1.57 \pm 0.24$, whereas α_2 is the one derived from a variable bin size with an average of $\bar{\alpha_2} \sim 1.58 \pm 0.18$. Although the values of $\bar{\alpha_1}$ and $\bar{\alpha_2}$ are slightly different, their errors show that the slopes derived from the two different ways of binning are still statistically consistent. Maíz Apellániz & Úbeda (2005) argued that the difference can be as large as 0.3 for small datasets due to a sample binning effect. The resulting LF slopes will be discussed in Section 4.2 and 4.3.

Name	α_1	α_2
IRAS F16516-0948	2.05±0.14	1.90±0.13
IRAS F17578-0400	1.46±0.14	1.51±0.15
IRAS F17138-1017	1.33±0.19	1.50±0.15
UGC 8387	1.27±0.09	1.25±0.10
IRAS 18293-3413	1.64±0.10	1.55±0.21
IRAS 19115-2124	1.78±0.08	1.78±0.20
IC 694	1.66±0.07	1.62±0.13
NGC 3690	1.42±0.12	1.57±0.13

Table 3.2: After a weighted linear fitting of the LF, we got the power-law indices using the relation in Eq. 3.12. α_1 and α_2 are respectively the indices derived from binning with the same bin width and binning with the same number in each bin. A discrepancy between the two slopes is most probably due to a sample binning effect. Nevertheless, the mean values of α_1 and α_2 are approximately equal to $\bar{\alpha_1} \sim 1.57 \pm 0.24$ and $\bar{\alpha_2} \sim 1.58 \pm 0.18$.

Goodness of the fit

To check whether a single power-law is really a good approximation of the LF, we estimated the reduced chi-square statistic χ^2_{red} in each case. Knowing the value of chi square χ^2, the measurement of the goodness of the fit, which is χ^2_{red} in our case, is derived as follows:

$$\chi^2_{red} = \frac{\chi^2}{N - p - 1} \tag{3.13}$$

where ν = N - p - 1 is the degree of freedom. N is the number of data points considered for the linear fit and p = 2 is the number of fitting parameters (the slope and the intercept).

A value of χ^2_{red} close to 1 indicates that a single-power law function is a good fit to

the shape of the LF. However, a value approaching 0 or much larger than 1 mean that the adopted function is not the best approximation of the data points.

Table 3.3 tabulates the goodness of a linear fit to the data points. $\chi^2_{red,1}$ and $\chi^2_{red,2}$ are respectively the measurement of the goodness of the fit from a constant and a variable bin size while deriving the LF. From the values of χ^2_{red} in both cases of binning, one can say that a single power-law is generally reasonable to fit the SSC candidate LFs. However, we should note that in some cases, such as IRAS F17138-1017 and IRAS 18293-3413, the values of χ^2_{red} are respectively approaching 0 and are above 1. In fact, a double-power law could be a better fit in some cases with a break either in the bright or faint end.

Nethertheless, only single power-laws were considered as a first approximation for simplicity in this work which deals with new kind of data.

Name	$\chi^2_{red,1}$	$\chi^2_{red,2}$
IRAS F16516-0948	0.63	0.67
IRAS F17578-0400	1.63	0.90
IRAS F17138-1017	0.40	0.06
UGC 8387	1.06	0.67
IRAS 18293-3413	1.27	2.03
IRAS 19115-2124	0.64	0.30
IC 694	0.41	0.68
NGC 3690	0.79	0.63

Table 3.3: $\chi^2_{red,1}$ and $\chi^2_{red,2}$ are respectively the reduced Chi Square values of the linear fitting from binning with the same bin width and binning with the same number in each bin.

3.2.3 Foreground contamination

If the target field lies at a low galactic latitude ($b < |20°|$), foreground stars from our own Galaxy may affect the analysis. Looking at the galactic coordinates of our targets, as listed in Table 2.1, our photometry might be affected by such contamination for some cases. Since the aim of the thesis is to construct the LF of the star clusters as accurately as possible, we need to check whether this effect is really critical for our results or not.

In this work, the following steps were carried out for the decontamination process: LFs

of the detected objects in the "inner" and the "outer regions" of the galaxy frames were first derived. Obviously, the objects in the "inner regions" close to the galaxy are most likely to be the SSC candidates as shown in Section 3.1, whereas those in the "outer regions" are most likely to be foreground stars. The very brightest obvious stars as well as the galaxy nucleus were not considered. Once the LFs were constructed, the respective completeness fractions of both regions were applied to the data for correction. After estimating the areas, *Inner Area* and *Outer Area*, of the two regions of the field, we then derived the surface number density of the sources for each magnitude bin. We used Eq. 3.14 to generate the data for a foreground corrected LF. Finally, we rescaled the data by multiplying it with the *Inner Area*.

$$N_{corrected} = \left(\frac{N_{IN}}{Inner\ Area} - \frac{N_{OUT}}{Outer\ Area}\right) \times Inner\ Area \tag{3.14}$$

A considerable variation of the index α of the foreground corrected LF would indicate the importance of the contamination, assuming that the incompleteness correction was perfect. If the influence is small, the value of α will almost be the same before and after the decontamination process.

GEMINI/ALTAIR data

From a visual inspection, it is difficult to judge whether a detected object, even a bright one, is a foreground star or not because of the small field of the GEMINI/ALTAIR data. Nevertheless, we tried to quantify the effect of the contamination in the data using one of the targets which simultaneously presents a large number of SSC candidates and has many sources suspected to be foreground stars in the outer field. Therefore, we chose IRAS F17578-0400 since its data fit in the above criteria. Figure 3.10 shows the LF being corrected for the contamination and Table 3.4 shows the values of α before and after the correction.

VLT/NACO data

VLT/NACO images have a slightly larger field compared to the GEMINI/ALTAIR ones and they are at low galactic latitudes. One would expect better statistics of the foreground stars. Therefore, it would be relevant to check on both images (IRAS 19115-2124, IRAS 18293-3413) the effect of the contamination. Figure 3.11 shows the foreground corrected LF of both targets and the variation in α are also seen in Table 3.4.

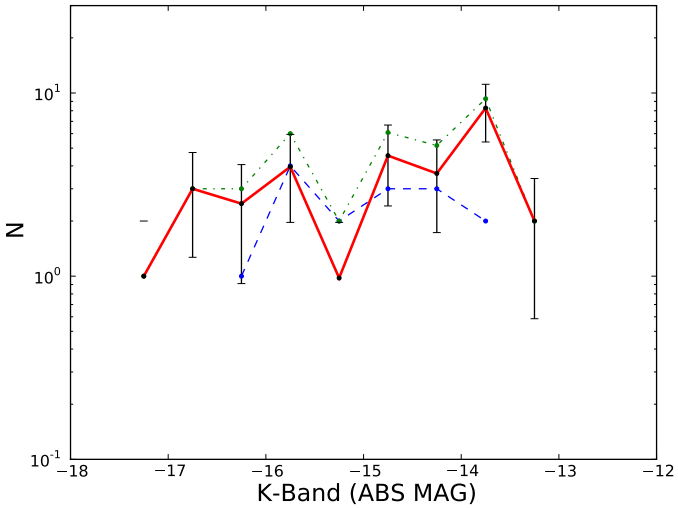

Figure 3.10: The red solid line represents the shape of the SSC LF of IRAS 17578-0400 after being corrected for foreground contamination while subtracting the surface number density of the detected objects located in the "outer regions" of the field (green dot-dashed line) from the ones in the "inner regions" (blue dashed line).

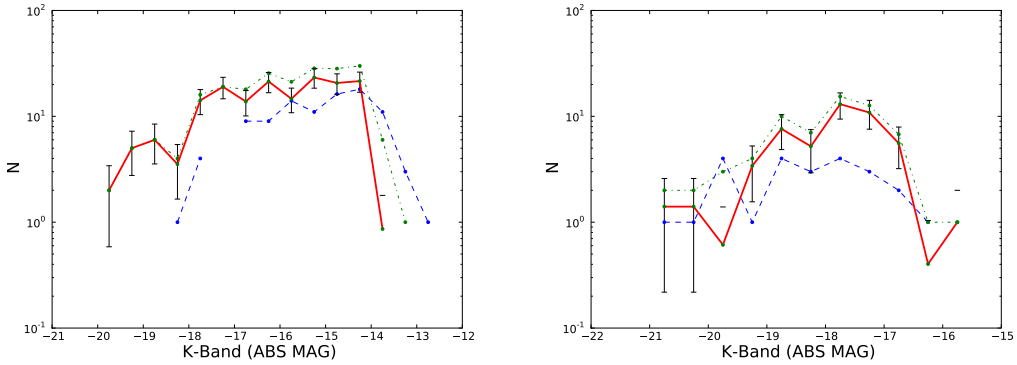

Figure 3.11: The figure shows how the foregound stars affect the shape of the LF for the VLT/NACO data. The left panel shows the effect of the contamination in IRAS 18293-3413 and the right panel to that of IRAS 19115-2124. The red solid line represents the shape of the SSC LF after being corrected for foreground contamination while subtracting the surface number density of the detected objects located in the "outer regions" of the field (green dot-dashed line) from the ones in the "inner regions" (blue dashed line).

The results from both GEMINI/ALTAIR and VLT/NACO data show that the contamination tend to affect more the data at the faint end of the LF not those at the bright end. However, by comparing the values of α before and after the decontamination

process, as seen in Table 3.4, the effect to the data is generally insignificant, especially for the GEMINI/ALTAIR case. So we will use the LFs only corrected for incompleteness for further analysis.

Name	α_1	α_2
IRAS F17578-0400	1.467±0.14	1.472±0.14
IRAS 18293-3413	1.64±0.10	1.57±0.11
IRAS 19115-2124	1.78±0.08	1.88±0.09

Table 3.4: α_1 and α_2 are respectively the values of the power-law index before and after applying a foreground correction to the data. They are almost the same for the case of IRAS F17578-0400 and are slightly varying in the order of ~ 0.1 for the VLT/NACO images.

3.3 Star formation rate estimate of the sample

As already mentioned in Section 1.3, luminous infrared galaxies are a good laboratory to study star formation rate (SFR) since they are often associated with violent star formation activity. Under some assumptions, Kennicutt (1998a) established an empirical relation between the galaxy SFR and its infrared luminosity L_{ir}, emitting in the mid- and far-IR (8 - 1000μm). This relation is expressed as follows:

$$\frac{SFR}{M_\odot\ yr^{-1}} \ = \ 4.5 \times 10^{-44}\ (\frac{L_{ir}}{ergs}) \tag{3.15}$$

and can also be written as:

$$SFR \ = \ 1.7 \times 10^{-10}\ L_{ir}\ [\mathrm{M_\odot\ yr^{-1}}] \tag{3.16}$$

Therefore, knowing the infrared luminosity L_{ir}, then using one of the above equations (Eq. 3.15 or 3.16), one can estimate the galaxy SFR. In our case, we retrieved the values of L_{ir} (see Table 2.1) from the *IRAS Revised Bright Galaxy Sample (RBGS)* which was published by Sanders et al. (2003). They used Eq. 1.1 and Eq. 1.2 to calculate L_{ir}, once they had derived the values of the fluxes emitted by the galaxy in all the IRAS bands and its luminosity distance. However, one should bear in mind that if the galaxy hosts an active galactic nucleus, L_{ir} will be the emission from both the AGN and the active star-forming regions. And if the AGN activity dominates the source of energy, the Kennicutt relation will no longer hold. The present sample consists of starburst-dominated galaxies.

Note, however, that IC 694 and NGC 3690 together form Arp 299 which is not resolved as two galaxies by IRAS survey. Consequently, we first need to estimate the individual L_{ir} of both galaxies before deriving their SFR using the Kennicutt relation. To derive L_{ir} of IC 694 and NGC 3690, we retrieved the archival data of Arp 299 in the mid and FIR from the Spitzer website[1]. Unfortunately, the data in the 8 μm was the only useful one since those from longer wavelengths were saturated. Nevertheless, it is more realistic to estimate the IR luminosity of each galaxy using that single waveband rather than using the one listed in the *IRAS RBGS*. Moreover, an empirical relation from the observations done with the AKARI infrared all-sky survey suggests that a total infrared luminosity estimated with the 8 μm Spitzer band is still somewhat reliable, since the error would be of an order of 2 or less (Goto et al. 2010).

Therefore, after correcting for bad pixels in the 8 μm image, and estimating the total flux of each galaxy component ($F_{IC\ 694}$ and $F_{NGC\ 3690}$), we took the ratio $F_{IC\ 694}/F_{NGC\ 3690}$ to get an approximate estimate of the infrared luminosity of each individual galaxy of the Arp 299 system. In both cases, the aperture radius was chosen such that most of the flux from the target will be enclosed within the radius and that the light from its neighbour will not be included. The sky annulus was estimated very far away outside the merging system, in a region free of sources.

From this method, we found that $F_{IC\ 694}/F_{NGC\ 3690} \sim 0.6$, which means that approximately 60 % of the infrared luminosity comes from IC 694 and the rest from NGC 3690. These results are in good agreement with a previous work on Arp 299 by Joy et al. (1989).

The star formation rates SFR of the whole sample are listed in the third column of Table 3.5. In their work, Mattila et al. (2007) and Väisänen et al. (2008) have respectively derived the value of SFR for IRAS 18293-3413 and IRAS 19115-2124 by fitting the full spectral energy distribution of the galaxies. While we are aware that they adopted a more accurate way to derive SFR, for consistency we rather used the Kennicutt relation for the whole sample here.

[1] See www.spitzer.caltech.edu

3.4 The brightest star cluster candidate

In their work, Larsen (2002) and Weidner et al. (2004) proved that there is a tight correlation between the V-band magnitude of the brightest star cluster $M_V^{brightest}$ and the global SFR of the host galaxy which is given by:

$$M_V^{brightest} = -1.87(\pm 0.06) \times \log SFR - 12.14(\pm 0.07) \tag{3.17}$$

The above expression was derived from a two-dimensional linear regression fitting of the observation data from Larsen (2002). Knowing $M_V^{brightest}$, one can estimate SFR inverting Eq. 3.17:

$$\log SFR = -0.54(\pm 0.02) \times M_V^{brightest} - 6.51(\pm 0.26) \tag{3.18}$$

In case there will be a correlation between SFR and the K-band magnitude of the brightest star cluster $M_K^{brightest}$, as listed in Table 3.5, it would be relevant to derive a similar relation for the first time in the NIR wavelengths. Figure 3.12 illustrates the brightest clusters in the field for each target. To estimate σ_{M_K} which is the error in the absolute magnitude of the star cluster, we applied the propagation of errors such that $\sigma_{M_K}^2 = \sigma_{m_K}^2 + \sigma_{m_0}^2 + \sigma_{a_c}^2$, where σ_{m_K}, σ_{m_0} and σ_{a_c} are respectively the uncertainties in the apparent magnitude, the magnitude zero-point and the aperture correction.

Name	$M_K^{brightest}$	SFR
IRAS F16516-0948	-18.4±0.2	30
CGCG 049-057	-16.7±0.2	32
IRAS F17578-0400	-17.4±0.1	38
MCG +08-11-002	-18.5±0.2	44
IRAS F17138-1017	-18.9±0.1	45
NGC 3690	-18.9±0.2	55
UGC 8387	-19.2±0.2	80
IC 694	-18.8±0.2	84
IRAS 18293-3413	-19.6±0.1	111
IRAS 19115-2124	-20.6±0.1	127

Table 3.5: The K-band absolute magnitude of the brightest star cluster candidate $M_K^{brightest}$ and an estimate of the star formation rate SFR for each sample. The Kennicutt SFR-L_{ir} was used to derive the value of SFR.

In fact, assuming that our SSC candidate selection criteria (see Section 3.1) are correct,

the upper panel of Figure 3.13 shows that there could be an observational relation between the K-band brightest star cluster $M_K^{brightest}$ and the galaxy SFR. A visual inspection was also done to avoid any confusion between the brightest cluster and luminous foreground stars and to verify that these clusters are not blended (See Figure 3.12).

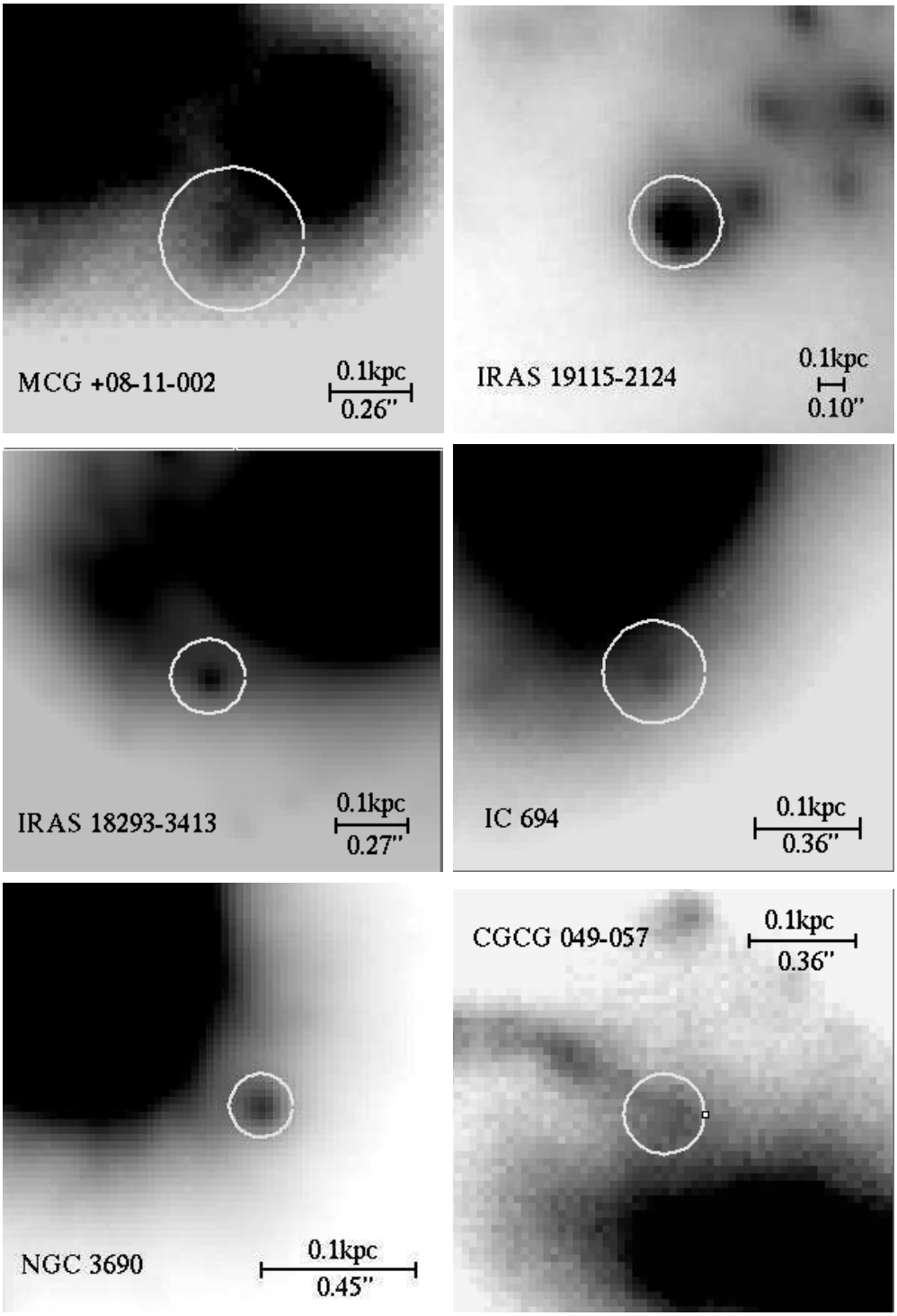
MCG +08-11-002
0.1kpc
0.26"
IRAS 19115-2124
0.1kpc
0.10"
IRAS 18293-3413
0.1kpc
0.27"
IC 694
0.1kpc
0.36"
NGC 3690
0.1kpc
0.45"
CGCG 049-057
0.1kpc
0.36"

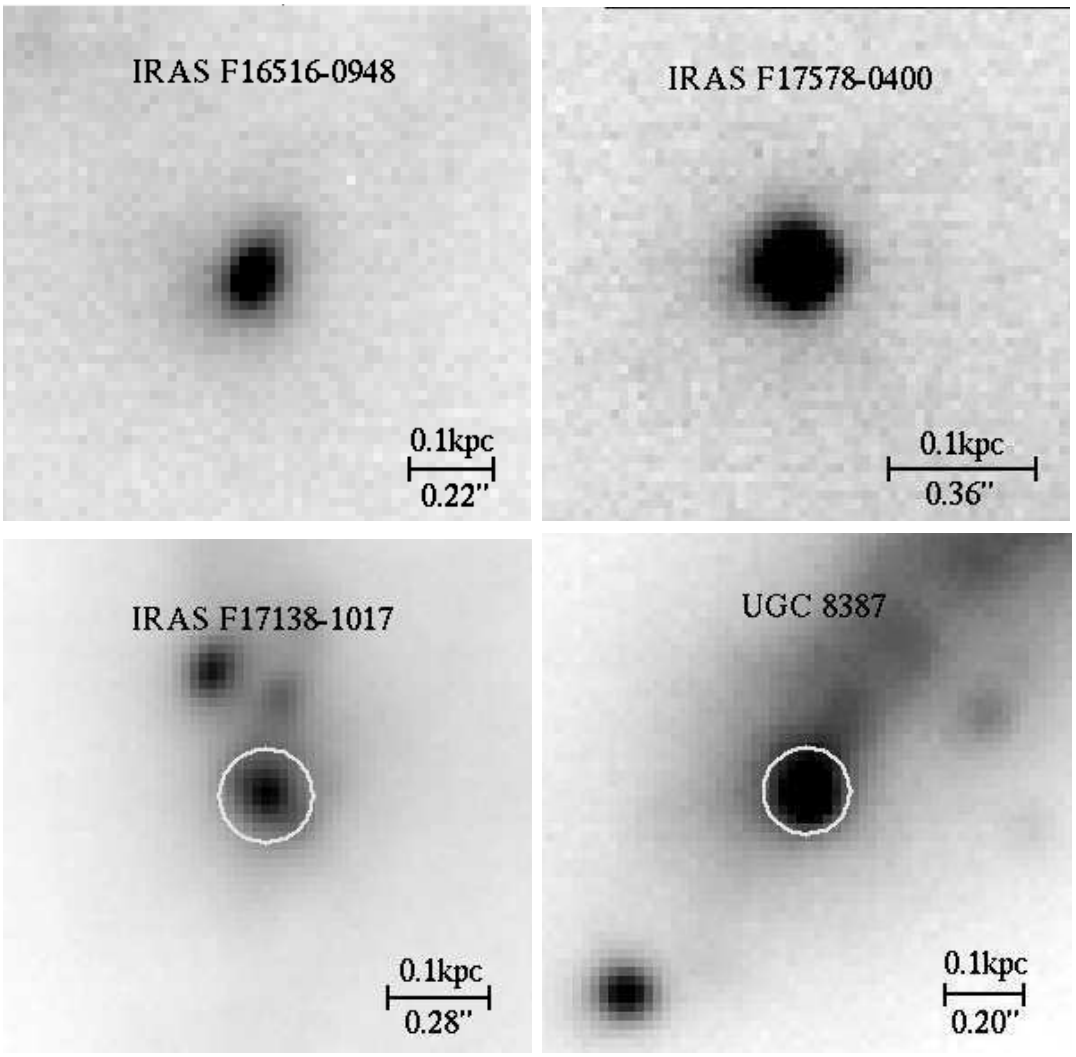

Figure 3.12: The brightest star cluster candidates for each sample. An open circle is used to indicate the brightest cluster if it is surrounded by other sources. We notice that the brightest cluster is elongated for IRAS F165156-0948. This is not surprising since all the point sources in that field are all elongated due to the AO-correction issue.

In addition, the lower panel of Figure 3.13 plots the magnitude of the brightest star cluster as a function of the total number of star clusters with $M_K \leqslant -16$ for each target. The slope of such relation is related with the power-law index η in Eq. 1.7 established by Whitmore (2003) as follows:

From a linear fit of the lower panel of Figure 3.13, one can write:

$$M_K^{brightest} \sim C \log \mathrm{N} \tag{3.19}$$

where C is the slope from the fitting. Since $M_K^{brightest}$ is related to the luminosity of the most luminous star cluster L_{max} by:

$$M_K^{brightest} = M_{max} \sim -2.5 \times \log L_{max} \tag{3.20}$$

Equating Eq. 3.19 and Eq. 3.20:

$$C \log N = -2.5 \times \log L_{max} \tag{3.21}$$

However, as established by Whitmore (2003):

$$L_{max} = N^{\eta} \tag{3.22}$$

Substituting L_{max} in Eq. 3.21, one can finally write:

$$C = -2.5\eta \tag{3.23}$$

Therefore, the power-law index η of the $L_{max} - N$ relation is given by:

$$\eta = -C/2.5 \tag{3.24}$$

From a linear fit of the data points for both plots in Figure 3.13, we derived the following expressions:

$$M_K^{brightest} = -3.9(\pm 0.03) \times \log SFR - 11.8(\pm 0.05) \tag{3.25}$$

and

$$M_K^{brightest} \sim -1.9(\pm 0.03) \times \log N \tag{3.26}$$

The expression in Eq. 3.26 is represented as the black dashed line in the lower panel of Figure 3.13. However, if we exclude the points which correspond to CGCG 049-057 and IRAS 19115-2124, we get $C = -1.7 \pm 0.04$ instead. These points are omitted because the number of the star cluster candidates brighter than -16 absolute magnitude in the first target are statistically too small, whereas the brightest star cluster of the second

target which is very distant ($D = 206$ Mpc) is most likely to be blended.

Using Eq. 3.24, the values of η are respectively equal to 0.76 and 0.68 for $C = -1.9$ and $C = -1.7$. The interpretation of these relations will be discussed in Section 4.5.

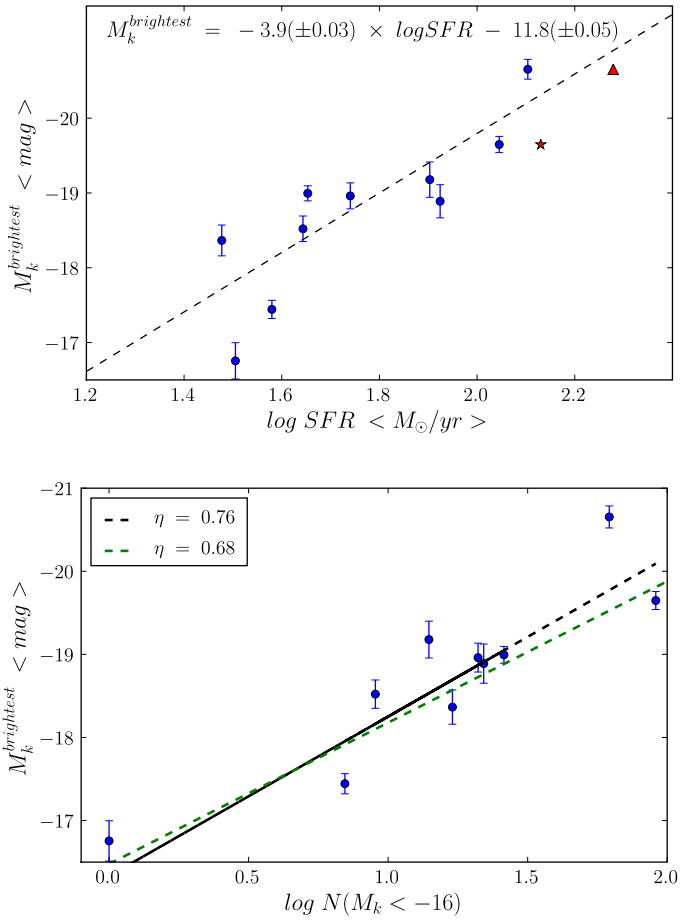

Figure 3.13: *Upper panel:* From observational K-band data, we were able to draw a relation between the brightest star cluster of the galaxy $M_K^{brightest}$ and its SFR. The dashed line represents a weighted linear fit to the data. The red star and the red triangle are respectively the data points of IRAS 18293-3413 and IRAS 19114-2124 while considering the SFR from Mattila et al. (2007) and Väisänen et al. (2008). *Lower panel:* $M_K^{brightest}$ as a function of the logarithm of the number of the star clusters brighter than -16 mag. The black dashed line represents a weighted linear fit considering all the data and its slope corresponds to $\eta = 0.76$, while the green one by omitting CGCG 049-057 and IRAS 19115-214. The linear slope corresponds to $\eta = 0.68$.

Chapter 4

Discussion

4.1 Comparing the SSC candidate LFs with the literature

The results from our fitting procedure in Section 3.2.2 clearly show that a single power-law distribution in the form of $dN(L)/dL \sim L^{-\alpha}$ is a reasonable approximation for young stellar cluster LFs of our sample. Earlier theoretical studies have already reported the same results for the same type of star clusters in merging systems, suggesting that such behaviour would be the imprint of a power-law MF under the following assumptions: a constant cluster formation rate (CFR), a negligible variation of the ambient pressure and the turbulence between the star-forming clouds (Gieles et al. 2006a). The same conclusion was drawn from previous optical data analysis who found that the cluster mass function (CMF) follows the same distribution with $dN(M)/dM \sim M^{-\gamma}$ (e.g. Gieles et al. 2006b). Moreover, as highlighted in Section 1.4.3, these star clusters are formed through the collapse of their giant molecular cloud progenitors, which were shown to exhibit a power-law mass function as well (e.g. Solomon et al. 1987, Elmegreen & Efremov 1997).

We note, however, that a single power-law will no longer be the best approximation if a bend occurs at the faint end of the SSC LF, such as in our case for IRAS 18293-3413. This will be discussed in Section 4.2. Furthermore, some early case studies of young star clusters in M51 and the Antennae system reported a gaussian shape of the LF (e.g. Fritze-v. Alvensleben 1999, Anders et al. 2007). Our results do not agree with this lognormal distribution. It is possible that since they were observing in the optical regime, star cluster candidates which are located in the very enshrouded dusty regions of the galaxies may have been hidden, due to the high extinction level. Fall et al. (2009)

and Whitmore et al. (2010) argued that these contradictions in the LF/MF shapes are due to the difficulties encountered in getting the exact LF/MFs.

Apart from the existence of a turnover in one of our SSC LFs, another particularity of our results is that the power-law indices derived from the weighted linear least squares fitting are generally smaller than 2 for both ways of binning. In what follows, we will discuss the reasons for any bend in a LF, and then we will investigate the origins of a shallower slope.

4.2 Evidence for a turnover at the faint end

A closer look at the SSC LFs indicates a bend in the faint end for IRAS 18293-3413. According to various studies, the primary explanations of such a break of the single power-law would be due to the effects of sample binning or a bias from observational incompleteness. While a careless binning may produce an artificial flattening of the binned LF, inaccurate incompleteness correction due to a non-robustness of the simulation will bias its shape toward the faint-end (Maíz Apellániz & Úbeda 2005, Anders et al. 2007). In our case, we excluded the binning effects since both LFs derived from two different ways of binning exhibit the same trend, as can be seen in Figure 3.6. In addition, we assume that our completeness fractions are correct as they were derived from a simulation which used an artificial star having the same PSF as a star cluster candidate. Moreover, if the starting-point of the bend was close to the completeness limit, then one most probably could think of an unsuccessful completeness correction, whereas the LFs start to bend at $\sim$ 2 mag above it in the case discussed here.

If a turnover in the LF is neither caused by the binning nor the incompleteness, we could then suggest that a truncated mass function itself could be another factor. This argument is based on the concept that the MF and its integrated LF may follow the same distribution, as already discussed in the previous section (e.g. Elmegreen & Efremov 1997, Gieles et al. 2006a). Some physical reasons are proposed in the next three subsections to explain the truncation.

4.2.1 A scatter in the star formation efficiency

Based on various studies, Parmentier & Gilmore (2007) were able to establish a relation between the initial mass m_{init} of a gas-free bound star cluster and the mass m_{cloud} of

the gas cloud progenitor. This relation can be written as:

$$m_{init} \; = \; F_{bound} \; \times \; \epsilon \; \times \; m_{cloud} \tag{4.1}$$

where F_{bound} is the mass fraction of bound clusters after gas removal. This quantity is suggested to correlate well with the star formation efficiency ϵ (e.g Lada et al. 1984, Boily & Kroupa 2003). Therefore, assuming a negligible variation in the ambient pressure, Eq. 4.1 can be reduced to:

$$m_{init} \; \sim \; \epsilon \; \times \; m_{cloud} \tag{4.2}$$

Gieles et al. (2006a) and Parmentier & Gilmore (2007) argued that ϵ will steadily increase with m_{cloud} until it reaches a point where the cloud specific binding energy will increase, inducing an increase of the cloud velocity dispersion. However, the latter will decrease ϵ due to large variations in the turbulence and the magnetic field pressure. Therefore, these counteracting effects in the m_{cloud} - ϵ relation would result in a truncated mass function (Parmentier & Gilmore 2007).

4.2.2 A selective destruction effect

Theoretical simulations argue that a turnover of the LF could be an imprint of a selective destruction when young star clusters are disrupted by stellar evolution. As already mentioned in Section 1.4.3, star clusters will be gravitationally unbound due to the gas removal during the supernova phase. Despite their survival from the disruption, they will be unlikely to escape the mass segregation effect while searching for a new virial equilibrium. Low-mass stars will mainly contribute to that mass-loss rate due to their higher velocity dispersion compared to that just acquired after the star clusters are revirialized. Numerical models suggest that the escape of these low-mass stars to form field stars will be observed as a natural bend in the cluster mass function (e.g. Boily & Kroupa 2003, Bastian & Goodwin 2006, Goodwin & Bastian 2006).

4.2.3 A physical upper mass limit in a truncated CIMF

From recent numerical models of synthetic cluster population (SCP) by Gieles et al. (2006a) and Larsen (2009), it has been shown that a Schecter CIMF with the form of $dN(M)/dM \; \sim \; M^{-\gamma} \exp(M/M_c)$ would result in a naturally truncated CMF having a physical upper mass limit M_c. To create the SCP in three different filters (BVI), Gieles et al. (2006a) ran the theoretical simulations under the following assumptions: the index γ of the Schecter CIMF is equal to 2 and the mass function breaks at $M_c \sim 10^5 M_\odot$, the

generated artificial star clusters have the same properties as those observed in M51, the cluster formation rate is constant, and finally the star clusters will undergo disruption and stellar evolution. The same detection limit used to select the SCs in M51 were considered to construct the SCP LF. Their analytical models agreed with their results from the observations. LFs with a turnover at the faint end were derived for all the filters in both cases.

Based on the same model, Gieles et al. (2006a) showed that the location of the bend will be at higher luminosities in redder filters and that a double-power law distribution will be more appropriate to fit the LF. In that case, the values of the slopes will be steeper at higher luminosities (e.g. Whitmore et al. 1999, Larsen 2002) and steeper at redder filters (e.g. Gieles et al. 2006b, Elmegreen et al. 2002). Note that Fall et al. (2009) and Whitmore et al. (2010) strongly advocate a universal power-law of $\alpha = 2$, and argue that bends and turnovers seen in the literature result from relative bias analysis methods.

4.3 A shallower slope

Despite the correction for incompleteness and assuming a negligible foreground contamination for the GEMINI/ALTAIR data, the power-law indices from a linear conservative fit, which are listed in Table 3.2, are still significantly lower than the typical index $\alpha = 2$, except for IRAS F16516-0948. Our results support the statement that the SSC LF in interacting galaxies is not a universal power law with $\alpha = 2$, as predicted in earlier studies (overviews can be found for example in de Grijs et al. 2003 or Whitmore 2003). Many studies find the index to span between 1.8 to 2.4 (e.g. Elmegreen & Efremov 1997, Whitmore et al. 1999, Elmegreen et al. 2002). Surprisingly, the values of α in our case do not fall in between that range, except for IRAS F16516-0948. Adamo et al. (2010) encountered the same situation in their recent work, when they found $\alpha \sim 1.5$ for the starburst galaxy Haro 11.

Apart from photometric uncertainties, our shallower slope may simply arise from contamination by blending or from age-extinction effects. Nevertheless, previous numerical studies have already found that such an unusual LF behaviour may occur under some circumstances, such as a mass-dependent disruption model (Gieles et al. 2006a, de Grijs & Parmentier 2007). These multiple factors will be discussed in the rest of this section.

4.3.1 Effects of blending

Referring to the distances of our sample, 45 < D (Mpc) < 207, one should agree that crowding will most probably contaminate the photometry despite the use of NIR AO imaging. Our aperture radius with a size of 0.2″ corresponds to a physical size of 44 - 199 pc and spatial resolution to the half of these values, depending on the distance of each target. Compared with the effective radius of a super star cluster from the literature, which is in the range of 3 to 5 pc, such aperture size may contain more than one SC candidate. However, considering the surface number density of our galaxy field and that from a deep HST nearby galaxy which is the Antennae system, we do not expect more than one object within the size of our aperture radius (Whitmore et al. 1999). Following this idea, the effects of blending alone cannot produce a significant deviation from the power-law index 2. We should note that the above range of the SC typical size was derived from the observations with HST/WFPC2 camera of nearby galaxies much closer than our sample such as the Antennae (21.7 Mpc) and NGC 3610 (25.6 Mpc) (Whitmore 2003).

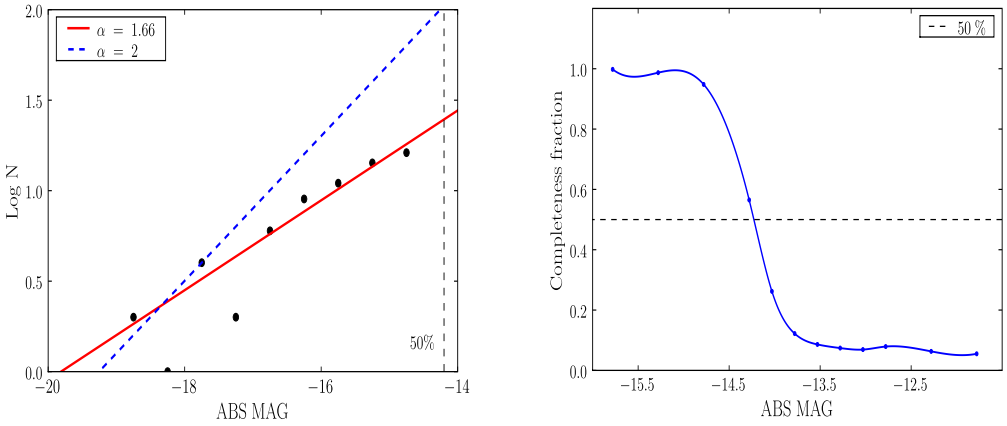

Figure 4.1: *Left panel:* The black points represent SSC LF for IC 694. The red solid line and the blue dashed line are respectively a LF linear fit for $\alpha = 1.6$ and $\alpha = 2$. The vertical dashed line is the 50 % completeness limit. *Right panel:* The blue line is the output from MC simulation used to correct the data for observational completeness. The horizontal dashed line is the 50 % completeness limit in this case.

Simultaneously, we adopted the method used by Adamo et al. (2010) to quantify this effect in our data. This is done by giving a rough estimate of the blended objects in making a linear fit, assuming that the LF is a power-law with $\alpha = 2$ and that the number of objects in the second or the third bin is correct. Using the relation in Eq. 3.12,

we got A = 0.4 for $\alpha = 2$ and from Eq. 3.4, we estimated the intercept associated with that index, after deciding the bin to be considered. After performing the test with our data, we estimated 61 to 75 % of blended objects for those with shallower slopes. These fractions are quite high and do not agree with the completeness test. The left panel of Figure 4.1 illustrates the test for IC 694. While the linear fit with a slope $\alpha = 2$ implies that the sample is already ~ 40 % incomplete at around -16 absolute magnitude, our simulation, which can be seen in the right panel, places that magnitude range still well above 99 % completeness limit. Therefore, though because of our spatial resolution, blending cannot be definitely ruled out, it seems clear that the effect cannot be a major factor in flattening the slope.

4.3.2 Age - extinction effects

As we are observing in the K-band filter, we expect a biased detection due to the extinction effect. Older SSC candidates will be preferentially detected, in the absence of a significant "red excess" factor. Mengel et al. (2005) argued that a SC which was previously born in a high extinction region would be less extinguished by the age of 8 - 9 Myr. From a plot of extinction A_v of each individual young SC with respect to its age in the Antennae system, they found that as the cluster ages, it will be less affected by the extinction since the cluster emerged from its natal dust cocoon. Therefore, in spite of a mass-independent disruption model, the slope of the integrated LF will likely differ from individual ones drawn from star cluster populations with different ages and extinction. If the distruption model is mass-dependent, the SC LF will most likely have a shallower slope (Mengel et al. 2005, Gieles et al. 2006a). This will be discussed next.

4.3.3 Mass-dependent disruption model

Based on the same model which was described in Section 4.2, Gieles et al. (2006a) also showed that the slope α will be lower than 2 if the effect of cluster disruption is included in the initial conditions of the simulation. While stellar evolution occuring in the first few 100 Myrs will obviously affect the cluster MF at older ages, infant mortality which is another disruption process responsible for a high mass-loss rate of a given cluster population may strongly lower the slope as simulated by Gieles et al. (2006a).

As a cluster evolves with Hubble time, it will become marginally unbound, hence it will get disrupted easily and it will consequently lose its low-mass stars. On the other

hand, because a mass-dependent *infant mortality* mainly destroys the young star clusters in the first few Myrs within the population, this mass-loss will certainly be significant by changing the original shape of the luminosity function. The destruction of the low mass SCs located in the faint magnitude bins will flatten the original slope (e.g. Lada & Lada 2003; de Grijs & Parmentier 2007). Nevertheless, it is difficult to accurately conclude whether the disruption is really the main cause of the shallower slope until we analyse data from other filters so that we would be able to derive LF with different age bins. And in that case, another challenge would be to determine which disruption process is the most dominant (Mengel et al. 2005).

4.4 Impact on cluster formation and evolution

As already highlighted in Section 1.4.3, a star cluster will likely be a potential progenitor of a present day GC if its stellar IMF is originally steep enough in the favor of the cluster being less vulnerable to further disruption (e.g. Vesperini & Zepf 2003, de Grijs 2005). This is because a mass-dependent disruption model will enhance mass-loss rate and hence will lead to a shallower slope of the MF, or even to the dissolution of the cluster, by being disrupted by the internal and external mechanisms (Mengel et al. 2005). Therefore, considering the shapes of our SSC LFs as discussed in Sections 4.2 and 4.3, one may think that the SSC candidates in our sample are unlikely to be proto-GCs. Moreover, suggesting that a shallower slope as well as bend in the LF would be the imprint of a mass-dependent infant mortality, these SSC candidates could actually become gravitationally unbound and could be older than 10 Myrs old, since the disruption occurs in the few Myrs of their lifetime. In brief, either a long-term survival of the cluster or its potential to be considered as proto-GC strongly depends on the shape of its initial mass function (Vesperini & Zepf 2003, de Grijs 2005, de Grijs & Parmentier 2007).

4.5 Brightest star cluster - SFR relation

Assuming that our SSC candidate selection criteria (see Section 3.1) are correct, the upper panel of Figure 3.13 shows that there could be an observational relation between the K-band brightest star cluster $M_K^{brightest}$ and the galaxy SFR as expressed as follows:

$$M_K^{brightest} \;=\; -\,3.9(\pm 0.03)\;\times\;\log SFR\;-\;11.8(\pm 0.05) \tag{4.3}$$

A visual inspection was also done to avoid any confusion between the brightest cluster and luminous foreground stars and to verify that these clusters are not blended (see Fig-

ure 3.12). Larsen (2002), Weidner et al. (2004) and Bastian (2008) already noticed the correlation between these two quantities as seen in the optical and provided their respective explanations. Since their analyses were carried out considering optical observations, *this work is one of the first determinations of such a relation in the NIR wavelengths.*

A simple statistical explanation was the very first argument proposed by Larsen (2002) and also argued by Whitmore (2003). Apart from the size-of-sample effect, two other main reasons which are mutually different, were suggested by Weidner et al. (2004) and Bastian (2008). In what follows, we will highlight these arguments and later we will decide whether they can be adopted to explain the similar correlation occuring in the NIR wavelengths or not.

4.5.1 A size-of-sample effect

Larsen (2002) and Whitmore (2003) showed observationally that the more star clusters there are forming in a galaxy (*i.e* with a high SFR), the higher will be the probability to also sample those which are the brightest of the overall population. In that case, the $M_K^{brightest}$ - SFR relation is "only" a statistical effect. In fact, the plot in the lower panel of Figure 3.13, $M_K^{brightest}$ as a function of log $N(M_k \leq -16)$, is directly related with the $L_{max} - N$ relation established by Whitmore (2003) using Eq. 3.24 . Moreover, converting η to α with the relation $\eta = 1/(\alpha - 1)$ by Hunter et al. (2003), we found that the slopes at the bright end of the LF are respectively equal to $\alpha = 2.31$ and $\alpha = 2.47$ for $\eta = 0.76$ and $\eta = 0.68$. Such values are interpreted to be the result from a size of sample effect: there are no physical conditions to constrain the formation of the very bright cluster of the sample and the mass-to-light ratio is independent of L_{max} which is a tracer of the brightest cluster (Portegies Zwart et al. 2010). These arguments however contradict those of Weidner et al. (2004) and Bastian (2008) who explain the same observational relation.

4.5.2 A reflection of the most massive cluster - SFR relation?

Weidner et al. (2004) converted the mass into luminosity using a mass-to-light ratio quantity and then derived an expression which directly relates the total SFR of the galaxy with the mass of the star cluster (see Eq. 3.17). Therefore, the brightest cluster - SFR relation would naturally be expected if the most massive cluster is always the brightest. To assess this assumption, they created a cluster population having a power-law MF and

further ran a MC simulation to check how the visual absolute magnitude would evolve over 500 Myr for clusters with different masses. When repeating the same procedure using a different cluster formation rate (CFR), the experiment always revealed that the heaviest one is the brightest, except for a very short period (5 % of the overall time) which is insignificant compared to the uncertainty in the cluster age.

4.5.3 Or a reflection of the current SFR?

On the other hand, Bastian (2008) proposed that the youngest clusters are the brightest. Therefore, a brightest star cluster - SFR relation would reveal the current SFR of the galaxy. This argument is based on a Monte Carlo simulation of a cluster population run with different CFR. The results reproduced nearly the same trend when they created the artificial clusters with a truncated Schecter MF at $M_C \sim 10^6\ M_\odot$ and a random age between 0 and 100 Myr. The cumulative distribution of the fraction of MC realisations indicated that young clusters dominate the population and that the most massive clusters, which are often older, are unlikely to be the brightest especially for a high CFR.

From these multiple point of views, it is very difficult to draw a firm conclusion regarding our own results because of the wavelength difference and the lack of age information. It would be relevant to simulate the behaviour of an artificial K-band cluster population over a period of time, and observationally a bigger sample is needed to check the reliability of the relation. Nevertheless, we should not forget that K-band observations suffer less from extinction and that they might be less sensitive to the youngest objects.

4.6 Any correlation between the optical and NIR relations?

As already shown in Eq. 3.17, Larsen (2002) and Weidner et al. (2004) established an empirical relation of the brightest star cluster with the galaxy SFR from optical observations. In this work, from a weighted linear fit, we got a similar relation in Eq. 4.3 from K-band NIR data analysis. Subtracting Eq. 4.3 from Eq. 3.17, we get the following relation:

$$V - K \sim 2 \log SFR \tag{4.4}$$

As the SFR increases with the V - K color, such correlation may indicate a color-age effect or a "red excess" in the K-band data when nebular emission dominates in the waveband. Investigating the reason of such a relation is beyond the scope of this work, though further analysis would possibly be interesting.

Chapter 5

Conclusions and further work

We have used near-infrared adaptive optics imaging to study super star cluster candidates in the star-forming regions of a representative sample of interacting luminous infrared galaxies. This work is dedicated to improving our current understanding of galaxy formation and evolution in the early Universe by directly studying the formation of massive star clusters (SCs) in the extreme environments of local interacting LIRGs. To this end, we derived the first ever K-band luminosity function of SSC candidates and established a relation between the brightest star cluster and the galaxy star formation rate in the NIR wavelengths.

The galaxy sample was selected over the redshift range $0.01 < z < 0.05$ and it was observed in the K-band filter using two different NIR AO instruments: the NAOS-CONICA (VLT/NACO data) and the ALTAIR NIRI (GEMINI/ALTAIR data), with a pixel scale of $\sim 0.02''\text{pix}^{-1}$ and a FWHM $\sim$ $0.1''$ for the point sources in both cases. For each target, we have combined the individual frames to get the final co-added image once the bad frames were excluded and a de-striping process was accomplished. We derived and added in the FITS header of each image its WCS coordinates using the IRAF CCMAP task. While SExtractor was used for object detection, IRAF/DAOPHOT was chosen to perform aperture photometry. We calibrated the magnitude scale of the science images and derived aperture corrections.

We set selection criteria to select potential SSC candidates amongst the detected objects from SExtractor. The selection was quite difficult as we were only working with a single filter. It was mainly based on photometric uncertainties and visual inspection because the value of the FWHM output by SExtractor depended too strongly on the

BACK_SIZE parameter and was not reliable. We found that most of the candidates were located on top of the "extended regions"of the galaxy (*i.e.* in the strongly star-forming regions).

For a more realistic LF, we corrected the data for photometric incompleteness and we used two different methods of binning. We ran Monte Carlo completeness simulations with different background levels to obtain a 50 % completeness limit and to correct the data for that bias. We should note that we assumed that an artificial star would be a good representation of a star cluster candidate while building the simulation. The number of SSC candidates generally increased with decreasing absolute magnitude. Therefore, we applied a weighted linear fit to the data. We then used the relation by Elmegreen & Efremov (1997) which relates the best-fit slope A with the index α of a power-law distribution of the form $N(L)dL \sim L^{-\alpha}dL$. For the sample binning, constant and variable bin sizes were adopted in constructing the SSC LF to derive two values of α for each target. The indices from the constant bin size method were generally ~ 0.2 shallower than those from the other method, though this difference is of the order of uncertainties in the data and fitting. In addition, we investigated the effect of foreground contamination for those fields with low galactic latitude. This was done by comparing the value of α before and after a decontamination process. Although the contamination was generally negligible looking at the values of the indices, the VLT/NACO data were the ones more affected by the effect. After constructing the SSC K-band LFs, and then fitting a power-law distribution to their shapes, the indices $\alpha \sim 1.5 \pm 0.2$ were generally significantly shallower than most slopes observed in the optical, which are tipically ~ 2. Moreover, a bend occured in the LF at fainter magnitudes for IRAS 18293-3413.

We plotted the K-band absolute magnitude of the brightest star cluster candidate $M_K^{brightest}$ as a function of the star formation rate SFR of the galaxy. This is the first time such relation has been shown for a NIR SSC sample. However, it is similar to the one in the optical wavelength derived by Larsen (2002) and Weidner et al. (2004). SFR was derived by considering the galaxy infrared luminosity L_{ir} to be the SFR tracer, then using the Kennicutt (1998a) $SFR-L_{ir}$ relation. We established the following empirical relation from a weighted linear fit to the data: $M_K^{brightest} = -3.9(\pm 0.03) \times \log SFR - 11.8(\pm 0.05)$. Finally, we plotted $M_K^{brightest}$ with the logarithm of the number of the star clusters brighter than -16 mag. From the fit, we got a slope approximately equal to 1.9 which corresponds to a value of $\eta \sim 0.76$ in the relation $L_{max} \sim N^{\eta}$.

After analysing the data, we then interpreted our results. We note that we have assumed that our incompleteness correction was correct and the effects of sample binning and foreground contamination were not significant. In addition, we adopted the argument that the cluster mass function generally follows the same distribution as that of a luminosity function. Listed here are the main conclusions of this work:

1. This thesis reinforces that SSC LFs are reasonably well-fitted by a single power-law. However, the shallow slope we found or/and the existence of a turnover at the faint end in one of our targets are not usual behaviours of LFs in the literature.

2. Although the effects of blending would lead to a shallower slope, it is however hard to believe that crowding alone would significantly lower the power-law index from 2 to $\sim$ 1.5. One may additionally suggest age-extinction effects or mass-dependent cluster models to be the reasons of such low values of α.

3. Since the turnover with IRAS 18293-3413 starts at 2 mag above the 50 % completeness level, the reason for the trend cannot be observational incompleteness. A truncated MF could rather be a contributing factor. If the truncation does not naturally originate from the existence of a physical upper mass limit in a truncated CIMF, a scatter in the SF efficiency or a selective mass-dependent destruction effect could be other explanations.

4. As mentioned above, both a shallower slope and a bend in the LF are possibly the signature of a mass-dependent cluster disruption model where, low-mass star clusters are the ones likely to be destroyed in their first 10Myr of age. However, this argument does not support the concept of a universal single power-law LF/MF and such mode of disruption would certainly lead to a gravitationally unbound star cluster. Therefore, depending on the CIMF, the cluster will either dissolve over the Hubble time or it will evolve to become a globular cluster if it has reached a new equilibrium after the disruption.

5. A relation between the brightest star cluster and the global galaxy star-formation rate in the NIR wavelengths could be related to the probability of the most massive clusters being formed in the most intense SF regions, and/or be a reflection of the level of current SFR where the youngest SSCs are the brightest. On the other hand, the values of $\eta \sim 0.68$ - 0.76, which correspond to the power-law indices $\alpha \sim 2.31$ - 2.47 at the bright end of the LF, would rather indicate that the magnitude of the most luminous

star cluster statistically increases with the number of the clusters and that SSC LFs obey universal power-law with slope $\alpha \sim 2$.

Note, however, that this work is based on observations with a single filter and that estimating the ages and the masses of the star cluster candidates were beyond the scope of this thesis. Assumptions regarding PSF size and distribution of SSC candidates with respect to different backgrounds were adopted while running the MC completeness simulations. Therefore, to strengthen the analysis of our work and to draw firm conclusions of our results in the future, we will re-run the simulations with a more careful photometric completeness analysis. We will definitely estimate the physical characteristics of the selected star cluster candidates with the help of archival HST data to be able to constrain the models and more quantitative blending effect simulations will be done in the future.

This thesis is a pilot study since we are in the process of imaging a larger sample of southern LIRGs and starbursts with the VLT/NACO to find many more SSC candidates and to bring the number of the targets from 10 to 40. Finally, we plan to extend the wavelength range of the observed sample to sub-millimeter and radio, using ALMA and eMERLIN, to study in high spatial resolution the gas disks and giant molecular clouds of these targets to understand the triggering of SSC formation in the turbulent interactions of LIRGs and starbursts.

Appendix A

The spatial distribution of the SSC candidates

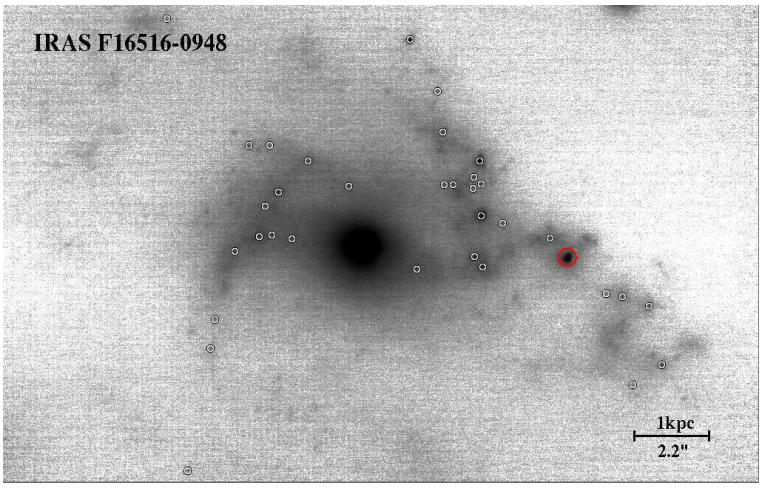

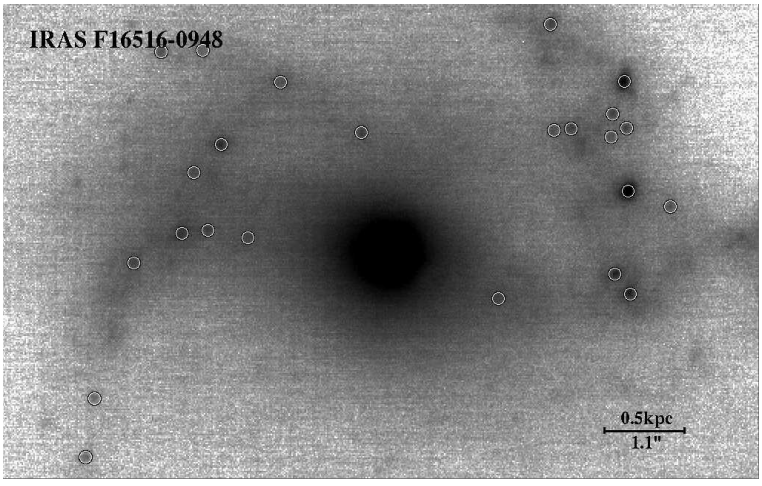

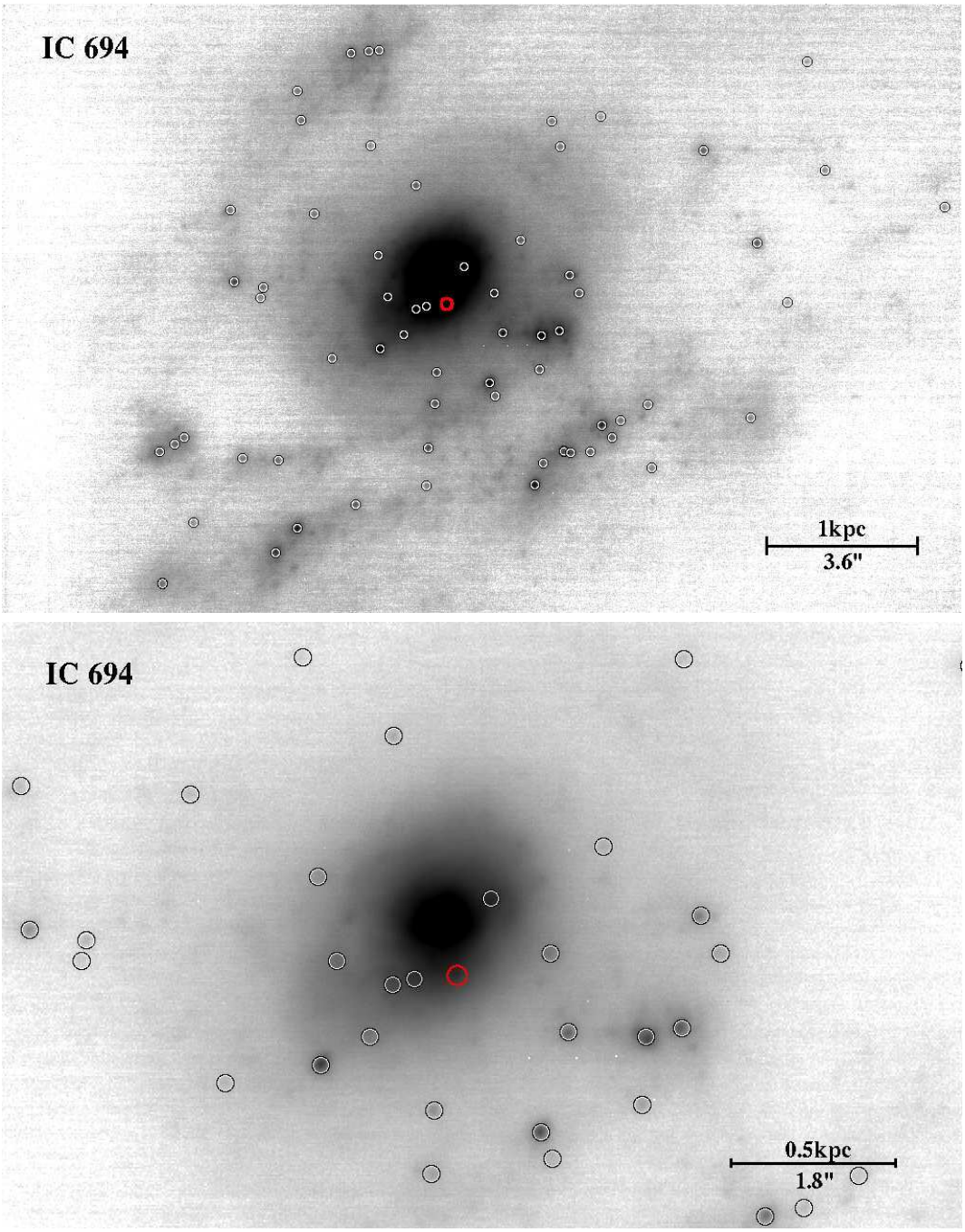
IC 694
1kpc
3.6"
IC 694
0.5kpc
1.8"

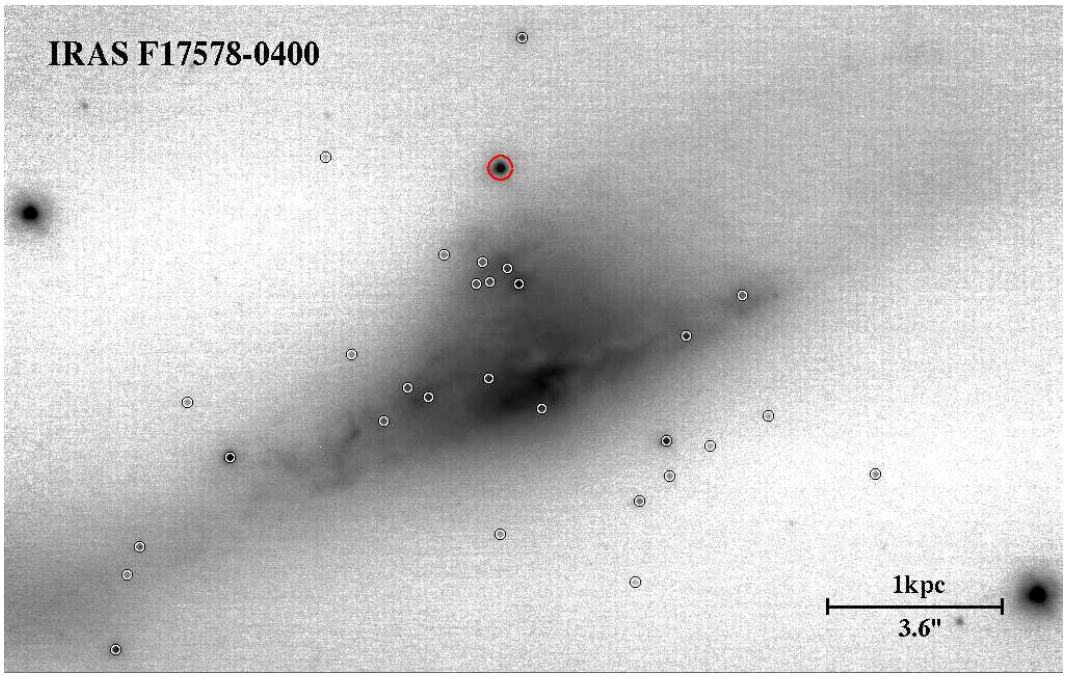
IRAS F17578-0400
1kpc
3.6"

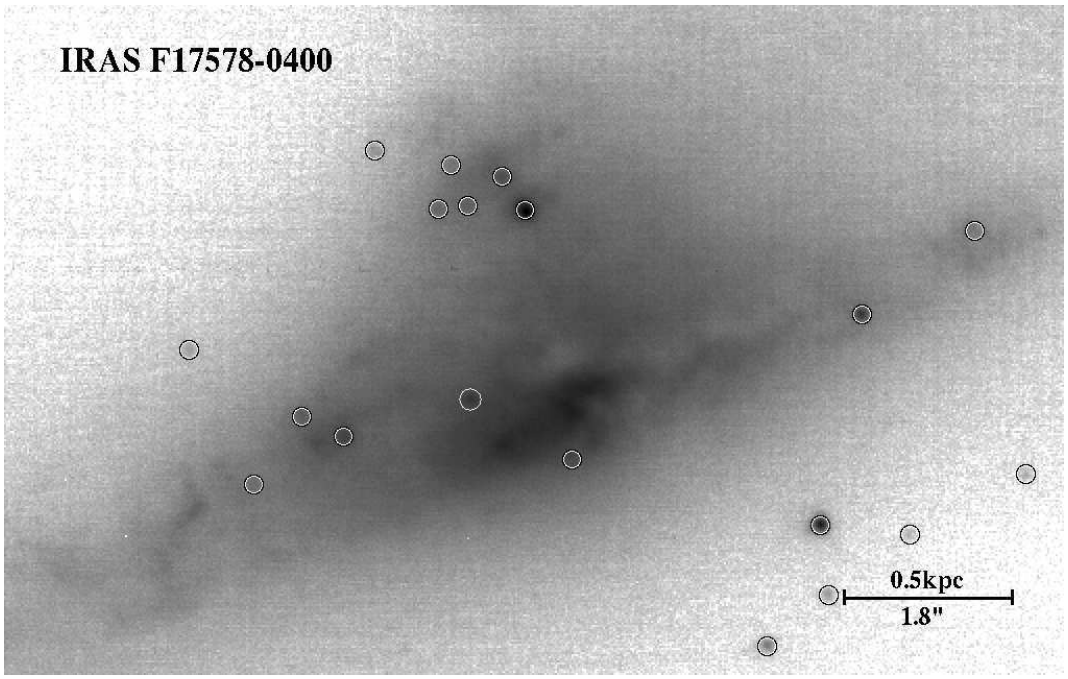
IRAS F17578-0400
0.5kpc
1.8"

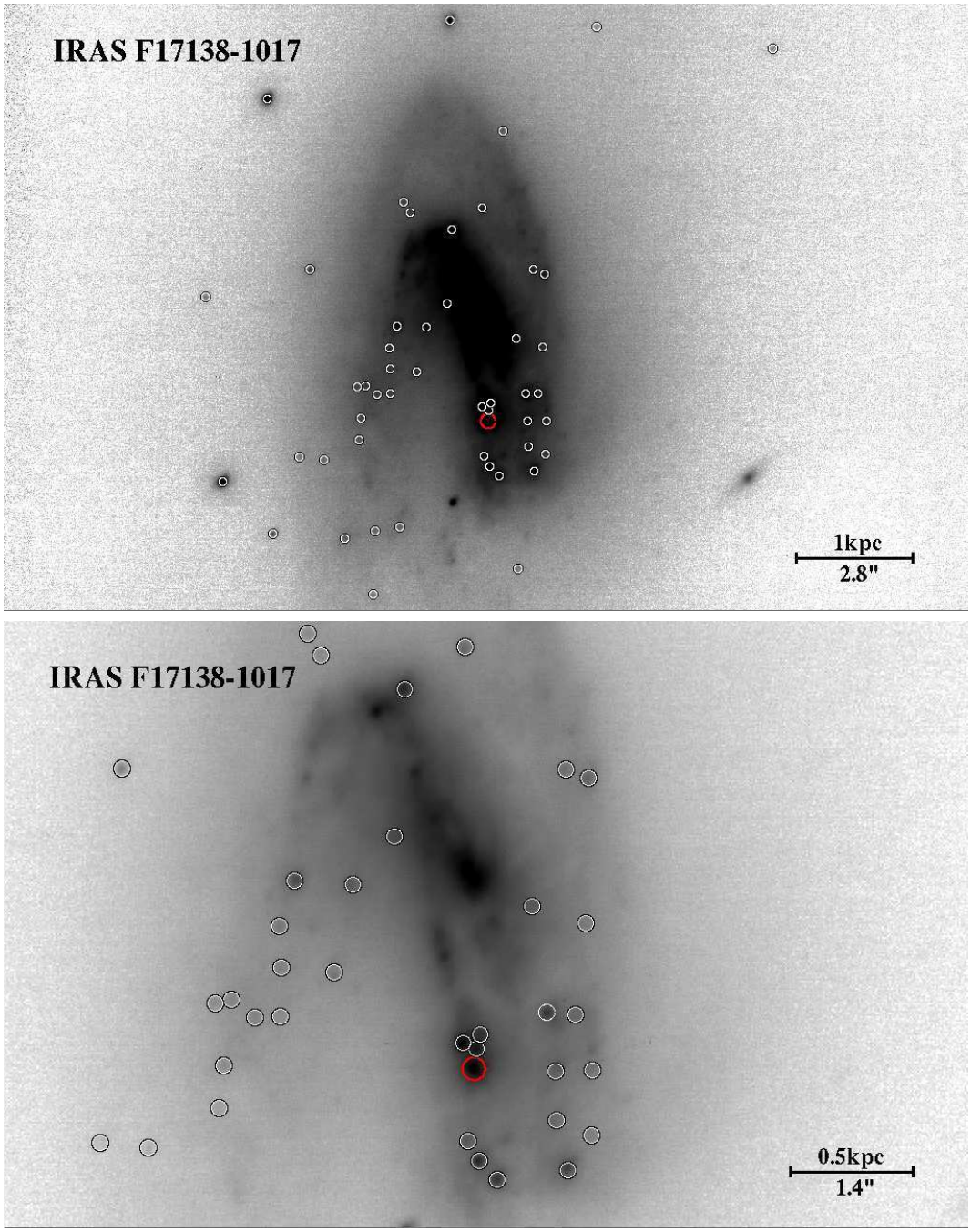
IRAS F17138-1017
1kpc
2.8"
IRAS F17138-1017
0.5kpc
1.4"

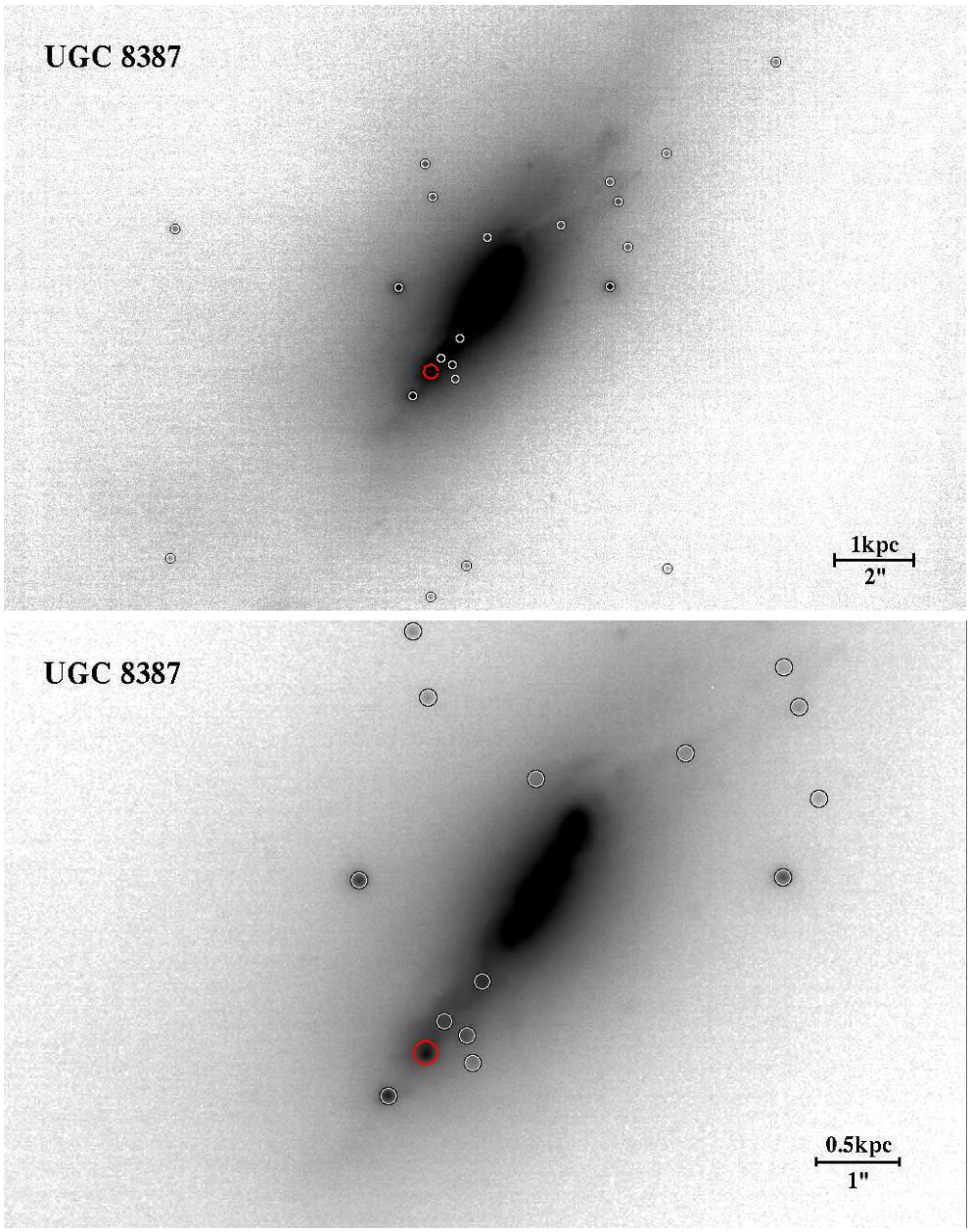
UGC 8387
1kpc
2"
UGC 8387
0.5kpc
1"

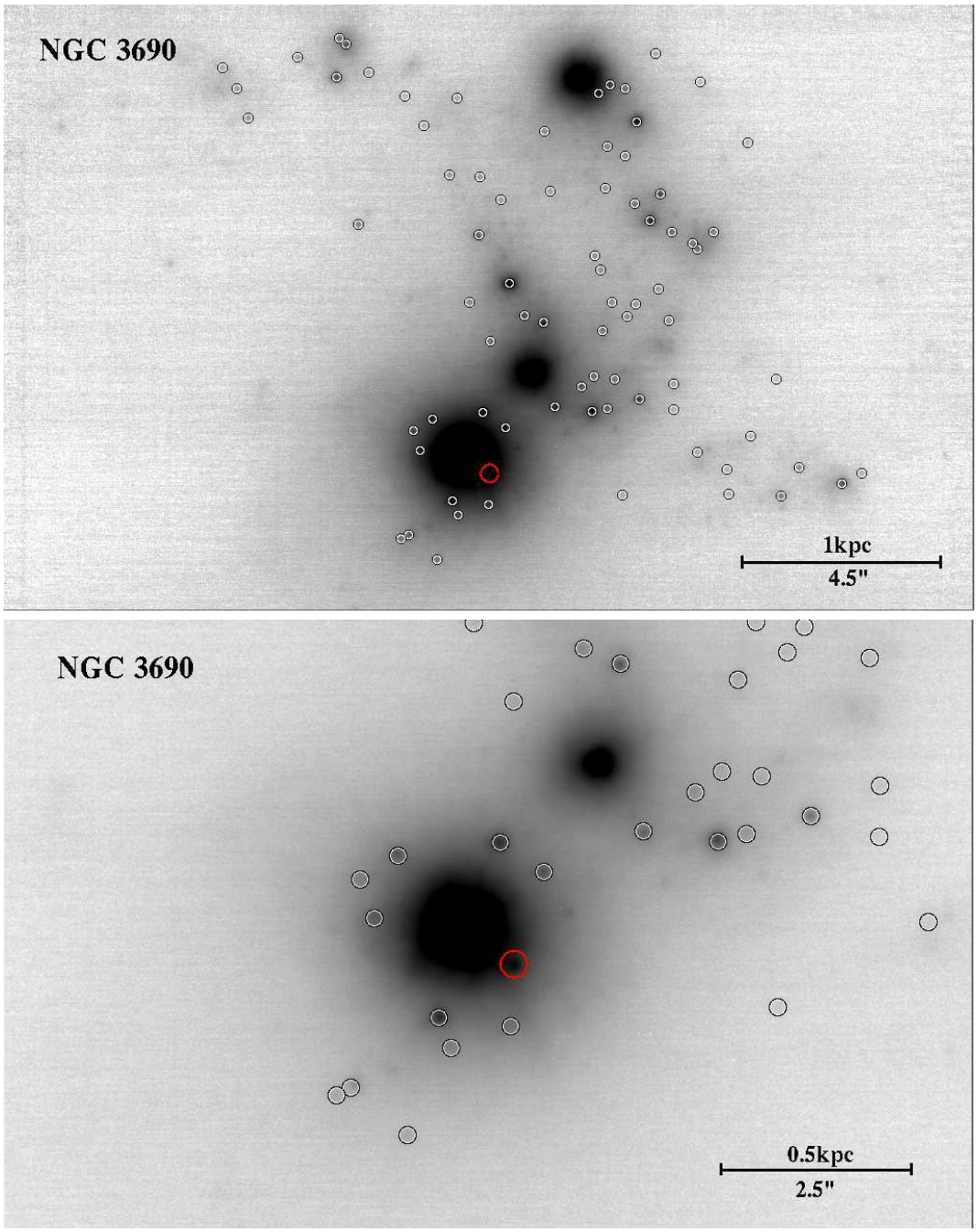
NGC 3690
1kpc
4.5"
NGC 3690
0.5kpc
2.5"

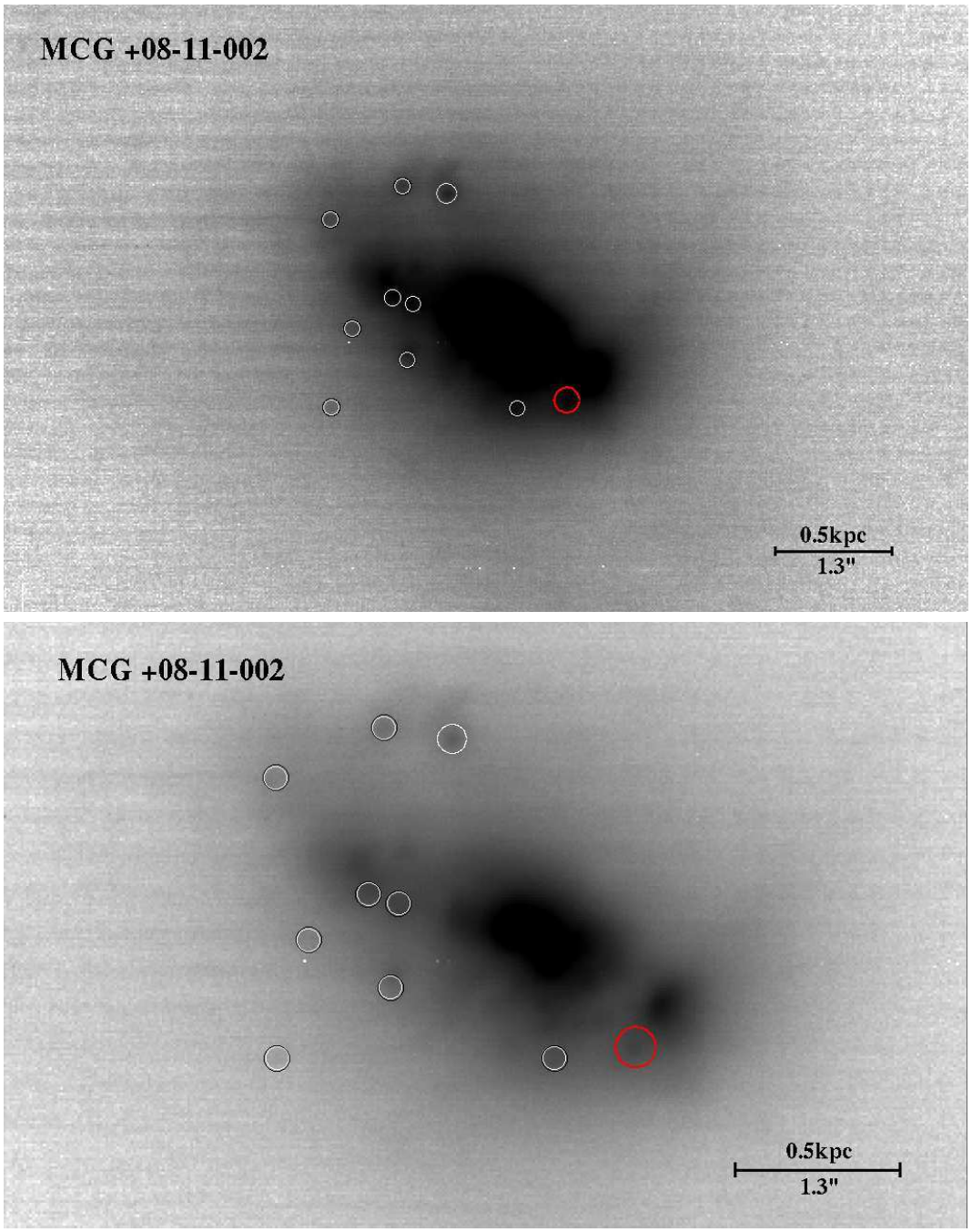
MCG +08-11-002
0.5kpc
1.3"
MCG +08-11-002
0.5kpc
1.3"

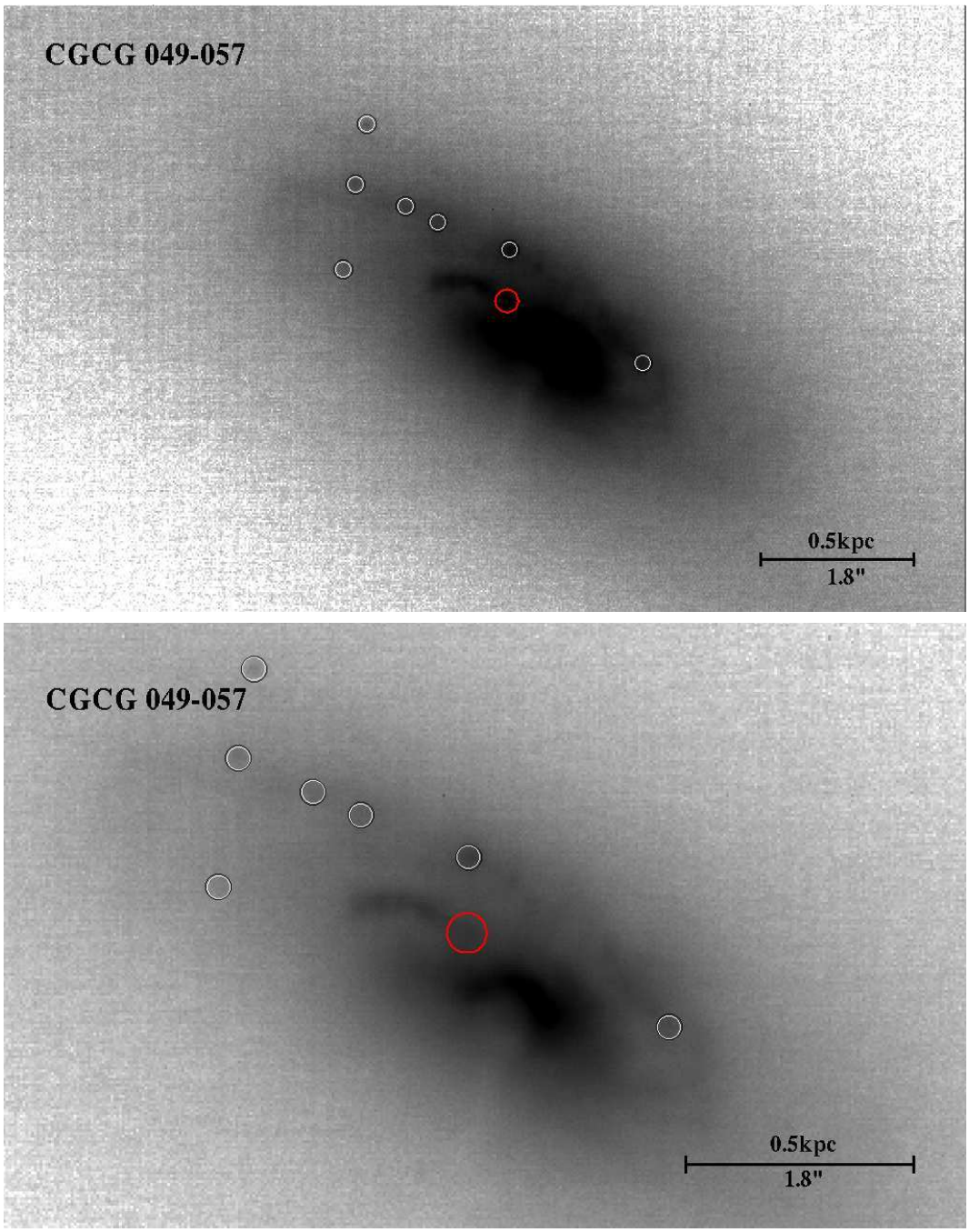
CGCG 049-057
0.5kpc
1.8"
CGCG 049-057
0.5kpc
1.8"

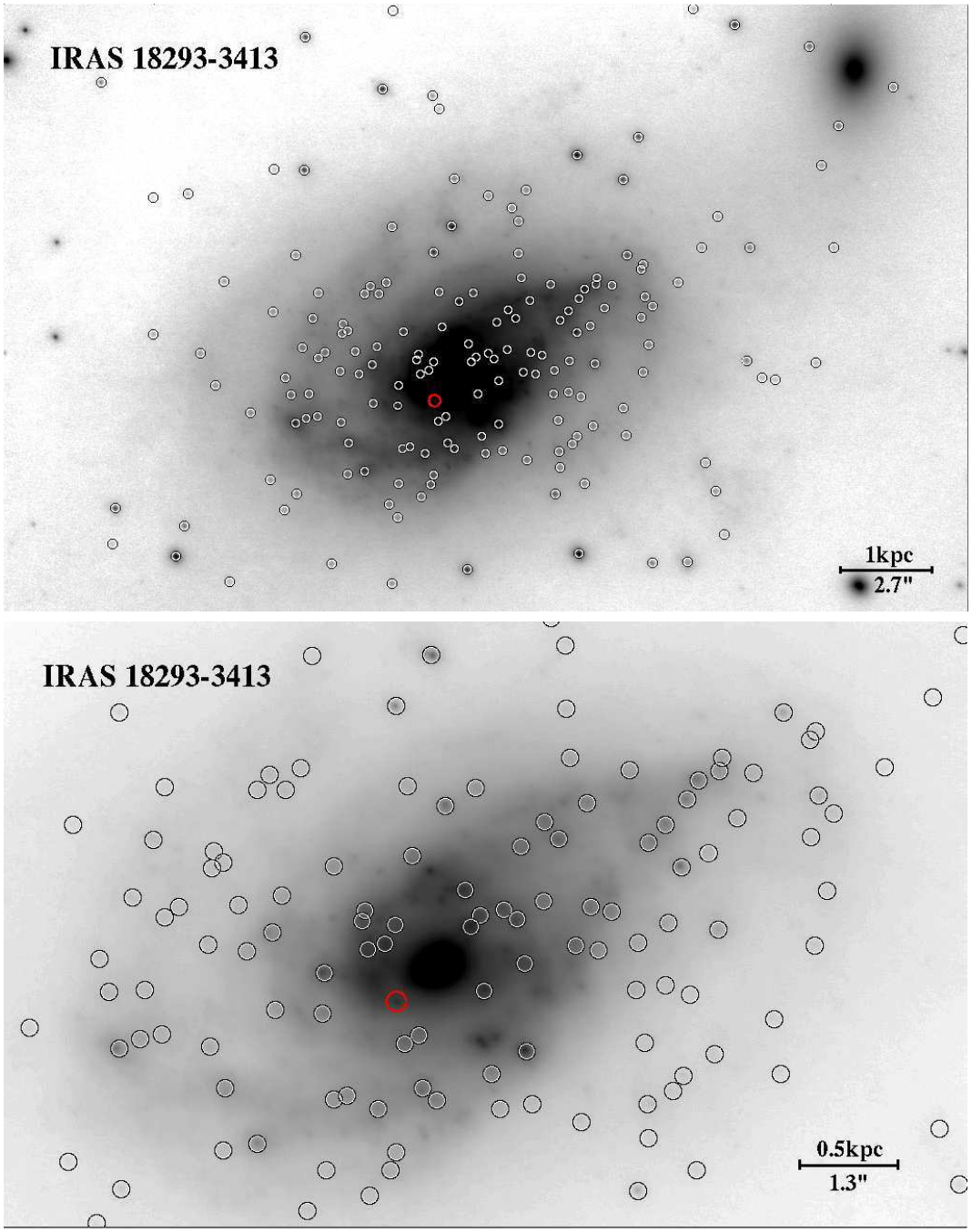
IRAS 18293-3413
1kpc
2.7"
IRAS 18293-3413
0.5kpc
1.3"

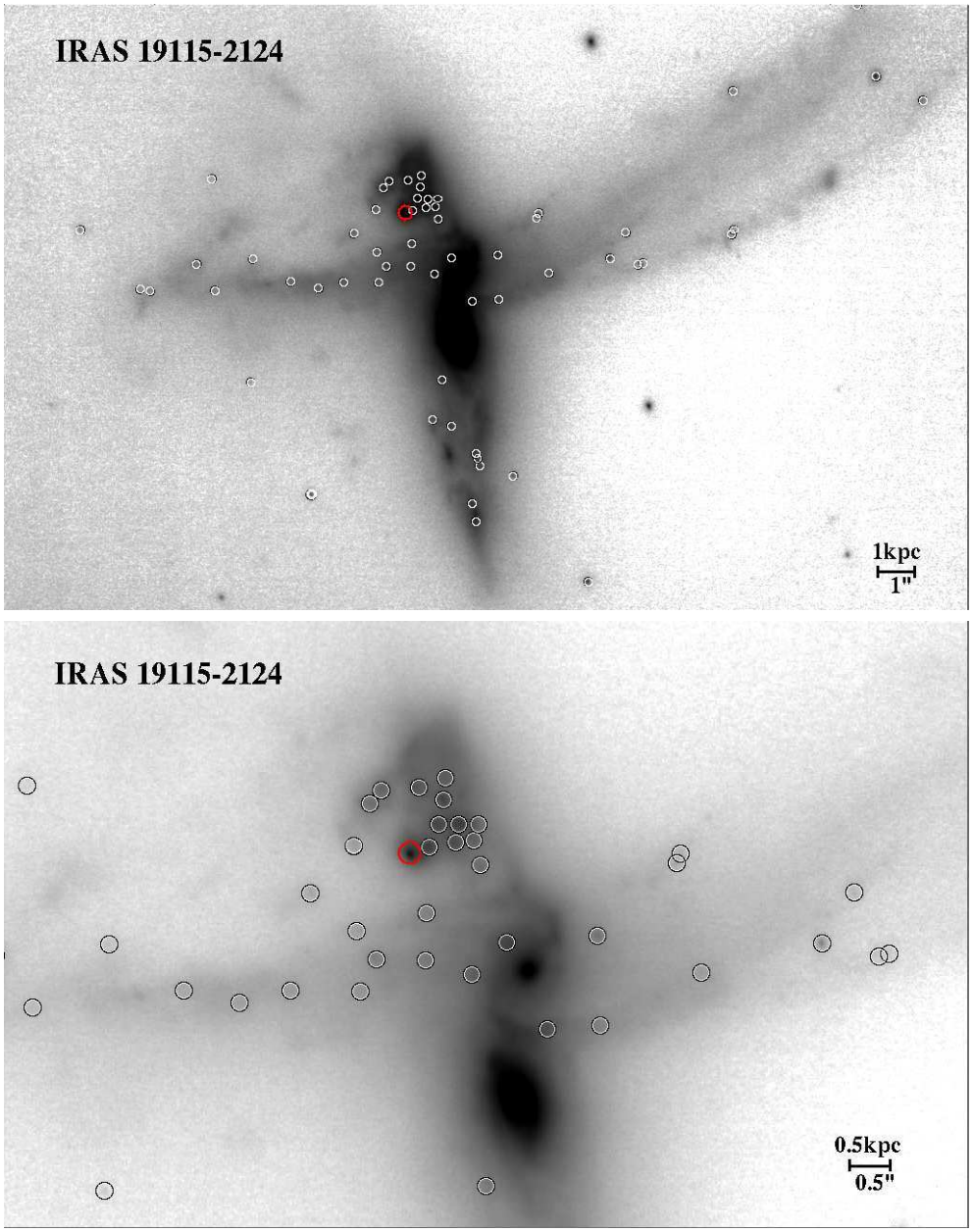

Figure A.1: Astronomical images of our LIRGs representative sample in the K_S-band filter. The selected super star cluster candidates are marked with open circles. For each target, the lower panel is a zoomed in version of the science image to better show SSC candidates which are around the galaxy nucleus. They are quite few in MCG +08-11-002 and CGCG 049-057 but are abundant in IRAS 18293-3413. Mostly located in the "extended regions"of the galaxy, the brightest cluster candidate is marked with a red circle.

Appendix B

Algorithm of the MC completenesss simulations

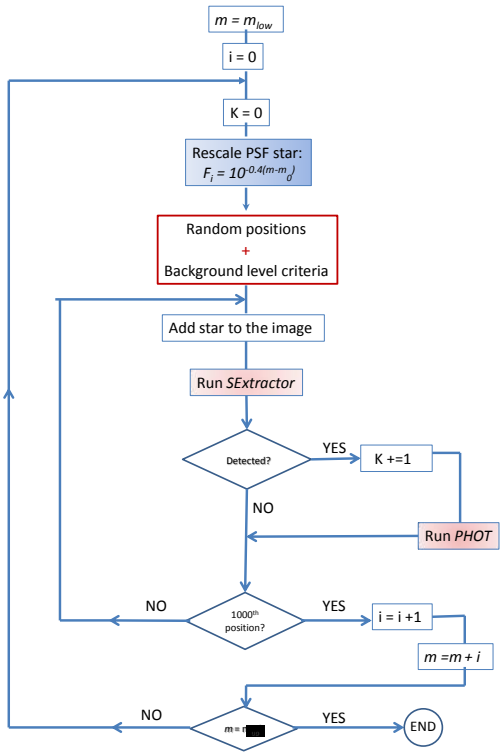

Figure B.1: A simple algorithm of the MC simulation used to correct for observational incompleteness. In this work, the simulation ran from $M_{low} = 18$ to $M_{up} = 22$ magnitudes in steps of 0.5.

Appendix C

The MC completenesss curves

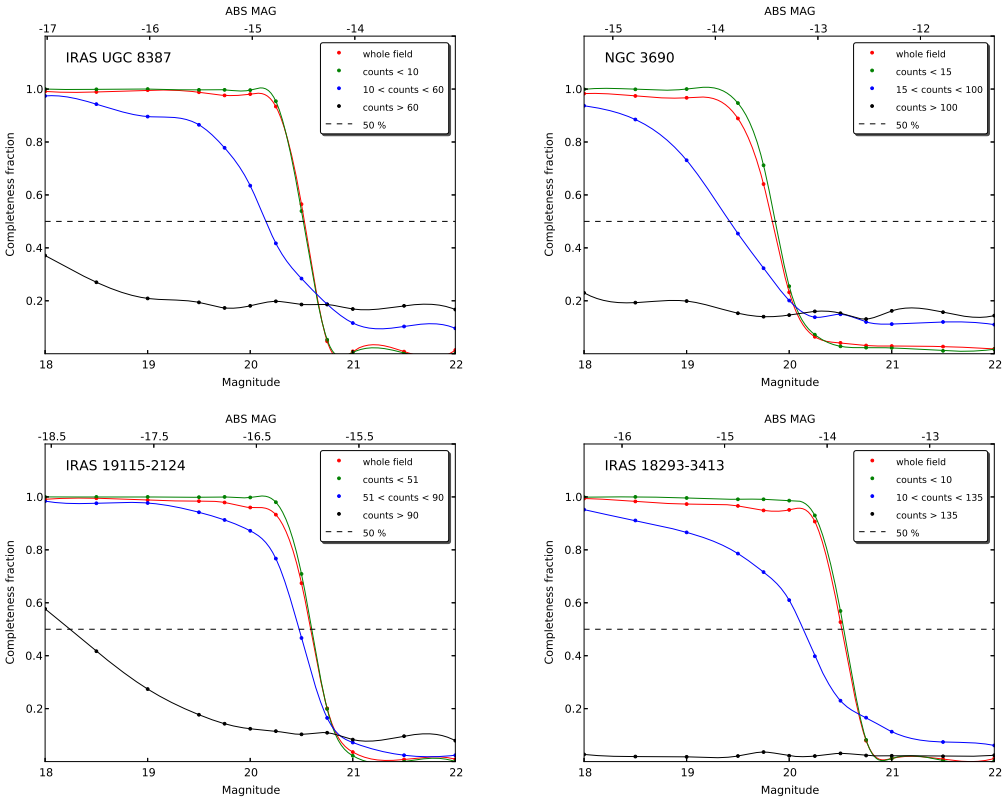

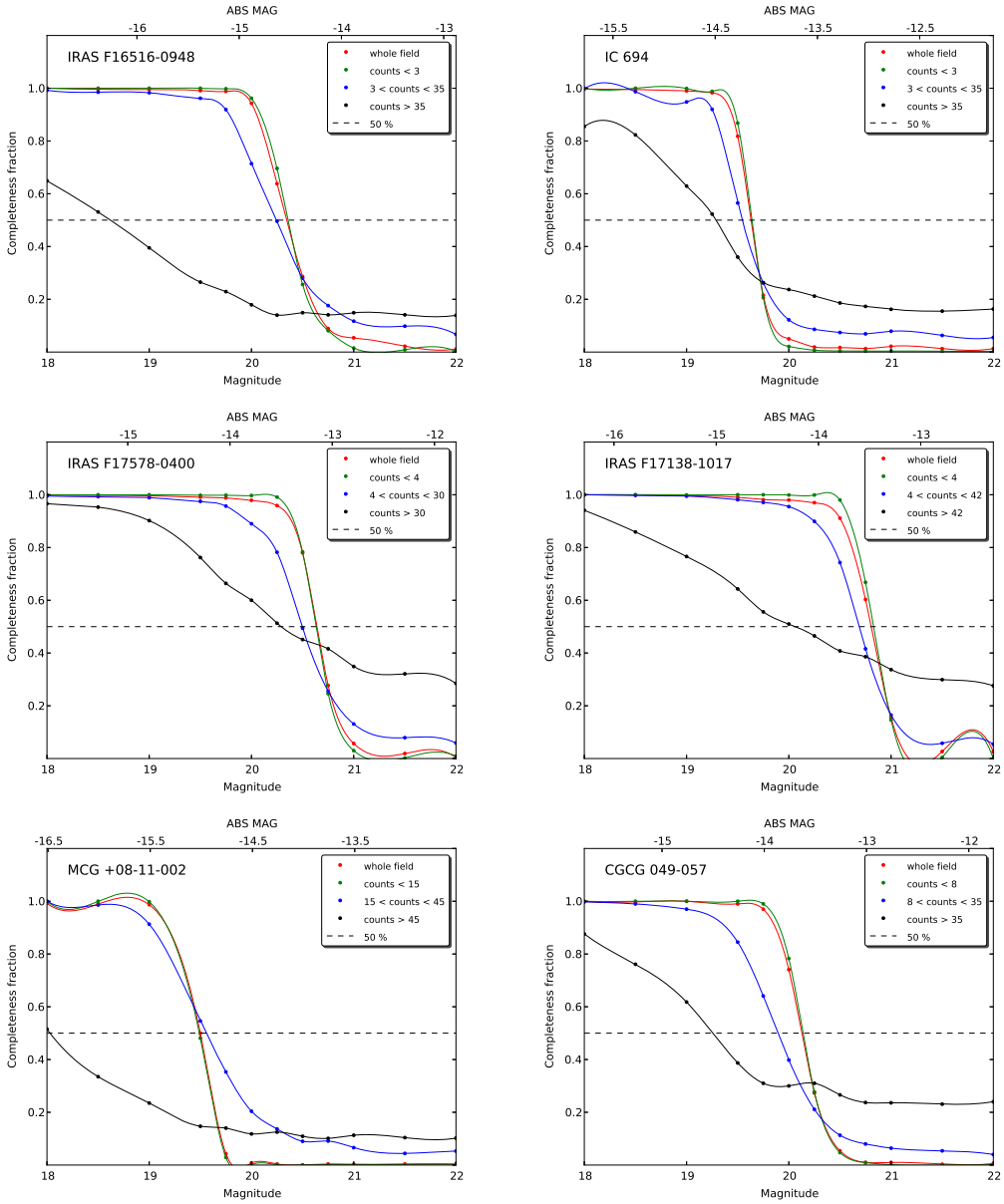

Figure C.1: The results of Monte Carlo completeness simulations within different regions of each target. Each curve corresponds to the interpolation of data points output by the simulation for a given background level. The horizontal dashed line represents the 50 % completeness limit. From the figure, we can see that a superposition of many background levels lead to a shallower completeness curve which is the case for the blue and the black curves. They respectively correspond to the middle and the inner regions of the frame.

Bibliography

Adamo, A., Östlin, G., Zackrisson, E., Hayes, M., Cumming, R. J., & Micheva, G. 2010, MNRAS, 949

Alonso-Herrero, A., Rieke, G. H., Rieke, M. J., Colina, L., Pérez-González, P. G., & Ryder, S. D. 2006, ApJ, 650, 835

Anders, P., Bissantz, N., Boysen, L., de Grijs, R., & Fritze-v. Alvensleben, U. 2007, MNRAS, 377, 91

Arp, H. & Sandage, A. 1985, AJ, 90, 1163

Barkana, R. & Loeb, A. 2001, Phys. Rep., 349, 125

Bastian, N. 2008, MNRAS, 390, 759

Bastian, N. & Goodwin, S. P. 2006, MNRAS, 369, L9

Bell, E. F., Papovich, C., Wolf, C., Le Floc'h, E., Caldwell, J. A. R., Barden, M., Egami, E., McIntosh, D. H., Meisenheimer, K., Pérez-González, P. G., Rieke, G. H., Rieke, M. J., Rigby, J. R., & Rix, H. 2005, ApJ, 625, 23

Benedict, G. F., Higdon, J. L., Jefferys, W. H., Duncombe, R., Hemenway, P. D., Shelus, P. J., Whipple, A. L., Nelan, E., Story, D., McArthur, B., McCartney, J., Franz, O. G., Fredrick, L. W., & van Altena, W. F. 1993, AJ, 105, 1369

Bertin, E. & Arnouts, S. 1996, A&AS, 117, 393

Bik, A., Lamers, H. J. G. L. M., Bastian, N., Panagia, N., & Romaniello, M. 2003, A&A, 397, 473

Bluck, A. F. L., Conselice, C. J., Bouwens, R. J., Daddi, E., Dickinson, M., Papovich, C., & Yan, H. 2009, MNRAS, 394, L51

Boily, C. M. & Kroupa, P. 2003, MNRAS, 338, 665

Bruzual A., G. & Charlot, S. 1993, ApJ, 405, 538

Bushouse, H. A. 1986, AJ, 91, 255

Chandar, R., Whitmore, B. C., Kim, H., Kaleida, C., Mutchler, M., Calzetti, D., Saha, A., O'Connell, R., Balick, B., Bond, H., Carollo, M., Disney, M., Dopita, M. A., Frogel, J. A., Hall, D., Holtzman, J. A., Kimble, R. A., McCarthy, P., Paresce, F., Silk, J., Trauger, J., Walker, A. R., Windhorst, R. A., & Young, E. 2010, ApJ, 719, 966

Cowie, L. L., Songaila, A., Hu, E. M., & Cohen, J. G. 1996, AJ, 112, 839

de Grijs, R. 2005, Highlights of Astronomy, 13, 363

—. 2009, Ap&SS, 324, 283

de Grijs, R., Anders, P., Bastian, N., Lynds, R., Lamers, H. J. G. L. M., & O'Neil, E. J. 2003, MNRAS, 343, 1285

de Grijs, R. & Parmentier, G. 2007, Chinese Journal of Astronomy and Astrophysics, 7, 155

Elbaz, D., Cesarsky, C. J., Chanial, P., Aussel, H., Franceschini, A., Fadda, D., & Chary, R. R. 2002, A&A, 384, 848

Elbaz, D., Daddi, E., Le Borgne, D., Dickinson, M., Alexander, D. M., Chary, R., Starck, J., Brandt, W. N., Kitzbichler, M., MacDonald, E., Nonino, M., Popesso, P., Stern, D., & Vanzella, E. 2007, A&A, 468, 33

Elmegreen, B. G. & Efremov, Y. N. 1997, ApJ, 480, 235

Elmegreen, D. M., Chromey, F. R., McGrath, E. J., & Ostenson, J. M. 2002, AJ, 123, 1381

Elson, R. A. W. & Fall, S. M. 1985, ApJ, 299, 211

Fall, S. M., Chandar, R., & Whitmore, B. C. 2009, ApJ, 704, 453

Fritze-v. Alvensleben, U. 1999, A&A, 342, L25

Genzel, R., Lutz, D., Sturm, E., Egami, E., Kunze, D., Moorwood, A. F. M., Rigopoulou, D., Spoon, H. W. W., Sternberg, A., Tacconi-Garman, L. E., Tacconi, L., & Thatte, N. 1998, ApJ, 498, 579

Gieles, M. 2010, in Astronomical Society of the Pacific Conference Series, Vol. 423, Astronomical Society of the Pacific Conference Series, ed. B. Smith, J. Higdon, S. Higdon, & N. Bastian, 123–+

Gieles, M., Larsen, S. S., Bastian, N., & Stein, I. T. 2006a, A&A

Gieles, M., Larsen, S. S., Scheepmaker, R. A., Bastian, N., Haas, M. R., & Lamers, H. J. G. L. M. 2006b, A&A

Goodwin, S. P. & Bastian, N. 2006, MNRAS, 373, 752

Goto, T., Arnouts, S., Inami, H., Matsuhara, H., Pearson, C., Takeuchi, T. T., Le Floc'h, E., Takagi, T., Wada, T., Nakagawa, T., Oyabu, S., Ishihara, D., Lee, H. M., Jeong, W., Yamauchi, C., Serjeant, S., Sedgwick, C., & Treister, E. 2010, ArXiv e-prints

Gott, III, J. R., Jurić, M., Schlegel, D., Hoyle, F., Vogeley, M., Tegmark, M., Bahcall, N., & Brinkmann, J. 2005, ApJ, 624, 463

Graciá-Carpio, J., García-Burillo, S., Planesas, P., Fuente, A., & Usero, A. 2008, A&A, 479, 703

Hacking, P., Houck, J. R., & Condon, J. J. 1987, ApJ, 316, L15

Ho, L. C. 1997, in Revista Mexicana de Astronomia y Astrofisica Conference Series, Vol. 6, Revista Mexicana de Astronomia y Astrofisica Conference Series, ed. J. Franco, R. Terlevich, & A. Serrano, 5–+

Holtzman, J. A., Faber, S. M., Shaya, E. J., Lauer, T. R., Groth, J., Hunter, D. A., Baum, W. A., Ewald, S. P., Hester, J. J., Light, R. M., Lynds, C. R., O'Neil, Jr., E. J., & Westphal, J. A. 1992, AJ, 103, 691

Hunter, D. A., Elmegreen, B. G., Dupuy, T. J., & Mortonson, M. 2003, AJ, 126, 1836

Imanishi, M. 2008, Mem. Soc. Astron. Italiana, 79, 1193

Iono, D., Wilson, C. D., Yun, M. S., Baker, A. J., Petitpas, G. R., Peck, A. B., Krips, M., Cox, T. J., Matsushita, S., Mihos, J. C., & Pihlstrom, Y. 2009, ApJ, 695, 1537

Johnson, K., Beck, S., Evans, A., Goss, M., Lonsdale, C., O'Connell, R., Turner, J., Ulvestad, J., & Wilson, C. 2009, in Astronomy, Vol. 2010, astro2010: The Astronomy and Astrophysics Decadal Survey, 141–+

Johnson, K. E. 2005, in IAU Symposium, Vol. 227, Massive Star Birth: A Crossroads of Astrophysics, ed. R. Cesaroni, M. Felli, E. Churchwell, & M. Walmsley, 413–422

Joy, M., Telesco, C. M., Decher, R., Lester, D. F., Harvey, P. M., Rickard, L. J., & Bushouse, H. 1989, ApJ, 339, 100

Juneau, S., Glazebrook, K., Crampton, D., McCarthy, P. J., Savaglio, S., Abraham, R., Carlberg, R. G., Chen, H., Le Borgne, D., Marzke, R. O., Roth, K., Jørgensen, I., Hook, I., & Murowinski, R. 2005, ApJ, 619, L135

Kankare, E., Mattila, S., Ryder, S., Pérez-Torres, M., Alberdi, A., Romero-Canizales, C., Díaz-Santos, T., Väisänen, P., Efstathiou, A., Alonso-Herrero, A., Colina, L., & Kotilainen, J. 2008, ApJ, 689, L97

Keel, W. C., Kennicutt, Jr., R. C., Hummel, E., & van der Hulst, J. M. 1985, AJ, 90, 708

Kennicutt, Jr., R. C. 1998a, ARA&A, 36, 189

—. 1998b, ApJ, 498, 541

Kim, D. & Sanders, D. B. 1998, ApJS, 119, 41

Lada, C. J. & Lada, E. A. 2003, ARA&A, 41, 57

Lada, C. J., Margulis, M., & Dearborn, D. 1984, ApJ, 285, 141

Lai, O., Rouan, D., Rigaut, F., Doyon, R., & Lacombe, F. 1999, A&A, 351, 834

Larsen, S. S. 2002, AJ, 124, 1393

—. 2009, A&A, 494, 539

Larsen, S. S. & Richtler, T. 1999, A&A, 345, 59

Larson, R. B. 2003, Reports on Progress in Physics, 66, 1651

Le Floc'h, E., Papovich, C., Dole, H., Bell, E. F., Lagache, G., Rieke, G. H., Egami, E., Pérez-González, P. G., Alonso-Herrero, A., Rieke, M. J., Blaylock, M., Engelbracht, C. W., Gordon, K. D., Hines, D. C., Misselt, K. A., Morrison, J. E., & Mould, J. 2005, ApJ, 632, 169

Lonsdale, C. J., Farrah, D., & Smith, H. E. 2006, Ultraluminous Infrared Galaxies, ed. Mason, J. W. (Springer Verlag), 285–+

Low, J. & Kleinmann, D. E. 1968, AJ, 73, 868

Madau, P., Ferguson, H. C., Dickinson, M. E., Giavalisco, M., Steidel, C. C., & Fruchter, A. 1996, MNRAS, 283, 1388

Maíz Apellániz, J. & Úbeda, L. 2005, ApJ, 629, 873

Mattila, S., Väisänen, P., Farrah, D., Efstathiou, A., Meikle, W. P. S., Dahlen, T., Fransson, C., Lira, P., Lundqvist, P., Östlin, G., Ryder, S., & Sollerman, J. 2007, ApJ, 659, L9

Mengel, S., Lehnert, M. D., Thatte, N., & Genzel, R. 2005, A&A, 443, 41

Neugebauer, G., Habing, H. J., van Duinen, R., Aumann, H. H., Baud, B., Beichman, C. A., Beintema, D. A., Boggess, N., Clegg, P. E., de Jong, T., Emerson, J. P., Gautier, T. N., Gillett, F. C., Harris, S., Hauser, M. G., Houck, J. R., Jennings, R. E., Low, F. J., Marsden, P. L., Miley, G., Olnon, F. M., Pottasch, S. R., Raimond, E., Rowan-Robinson, M., Soifer, B. T., Walker, R. G., Wesselius, P. R., & Young, E. 1984, ApJ, 278, L1

O'Connell, R. W., Gallagher, III, J. S., & Hunter, D. A. 1994, ApJ, 433, 65

Okamoto, T. & Habe, A. 2000, PASJ, 52, 457

Okamoto, T. & Nagashima, M. 2001, ApJ, 547, 109

Parmentier, G. & Gilmore, G. 2007, MNRAS, 377, 352

Portegies Zwart, S. F., McMillan, S. L. W., & Gieles, M. 2010, ARA&A, 48, 431

Rieke, G. H. & Low, F. J. 1972, ApJ, 176, L95+

Rosolowsky, E. 2005, PASP, 117, 1403

Sanders, D. B., Mazzarella, J. M., Kim, D., Surace, J. A., & Soifer, B. T. 2003, AJ, 126, 1607

Sanders, D. B. & Mirabel, I. F. 1996, ARA&A, 34, 749

Schmidt, M. 1959, ApJ, 129, 243

Smail, I., Ivison, R. J., Blain, A. W., & Kneib, J. 1998, ApJ, 507, L21

Soifer, B. T., Rowan-Robinson, M., Houck, J. R., de Jong, T., Neugebauer, G., Aumann, H. H., Beichman, C. A., Boggess, N., Clegg, P. E., Emerson, J. P., Gillett, F. C., Habing, H. J., Hauser, M. G., Low, F. J., Miley, G., & Young, E. 1984, ApJ, 278, L71

Soifer, B. T., Sanders, D. B., Madore, B. F., Neugebauer, G., Danielson, G. E., Elias, J. H., Lonsdale, C. J., & Rice, W. L. 1987, ApJ, 320, 238

Solomon, P. M., Rivolo, A. R., Barrett, J., & Yahil, A. 1987, ApJ, 319, 730

Stanford, S. A. & Bushouse, H. A. 1991, ApJ, 371, 92

Toomre, A. 1977, in Evolution of Galaxies and Stellar Populations, ed. B. M. Tinsley & R. B. Larson, 401–+

Väisänen, P., Mattila, S., Kniazev, A., Adamo, A., Efstathiou, A., Farrah, D., Johansson, P. H., Östlin, G., Buckley, D. A. H., Burgh, E. B., Crause, L., Hashimoto, Y., Lira, P., Loaring, N., Nordsieck, K., Romero-Colmenero, E., Ryder, S., Still, M., & Zijlstra, A. 2008, MNRAS, 384, 886

Väisänen, P., Mattila, S., & Ryder, S. 2009, ArXiv e-prints

van den Bergh, S. 2004, in Astronomical Society of the Pacific Conference Series, Vol. 322, The Formation and Evolution of Massive Young Star Clusters, ed. H. J. G. L. M. Lamers, L. J. Smith, & A. Nota, 3–+

Vesperini, E. & Zepf, S. E. 2003, ApJ, 587, L97

Weidner, C., Kroupa, P., & Larsen, S. S. 2004, MNRAS, 350, 1503

Whitmore, B. C. 2000, ArXiv Astrophysics e-prints

Whitmore, B. C. 2003, in A Decade of Hubble Space Telescope Science, ed. M. Livio, K. Noll, & M. Stiavelli, 153–178

Whitmore, B. C. 2004, in Astronomical Society of the Pacific Conference Series, Vol. 322, The Formation and Evolution of Massive Young Star Clusters, ed. H. J. G. L. M. Lamers, L. J. Smith, & A. Nota, 419–+

Whitmore, B. C., Chandar, R., Schweizer, F., Rothberg, B., Leitherer, C., Rieke, M., Rieke, G., Blair, W. P., Mengel, S., & Alonso-Herrero, A. 2010, AJ, 140, 75

Whitmore, B. C., Schweizer, F., Leitherer, C., Borne, K., & Robert, C. 1993, AJ, 106, 1354

Whitmore, B. C., Zhang, Q., Leitherer, C., Fall, S. M., Schweizer, F., & Miller, B. W. 1999, AJ, 118, 1551

Wright, G. S., James, P. A., Joseph, R. D., & McLean, I. S. 1990, Nature, 344, 417